

Band 72

Schriftenreihe des Lehrstuhls für
Wasserchemie und Wassertechnologie
und der DVGW-Forschungsstelle am Engler-Bunte-Institut
des Karlsruher Instituts für Technologie (KIT)

**Investigating biofilm deformation using optical coherence
tomography and fluid-structure interaction simulation**

Florian Blauert

Herausgeber

Harald Horn

Karlsruhe 2017

Florian Blauert

Investigating biofilm deformation using optical coherence tomography and fluid-structure interaction simulation

Herausgeber: Harald Horn

Band 72

Schriftenreihe des Lehrstuhls für Wasserchemie und Wassertechnologie und der DVGW-Forschungsstelle am Engler-Bunte-Institut des Karlsruher Instituts für Technologie (KIT)
Karlsruhe 2017

ISSN: 2195-2973

Lehrstuhl für Wasserchemie und Wassertechnologie und DVGW-Forschungsstelle
am Engler-Bunte-Institut des Karlsruher Instituts für Technologie (KIT)

Engler-Bunte-Ring 9

D-76131 Karlsruhe

Tel.: +49-(0)721-608-42581

Fax: +49-(0)721-608-46497

E-mail: ebi-sekretariat-wasserchemie@kit.edu

<http://wasserchemie.ebi.kit.edu/>

Titelbild: Reale Biofilmdeformation aufgenommen mittels optischer Kohärenz-
tomographie (oben) und simulierte Biofilmdeformation mittels Comsol Multiphysics®(unten).

Dieses Werk wird durch das deutsche Urheberrechtsgesetz und internationale Verträge
urheberrechtlich geschützt.

© 2017 Prof. Dr. H. Horn. Alle Rechte vorbehalten. All rights reserved.

Investigating biofilm deformation using optical coherence tomography and fluid-structure interaction simulation

Zur Erlangung des akademischen Grades eines
Doktors der Ingenieurwissenschaften (Dr.-Ing.)

der Fakultät für Chemieingenieurwesen und Verfahrenstechnik
des Karlsruher Instituts für Technologie (KIT)

genehmigte
Dissertation

von
Florian Blauert, M. Sc.
aus Kassel, Deutschland

Referent:	Prof. Dr. rer. nat. Harald Horn
Korreferent:	Prof. Dr.-Ing. Wolfgang A. Wall
Korreferent:	Dr.-Ing. Cristian Picioreanu
Tag der mündlichen Prüfung:	10.03.2017

“Success is not final, failure is not fatal, it is
the courage to continue that counts.”

-Winston Churchill

Acknowledgments

First of all I would like to thank Prof. Harald Horn for the commitment and trust to let me do my PhD in this wonderful group. Fruitful discussions and ongoing support guided me through these years of learning and developing the skills, which provided the basis for my future career. I also like to thank Dr. Michael Wagner for the time and effort he put into the supervision of my work and practical skills. I appreciate the freedom they have given me to explore new approaches and collaborations, which led the right path for my thesis. A special thanks to my fellow PhD candidates Fabian Brunner and Marc Tuczinski, who started with me this journey and shared the difficulties and challenges along the way. It was a great time and will always be remembered. Special thanks go to my former colleagues and now close friends Samuel Welker and Shelesh Agrawal, who left for TU Darmstadt to continue their career as doctoral candidates. Thank you for the wonder- and cheerful time in and outside of the institute. I further wish to thank our group members: Laure, Ewa, Alex, Max, Philip, Steffi, Alondra, Oliver, Annika, Isa, Nico, Andrea, Florencia, Gudrun Abbt-Braun, and Birgit Gordalla; as well as our technicians: Antje, Dunja, Uli, Rafael, Axel, Reinhard, and Matthias. It was a joyful time with all of you. With some I worked more closely and some less, but the outcome was always pleasant. Scientific and social discussions always helped me and made me think. Special thanks go to Rudger Heß and Arvind Pari for working with me and helping me to develop my coordination skills. It was an exciting and joyful time with the both of you. Also special thanks to my HiWi Hannes Frey, who supported me with my experiments in the most stressful times. Without you many experiments would not have been carried out. Thanks go to the mechanical and electrical workshops. The work with Alfred Herbst, Erwin Wachter, and Norbert Andree was a great pleasure. They put endless effort in my plans to realize and produce my experimental designs. Stefan Herbel and Mathias Kieslich helped me with endless electrical problems and were always there for coffee (and cake). I would like to thank Dr. Cristian Picioreanu for the supervision and review of my thesis. Furthermore, I appreciated the pleasant time in the Department of Biotechnology, Delft University of Technology. The time I spend in Delft was one of the most joyful days in my PhD. Sharing science and learning new techniques was an extremely exciting experience in my scientific career. Also many thanks to Prof. Wolfgang A. Wall from the Institute for Computational Mechanics, Technical University of Munich, for the time to review my thesis. Finally I would like to thank my girlfriend Jueying for the ongoing support, ideas, help, pressure, and amazing time in the lab, as well as outside. It was a joy and honor to work and share my personal and professional time with you. Thank you very much. Last, but not least I would like to thank my parents and friends for their ongoing support in better and worse times. I am tremendously grateful for your backup and the believe in me to achieve my life goals.

- Florian Blauert

Abstract

The nature of biofilm mechanics is still one of the most understudied fields in biofilm research. The main challenge is to understand the complex interplay of deformation and matrix re-arrangements. Both give the biofilm matrix its enormous resistance against environmental stress. After the discovery of biofilms behaving as viscoelastic material, research of the elastic properties basically stopped. But it is the elastic part, which defines rigidity, elasticity, and ability to absorb applied stress without detaching.

The following thesis deepens the understanding about elastic properties of the biofilm matrix. Using optical coherence tomography (OCT) new insights in the dynamics of the elastic deformation process of heterotrophic waste water biofilms were gained. This includes the observation of porosity change during deformation, scaling of mechanical properties at different Reynolds numbers during cultivation, and access to mechanical properties, which have not been measured before. For the first time the bulk modulus of biofilms and its inverse, the compressibility, were evaluated. This allowed to determine the Poisson's ratio, which describes the relation between transverse and axial elongation and is one of the most underrated parameters in biofilm mechanics. Biofilms, which contain a high amount of water, were assumed to behave as incompressible materials similar to rubber. Therefore, positive values of the Poisson's ratio were always used in biofilm models dealing with deformation. However, dynamic deformation experiments allowed to prove a high compressibility and low bulk modulus of the biofilm matrix leading to the conclusion that biofilms should be partially classified as auxetic materials with a negative Poisson's ratio. This changes the understanding of the mechanical nature of biofilms. In fluid-structure interaction simulations the evaluated parameters were hence used to deepen the understanding of the mechanical nature of biofilms. Real biofilm geometries acquired in deformation experiments were used to improve the evaluation of mechanical properties without relying on estimations about the stress acting on the bulk-biofilm interface. In the simulations it was shown that the Young's modulus cannot be considered constant. It rather scales with the flow velocity. This is a direct consequence of the heterogeneity of the biofilm matrix. At last, the influence of a negative Poisson's ratio on the deformation behavior of biofilms was investigated and discussed. Simulations with negative Poisson's ratios showed deformation fields comparable to deformed biofilms imaged by means of OCT. These simulations showed that biofilms can partially be considered auxetic materials.

Zusammenfassung

Das Feld der Biofilmmechanik ist noch immer einer der am wenigsten untersuchten Bereiche der Biofilmforschung. Um zu verstehen, was Biofilmen eine so große Widerstandskraft gegen Scherspannung verleiht, muss das Wechselspiel von Deformation und Änderung der Biofilmmatrix im Detail untersucht werden. Seit der Einordnung von Biofilmen in viskoelastische Materialien wurden fast keine Untersuchungen hinsichtlich elastischer Deformation durchgeführt. Jedoch sind es die elastischen Eigenschaften eines Biofilms, welche der Biofilmmatrix die Fähigkeit zur Absorption von mechanischem Stress maßgeblich beeinflussen.

Diese Dissertation vertieft das Verständnis im Bereich der elastischen Biofilmmechanik. Durch die Nutzung der optischen Kohärenztomographie (OCT) konnten neue Erkenntnisse über die Dynamik der elastischen Biofilmdeformation gewonnen werden. Das beinhaltet die Änderung der Porosität während des Deformationsprozesses, die Änderung der mechanischen Eigenschaften mit der Fließgeschwindigkeit während der Kultivierung, sowie die Bestimmung zuvor noch nicht gemessener mechanischer Parameter wie die Poissonzahl, das Kompressionsmodul, sowie die Kompressibilität von Biofilmen. Zum ersten Mal konnte eine Messgröße für die Poissonzahl bestimmt werden, welche die relative Längenänderung zwischen transversaler und axialer Deformation beschreibt. Da Biofilme einen hohen Wassergehalt haben, wurde lange Zeit angenommen, dass sie sich wie inkompressible Materialien (z.B. Gummi) verhalten. Daher wurden in Simulationsstudien immer positive Werte für die Poissonzahl angenommen. OCT Aufnahmen während Deformationsexperimente zeigten jedoch eine höchst kompressible Biofilmmatrix. Daraus wurde geschlossen, dass es sich bei den untersuchten Biofilmen zum Teil um sogenannte auxetische Materialien mit negativer Poissonzahl handelt. Dies ändert das Verständnis der mechanischen Natur von Biofilmen maßgeblich. Die daraus ermittelten Werte erlaubten zudem die Bestimmung des Kompressionsmoduls, sowie der Kompressibilität.

In Fluid-Struktur-Interaktions Simulationen wurden die gewonnenen Parameter daher genutzt, um das mechanische Verständnis von Biofilmen im Detail zu verstehen. Biofilmdeformationen, welche mittels OCT verfolgt wurden, lieferten reale Geometrien, die als strukturelle Vorlage für die Simulationen dienten. Durch die Implementierung von realen Geometrien konnte die Abschätzung von Materialkonstanten weiter verbessert werden. Mit diesen Simulationen konnte gezeigt werden, dass der Young's Modulus bei ansteigender Schubspannung nicht konstant bleibt. Dies ist eine direkte Konsequenz der Heterogenität der Biofilmstruktur. Zuletzt wurde der Einfluss von negativen Poissonzahlen untersucht und die Qualität der Simulationen diskutiert. Biofilme zeigten in Simulationen mit negativen Poissonzahlen Deformationen, welche vergleichbar mit den realen OCT Aufnahmen waren. Die Simulationen zeigten, dass es sich bei Biofilmen teilweise um auxetische Materialien handelt.

Publication list

Peer-reviewed publications

Blauert F., Horn H., Wagner M., Time-resolved biofilm deformation measurements using optical coherence tomography. *Biotechnol. Bioeng.*, 112:18931905, 2015.

Herrling M. P., Fetsch K. L., Delay M., **Blauert F.**, Wagner M., Franzreb M., Horn H., Lackner S., Low biosorption of PVA coated engineered magnetic nanoparticles in granular sludge assessed by magnetic susceptibility. *Sci. Total Environ.*, 537:4350, 2015.

Yang J., Zhang D., Chen Z., **Blauert F.**, Jiang B., Dai D., Wu G., Zhang D., Yang X., Effect of CH stretching excitation on the reaction dynamics of $F + CHD_3 \rightarrow DF + CHD_2$, *J. Chem. Phys.*, 143:44316, 2015.

Conference contributions

Blauert F., Horn H., Wagner M., A new attempt to measure biofilm rheology by optical coherence tomography. *Biofilms 6*, 11-13 Mai 2014, in Vienna, Austria.

Blauert F., Wagner M., Horn H., Time-lapsed Three-dimensional Biofilm Deformation in Situ and Non-invasively Visualized and Quantified by Means of Optical Coherence Tomography. 7th *ASM Conference on Biofilms*, 24-29 September 2015, in Chicago, USA.

Blauert F., Pavissich J. P., Wagner M., Horn H., Piciooreanu C., Evaluation of biofilm mechanical properties using optical coherence tomography (OCT) and fluid-structure interaction simulations. *Biofilms 7*, 26-28 June 2016, in Porto, Portugal.

Contents

1	Introduction	1
2	Materials and methods	7
2.1	Biofilm cultivation	7
2.1.1	Hydrodynamic conditions during cultivation	8
2.1.2	Cultivation of biofilms	9
2.2	Optical coherence tomography (OCT)	11
2.3	OCT settings for cultivation and deformation experiments	12
2.3.1	Dynamic deformation experiments	13
2.3.2	Time-lapsed experiments	14
2.4	OCT data-set analysis	15
2.4.1	OCT data processing	15
2.4.2	Mean biofilm thickness	17
2.4.3	Surface roughness coefficient	17
2.4.4	Biofilm porosity	17
2.5	Mechanical properties of biofilms	19
2.6	Fluid-structure interaction model	22
2.6.1	Model domain	22
2.6.2	Model domain equations	23
2.6.3	Model boundary conditions	26
2.6.4	Model solutions	26
2.6.5	Evaluation of the Young's modulus from the simulation	26
3	Results and discussion	28
3.1	Structural integrity of biofilms	28
3.2	Assessing the mechanical properties of biofilms	31
3.2.1	Elastic biofilm deformation	31
3.2.2	Viscoelastic biofilm deformation	42
3.2.3	Material property variations in biofilms	49
3.3	Dependence of mechanical properties on substrate and Reynolds number	51
3.3.1	Cultivated biofilms	51
3.3.2	Influence of cultivation conditions on the shear Modulus G	55
3.3.3	Influence of cultivation conditions on the Young's modulus E	58
3.3.4	Influence of porosity on material properties	61
3.3.5	Shear strength of biofilms	62
3.3.6	Biofilm relaxation after deformation	64
3.3.7	Poisson's ratio ν of biofilms	65
3.3.8	Bulk modulus K and compressibility β of biofilms	69
3.4	Biofilm modeling using real biofilm geometries	73

3.4.1	OCT images as structural templates in 2D FSI simulations	74
3.4.2	Flow-field around real biofilm geometries	75
3.4.3	Shear stress distribution onto and in the biofilm structure	77
3.4.4	Assessment of Young's modulus from simulations	80
3.4.5	Scaling of the Young's modulus with fluid flow	82
3.4.6	Influence of the Poisson's ratio on the evaluation of the Young's modulus	84
4	Summary and Outlook	89
5	References	93

List of Figures

1	Experimental setup	7
2	OCT Principle	12
3	Imaging modes of the OCT device	13
4	Stress-Strain Scheme	15
5	Elastic/viscoelastic Deformation	19
6	Deformation scheme	20
7	Model domain	22
8	Elastic deformation at increasing shear stress	32
9	Elastic deformation	33
10	Time-resolved biofilm deformation	35
11	Change of \bar{L}_F and R_a^* in the shear stress experiment	36
12	Evaluation of the shear modulus G	38
13	Long-term elastic deformation	40
14	Biofilm deformation in a stress-strain experiment	43
15	Macro-porosity and roughness change in stress-strain experiments	44
16	Cross-section viscoelastic effekt	46
17	Changes of \bar{L}_F and ε in stress-strain experiments	47
18	Material property variances	50
19	Z-projection biofilm cultivation	52
20	Final biofilm thicknesses before experiments	53
21	Porosity development during cultivation	54
22	Shear modulus vs Reynolds	56
23	Young's modulus vs Reynolds	60
24	Mechanical properties vs porosity	62
25	Biofilm shear strength	62
26	Biofilm relaxation	64
27	Scheme Poisson's ratio ν	65
28	Scheme of the inverted honeycomb structure deformation	66
29	Poisson's ratios of biofilms	67
30	Bulk modulus K of biofilms	69
31	Biofilm compressibility	70
32	Simulation model basis	75
33	Simulated flow field of biofilm I	75
34	Simulated stress distribution	77
35	Simulated versus calculated shear stress	78
36	Simulated von Mises stress distribution	79
37	Simulated biofilm deformation	80
38	Scaling of Young's modulus	82
39	Negative Poisson's ratio in modeling	85

40	Real biofilm deformation indicating a negative Poisson's ratio	85
41	Effect of Poisson's ratio on the scaling of the Young's modulus	86
42	Comparison of best fits for different Poisson's ratios	87

List of Tables

1	Overview shear and Young's modulus of biofilms.	5
2	Cultivation medium composition	9
3	Cultivation conditions for all biofilms	10
4	Cultivation conditions for biofilm images presented in this thesis	10
5	Model variables and parameters	27
6	Local material property variations	50
7	Ranges of shear moduli	57
8	Ranges of Young's moduli	59
9	Material property overview	72
10	Best fit evaluation of the Young's modulus	81
11	Simulated shear stress and Young's modulus	83
12	Best fits of the Young's moduli from all simulations	88

Abbreviations

Ac	<i>sodium-acetate</i>
AFM	<i>atomic force microscopy</i>
CLSM	<i>confocal laser scanning microscopy</i>
COD	<i>chemical oxygen demand</i>
DNA	<i>deoxyribonucleic acid</i>
EPS	<i>extracellular polymeric substances</i>
FSI	<i>fluid-structure interaction</i>
Gl	<i>D-glucose</i>
OCT	<i>optical coherence tomography</i>
Ph	<i>L-phenylalanine</i>
POM	<i>poly-oxymethylene</i>
SLD	<i>super luminescent diode</i>

Mathematical Symbols

$A_{biofilm}$	<i>area of the whole biofilm structure in the OCT B-scan</i>	[px]
$A_{biomass}$	<i>area of the detected biomass in the OCT B-scan</i>	[px]
A_{voids}	<i>area of the detected voids in the OCT B-scan</i>	[px]
d	<i>maximum diameter of the flow cell</i>	[m]
D_h	<i>hydraulic diameter</i>	[m]
E	<i>Young's modulus</i>	[Pa]
F	<i>force</i>	[N]
G	<i>shear modulus</i>	[Pa]
H	<i>height of the flow cell</i>	[m]
k	<i>spring constant</i>	[kg · s ⁻²]
K	<i>bulk modulus</i>	[Pa]
L	<i>length of the biofilm</i>	[m]
L_e	<i>entrance length of the flow channel</i>	[m]
L_x	<i>model domain length</i>	[m]
L_z	<i>model domain height</i>	[m]
\bar{L}_F	<i>mean biofilm thickness</i>	[m]
$L_{F,i}$	<i>biofilm thickness from single OCT A-scan i</i>	[m]
N	<i>total number of A-scans in the OCT image</i>	[-]
p	<i>pressure</i>	[Pa]
p_B	<i>biofilm pore pressure</i>	[Pa]
P	<i>porosity</i>	[-]
P_{crit}	<i>critical porosity</i>	[-]

Mathematical Symbols

Q	<i>mean volumetric flow rate</i>	$[m^3 \cdot s^{-1}]$
R_a^*	<i>surface roughness coefficient</i>	$[-]$
Re	<i>Reynolds number</i>	$[-]$
u_F	<i>flow field in biofilm simulation</i>	$[m \cdot s^{-1}]$
u_{mean}	<i>mean flow velocity</i>	$[m \cdot s^{-1}]$
v_B	<i>deformation field in biofilm simulation</i>	$[m]$
V	<i>biofilm volume</i>	$[m^3]$
W	<i>width of the flow cell</i>	$[m]$
X	<i>distance</i>	$[m]$

Greek Symbols

α	<i>angle of deformation</i>	$[rad]$
α_B	<i>Biot coefficient</i>	$[-]$
β	<i>compressibility</i>	$[Pa^{-1}]$
γ_{SR}	<i>shear strain</i>	$[rad]$
Γ_{FSI}	<i>bulk-biofilm interface</i>	$[m]$
$\Gamma_{in,out}$	<i>inflow/outflow boundary</i>	$[m]$
$\Gamma_{top,sub}$	<i>top/substratum boundary</i>	$[m]$
Γ_{subf}	<i>zero displacement (fixed) boundary</i>	$[m]$
ε	<i>strain</i>	$[-]$
η	<i>dynamic viscosity</i>	$[Pa \cdot s]$
κ_B	<i>biofilm permeability</i>	$[m^{-1}]$
μ	<i>water viscosity</i>	$[Pa \cdot s]$
ν	<i>Poisson's ratio</i>	$[-]$
ν_k	<i>kinematic viscosity</i>	$[Pa \cdot s]$
ρ	<i>biofilm density</i>	$[kg \cdot m^{-3}]$
σ	<i>cauchy stress</i>	$[Pa]$
σ_T	<i>tensile stress</i>	$[Pa]$
σ_B	<i>stress in biofilm</i>	$[Pa]$
σ_F	<i>stress in fluid</i>	$[Pa]$
σ_v	<i>von Mises stress</i>	$[Pa]$
τ	<i>shear stress</i>	$[Pa]$
Φ	<i>biofilm porosity</i>	$[-]$
Ω_B	<i>biofilm domain</i>	$[m^2]$
Ω_F	<i>fluid domain</i>	$[m^2]$

1 Introduction

The biofilm matrix is a highly complex and dynamic environment in which bacteria embed themselves to create a protective microenvironment (Flemming and Wingender, 2010, Sutherland, 2001a,b). This highly hydrated protective matrix consists of extracellular polymeric substances (EPS), and contains up to 97% water (Zhang *et al.*, 1998). The major matrix components are microbial cells, polysaccharides, proteins, and water, together with excreted cellular products (such as DNA). These components form stable networks in the biofilm matrix and show great heterogeneity even at the microscale (μm -range). For bacteria the advantages of biofilm formation are numerous. These include protection from dynamic changes in the environment (Røder *et al.*, 2015, Li and Tian, 2012, Simões *et al.*, 2010), antibiotics (Proia *et al.*, 2016, Holmberg and Rasmussen, 2016), or disinfectants (Charlebois *et al.*, 2017, Abdallah *et al.*, 2015). Since biofilms demonstrate a great resistance against chemical and mechanical treatment, they can be problematic in many industrial processes such as (waste-)water distribution pipelines (Moskvicheva *et al.*, 2016, Gonzalez *et al.*, 2016, Subramanian *et al.*, 2016), on ship hulls (Turan *et al.*, 2016) or as biofouling in food industry (Moreira *et al.*, 2016, 2015). Therefore, the complete removal of biofilms is important. Stress-induced detachment provides an alternative cleaning procedure compared to chemical treatment. The flow velocity is usually increased to create a high shear stress, which finally lead to detachment of the biofilm structure. The ability of biofilms to withstand changing environmental conditions is enormous. Therefore, it is essential to investigate the stability of biofilms in detail. This requires knowledge of the structural integrity, as well as the mechanical properties of the biofilm matrix. However, a simple description of the biofilm matrix is not possible. The complex structure of the biofilm matrix, interspersed with water pores and channels (Costerton *et al.*, 1995), create a variety of local density variations, which increase towards the bottom of the biofilm (de Beer *et al.*, 1994). When biofilms are subjected to fluid flow in a channel or pipe, the corresponding deformation depends on the time of the applied stress. If the stress persists over a short time up to a few minutes, biofilms show an elastic deformation behavior (Körstgens *et al.*, 2001a,b, Mathias and Stoodley, 2009). The elastic framework is suitable to describe the biofilm deformation with material properties such as the shear modulus G or the Young's modulus E . These mechanical properties describe the rigidity and elasticity of the biofilm matrix, respectively. However, due to the slimy matrix it can be well understood that the material does not behave as an ideal elastic solid during deformation, nor flow like a liquid. The biofilm matrix shows a behavior in between. If the stress persists over a longer period of time, the biofilm matrix starts to flow, expressing a viscous response of a liquid. This class of materials is called viscoelastics. Several studies investigated this viscoelastic behavior, using a variety of different experimental techniques, such as fluid shear techniques (Stoodley *et al.*, 1999c), compression measurements (Körstgens *et al.*, 2001a), rheometer creep analysis (Towler *et al.*, 2003), or fluid dynamic gauging (Möhle

et al., 2007). Except for fluid shear techniques testing of the mechanical properties destroy the biofilm structure in the process. Moreover, not all experimental techniques measure on the same scale. Biofilms differ in the matrix composition, containing different amounts of polysaccharides or polypeptides. This results in local differences in the rigidity or elasticity of each biofilm. Methods such as rheometer creep analysis or fluid dynamic gauging measure on the macro-scale in the *cm* region. This provides an average value for the biofilm, but the biofilm sample has often be transferred to the measuring device, possibly altering the structure. On the other hand, methods such as indentation testing measure the force a small metal tip transfers onto the biofilm. The contact area of the tip is small (in the μm range), and therefore the relation of force to contact area is high. This leads to large values of elastic moduli (see Table 1). However, these local measurements do not reflect the the fluid-structure interaction, which is of interest for industrial application. Nevertheless, these experiments gained valuable knowledge about relaxation times (Klapper *et al.*, 2002), a time dependent transition between elastic and viscoelastic processes (Shaw *et al.*, 2004), and helped to develop new mathematical models about biofilm mechanics. Mathematical models simulate elastic deformation as a spring and viscous flow behavior as a dashpot. The easiest combination of both is in series, known as the Maxwell model. If the spring and dashpot are in parallel, it is considered a Kelvin-Voigt model, and a combination of both is used in the Burger model (Findley *et al.*, 1989). Shaw *et al.* (2004) found in a study with 44 different biofilms that the expected transition time from elastic to viscoelastic deformation is on average 18 min for biofilms. This time scale coincides with the time, which is required to express a phenotypic response at the cellular level. Few studies actually investigated the elastic response of the biofilm within these first 18 min. Conclusive data is missing, explaining the exact reaction of biofilms towards changing fluid flow. It is important to understand how the internal structure changes within the biofilm and how heterogeneity influences the deformation behavior. In material science determination of shear or Young's modulus are most often considered as a sufficient description of the material. Few experiments have been conducted to investigate the elastic nature of biofilms. Shear and Young's moduli range from a few *Pa* up to a few *kPa*. The majority of experiments narrow down the range of shear and Young's modulus to be less than 1 *kPa*. However, especially indentation experiments show a stiffness of the biofilm several times larger than shearing or compression tests. Table 1 gives an overview over different experimental techniques and the values for the shear and Young's moduli measured for biofilms. However, the shear and Young's modulus are not the only material properties describing ideal elastic materials. The bulk modulus, and its inverse the compressibility, are connected to the shear and Young's modulus by the Poisson's ratio. In biofilm research these two important material properties have not been investigated yet. This is mainly due to crucial assumptions needed to describe biofilm deformation. The bulk modulus has not been mentioned directly, but several studies (especially membrane reactor ex-

periments (Dreszer *et al.*, 2014b, Derlon *et al.*, 2016, Fortunato *et al.*, 2016)), reported compressible biofilm structures without elucidating the deformation process in detail or giving a number for the compressibility. The Poisson's ratio is also an understudied field in biofilm research. Due to its high water content, the biofilm matrix is considered as a nearly incompressible material, exhibiting rubber like deformation behavior. It was never doubted that the assumption of a positive Poisson's ratio, ranging between $\nu = 0.3 - 0.5$, is wrong.

One of the major problems in biofilm research is the fragile structure of the biofilm matrix. Overall, few experimental studies have been conducted to determine material properties of intact biofilms, mostly due to the technical difficulties associated with such testing. A technique capable of measuring non-invasively and *in situ* is optical coherence tomography (OCT). Huang *et al.* (1991) introduced this technique in the medical field to generate non-destructively cross-sectional images of the retina. OCT is capable of imaging structures in the mm-range, with a μm -resolution. It is a fast imaging technique for which no staining is needed. When OCT was introduced in biofilm research by Xi *et al.* (2006), research focus shifted to measure intrinsic properties, such as porosity, surface roughness, and distribution of cavities over time (Wagner *et al.*, 2010a). Furthermore, it is now possible to explain dynamics within the biofilm system. Haisch and Niessner (2007) added H_2O_2 to a biofilm and visualized the interaction with OCT. Due to the measurement speed it has been demonstrated that OCT can be used to measure even faster processes, such as changes in porosity during deformation (Blauert *et al.*, 2015). This allowed to use OCT not only as imaging tool, but to quantify structural changes of the biofilm matrix. The general advances of imaging opened the field of biofilm mechanics using image analysis. The advantages to measure mechanical properties over other macroscopic techniques, such as compression measurements (Körstgens *et al.*, 2001a), rheometer creep analysis (Towler *et al.*, 2003), or fluid dynamic gauging (Möhle *et al.*, 2007), is that the biofilm is not necessarily destroyed during the measurement procedure. Macroscopic techniques test biofilm structures in the *mm* to *cm* range, measuring average mechanical properties. Exactly these properties might vary locally in the biofilm matrix. For material properties such as the Young's or the shear modulus a wide range of values is reported in the literature, ranging from a few *Pa* up to a few *kPa*. Böhl *et al.* (2013) and Guélon *et al.* (2011) gave a good overview about the variances of mechanical property measurements for biofilms. A clear need for measuring local material properties is present. Since biofilms are heterogeneous materials, cultivation under different conditions may exhibit different mechanical properties. Therefore, it is essential to narrow down the range of the mechanical properties.

As a result of the scarcity of experimental data, any reported mechanical properties are valuable and used extensively by modeling studies. Otherwise, the outcome of these seemingly conclusive studies is data which differs from reality. Therefore, reliable experimental data is needed in order to produce meaningful results. Simulation studies

improved the understanding and estimation of structural features, biofilm growth, and interaction with the environment. Horn and Lackner (2014) reviewed this in detail and more information can be found there. The structural shape of the simulated biofilm geometry has a great impact on the fluid-structure interaction and substrate conversion. The models need experimental data and real geometries to improve the model assumptions. The mechanical properties measured in experiments were implemented into theoretical models, to reproduce the observations. Alpkvist and Klapper (Alpkvist and Klapper, 2007a) were the first to include mechanical properties in a moving biofilm geometry. They used a ball and spring model to simulate a moving biofilm matrix geometry. A great achievement was the implementation of 3D confocal laser scanning microscopy images to simulate shear stress onto the biofilm structure and detachment (Böl *et al.*, 2009). Recently OCT images were introduced in modeling studies, providing real geometries on the mesoscale (Martin *et al.*, 2014, Fortunato *et al.*, 2016, Li *et al.*, 2016) Implementing real structures, together with experimental data from OCT deformation experiments, will significantly improve the quality of modeling studies and possibly lead to a new understanding of the mechanical nature of biofilms.

Table 1: Overview shear and Young's modulus of biofilms.

Method	Range [Pa]	Bacteria culture	Reference
shear modulus G			
Fluid shear	27	mixed culture	Stoodley <i>et al.</i> (1999c)
Fluid shear	29	mixed culture	Blauert <i>et al.</i> (2015)
Fluid shear	0.9 - 5	<i>S. aureus</i> (EX265)	Rupp <i>et al.</i> (2005)
Fluid shear	0 - 280	<i>P. aeruginosa</i>	Stoodley <i>et al.</i> (2002)
Rotating disc	0.3 - 45	mixed culture	Towler <i>et al.</i> (2003)
Rotating disc	190 - 380	<i>S. mutans</i>	Vinogradov <i>et al.</i> (2004)
Rotating disc	1400	mixed culture	Houari <i>et al.</i> (2008)
Young's modulus E			
Fluid shear	40	mixed culture	Stoodley <i>et al.</i> (1999c)
Fluid shear	36	mixed culture	Blauert <i>et al.</i> (2015)
Fluid shear	1 - 33	<i>Desulfovibrio sp.</i> (EX265)	Stoodley <i>et al.</i> (2001b)
Fluid shear	65	<i>P. aeruginosa</i> (PAO1)	Klapper <i>et al.</i> (2002)
Fluid shear	20 - 240	<i>P. aeruginosa</i> (PAO1)	Stoodley <i>et al.</i> (1999c)
Fluid shear	1 - 336	<i>P. aeruginosa</i> (PAO1)	Stoodley <i>et al.</i> (2001b)
Fluid shear	3	<i>P. aeruginosa</i> (FRD1)	Klapper <i>et al.</i> (2002)
Compression	17 - 62	<i>S. oralis</i> (J22)	Paramonova <i>et al.</i> (2009)
Compression	18 - 19	<i>A. naeslundii</i> (TV14-J1)	Paramonova <i>et al.</i> (2009)
Compression	30 - 140	mixed culture	Paramonova <i>et al.</i> (2009)
Compression	30 - 180	dental plaque	Paramonova <i>et al.</i> (2009)
Compression	20 - 280	<i>C. albicans</i> (Caf2-1)	Paramonova <i>et al.</i> (2009)
Compression	120	<i>C. albicans</i> (Chk23)	Paramonova <i>et al.</i> (2009)
Compression	210 - 310	<i>C. albicans</i> (Chk24)	Paramonova <i>et al.</i> (2009)
Compression	40	<i>C. tropicalis</i> (GB 9/9)	Paramonova <i>et al.</i> (2009)
Compression	30	<i>C. parapsilosis</i> (GB 2/8)	Paramonova <i>et al.</i> (2009)
Compression	1100	<i>S. epidermidis</i>	Hohne <i>et al.</i> (2009)
Compression	3300	<i>K. pneumoniae</i>	Hohne <i>et al.</i> (2009)
Compression	6500	<i>P. aeruginosa</i>	Körstgens <i>et al.</i> (2001b)
Indentation	1000 - 8000	<i>S. mutans</i>	Cense <i>et al.</i> (2006)
Indentation	700000	<i>S. carlsbergensis</i>	Alsteens <i>et al.</i> (2008)
Indentation	2300000	<i>S. cerevisiae</i>	Alsteens <i>et al.</i> (2008)
Indentation	600000	<i>S. cerevisiae</i>	Touhami <i>et al.</i> (2003)
Indentation	6100000	<i>S. cerevisiae</i>	Touhami <i>et al.</i> (2003)

Motivation

For a long time now biofilms are classified as viscoelastic materials. However, it is of utmost interest to dig deeper into the elastic nature of biofilms, in order to understand deformation processes in detail. It is the elastic part, which defines whether the biofilm will absorb the stress and deform or detach. This understudied area of biofilm research can only be investigated with fast, non-invasive methods measuring the deformation *in situ*. This is the exact strength of optical coherence tomography. Unlike other imaging techniques OCT is capable of visualizing the internal structure of biofilms, opening a field of dynamic process analysis never seen before. Before, processes such as porosity, thickness, or surface roughness change were correlated to deformation without knowing the *in situ* details. Here OCT can give an exact insight into the deformation process, revealing changes of the geometry and intrinsic parameters. For that methods to estimate mechanical properties from image analysis were developed. This includes the evaluation of the shear, Young's, as well as the bulk modulus. For the first time the bulk modulus and its inverse, the compressibility, were evaluated for a biofilm system. Compressed and drained biofilms change their physical appearance and will have an impact on industrial processes, such as membrane reactors, for which it influence the process strategy. The experiments further allow to measure and estimate a value for the Poisson's ratio, an unknown parameter, considered to lie in a positive range. The methods developed here show that biofilms indeed should be considered auxetic materials. This changes the impression we have about the elastic nature of biofilms and has direct consequences for theoretical studies of biofilm systems. In fluid-structure interaction simulations the experimental data was used to qualitatively describe the stress within the biofilm during deformation. Little data is available from real biofilm geometries to understand the processes connected to the elastic deformation. It can be shown that elastic deformation can be well simulated from real biofilm geometries and that simple models can even reveal implicit processes, which were not expected per se. This thesis aims to demonstrate the importance of elastic deformation processes for biofilm research. This understudied area still surprises magnificently in each and every detail, presenting biofilms in a completely new light.

2 Materials and methods

2.1 Biofilm cultivation

Biofilms were cultivated in flow cells made of poly-oxymethylene (POM). The dimensions of the flow channel was ($W \times H \times L$) : $2 \text{ mm} \times 1 \text{ mm} \times 124 \text{ mm}$. A peristaltic pump (Ecoline IPC, Ismatec, Weinheim, Germany) was used to deliver a cultivation medium towards the biofilm. The experimental setup is shown in Fig. 1. The cultivation medium

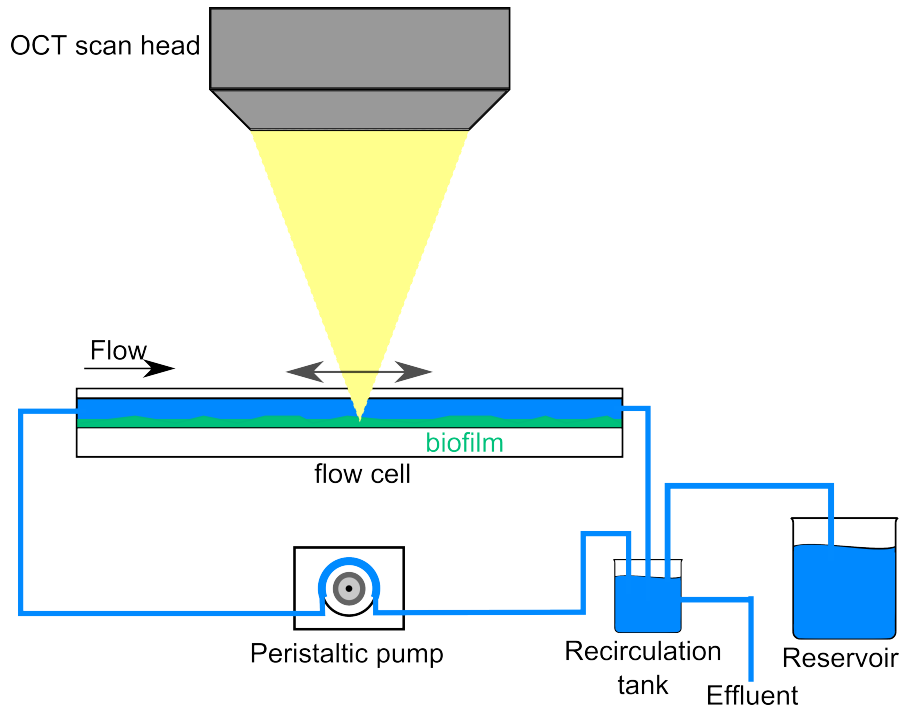


Figure 1: Experimental setup with the biofilm forming in the flow channel. The peristaltic pump delivers nutrients from the recirculation tank, which is exchanged four times per day from the reservoir. Biofilm visualization was done from top by optical coherence tomography (OCT).

was pumped in recirculation mode from a recirculation tank. The exchange rate was set to four times per day. The flow cells were inoculated with fresh activated sludge supernatant from a local waste water treatment plant (Karlsruhe, Germany), which was pre-filtered with a $12 - 15 \mu\text{m}$ filter (Filter 301, VWR International, Radnor, USA). 20 mL of the inoculum was added to the recirculation tank and remained in the system for one day, before the cultivation medium was exchanged four times per day from the reservoir.

2.1.1 Hydrodynamic conditions during cultivation

Flow cells provide a good system to have stable and controlled hydrodynamic conditions. To study the influence of fluid flow on biofilm formation and its mechanical properties, mean volumetric flow rates between $1 - 42 \text{ mL/min}$ were investigated. This translates to Reynolds numbers between $Re = 11 - 472$. Flow cell hydrodynamics were calculated according to Stoodley *et al.* (2001a), assuming fully developed laminar flow through a rectangular flow channel. The Reynolds numbers Re were calculated from the following equation:

$$Re = \frac{u_{mean} \cdot D_h}{\nu_k} \quad (1)$$

where ν_k is the kinematic viscosity of water at $20 \text{ }^\circ\text{C}$, and u_{mean} is the mean flow velocity in the empty channel. u_{mean} is calculated from eq. 2 with the mean volumetric flow rate Q , which is measured during the experiments.

$$u_{mean} = \frac{Q}{W \cdot H} \quad (2)$$

The hydraulic diameter D_h was derived from the width (W) and height (H) of the flow channel:

$$D_h = \frac{4 \cdot H \cdot W}{2 \cdot (H + W)} \quad (3)$$

However, over time biofilm covers the walls, which does influence the cross-section of the flow channel slightly. For simplicity it was assumed that the coverage did not influence the flow rate and therefore the shear stress. Biofilm structures were visualized from top by optical coherence tomography (OCT, indicated in Fig. 1). The system was designed in a way that biofilm formation was followed over time non-invasively and *in situ*. To assure that biofilms formed under fully developed laminar flow, OCT images were acquired at a distance of $70 - 80 \text{ mm}$ from the entrance. To determine the length of the channel necessary to develop a laminar flow profile, following assumption of the entrance length L_e was used:

$$L_e = 0.06 \cdot Re \cdot d \quad (4)$$

Assuming a maximal diameter of $d = 2 \text{ mm}$ for the flow channel, the entrance length at the highest Reynolds number ($Re = 472$) was calculated to be $L_e = 57 \text{ mm}$. Therefore, a fully developed laminar flow could be assumed at the imaging position.

2.1.2 Cultivation of biofilms

For deformation experiments various biofilms were cultivated with one of three substrates as sole carbon source: Na-acetate, D-glucose, or L-phenylalanine. Each substrate was supposed to have a different influence on the EPS network. The hypothesis was that biofilms cultivated with glucose embed more polysaccharides compared to biofilm cultivation with acetate or phenylalanine. The difference in the composition of the EPS was expected to influence the stability of the biofilm matrix, hence change the value the material properties. The cultivation medium included additional nutrients and trace elements to assure sufficient nitrogen and phosphor for the biofilms (listed in Table 2). The recirculation tank was constantly aerated to assure an oxygen concentration of $\sim 8 \text{ mg/L}$. Nine flow cells were cultivated in parallel to have triplicates for each Reynolds number. Biofilms were cultivated until either the biofilm structures were visibly large enough for deformation experiments, or the cultivation condition was expected to prevent further biofilm formation in a given time.

Table 2: Composition of the cultivation medium with varying substrates for the experiments. The cultivation medium was composed of a specific substrate, nutrient composition, as well as trace elements.

	$\beta_s \text{ [mg} \cdot \text{L}^{-1}]$		$\beta_s \text{ [}\mu\text{g} \cdot \text{L}^{-1}]$
Substrates		Trace elements	
Na-Acetate	20-30	H_3BO_3	300
D-Glucose	24-30	$CoSO_4 \cdot 7H_2O$	130
L-Phenylalanine	40	$CuCl$	8
		$ZnSO_4 \cdot 7H_2O$	56
Nutrients		$MnSO_4 \cdot H_2O$	20
K_2HPO_4	2	$Na_2MoO_4 \cdot 2H_2O$	26
$(NH_4)_2SO_4$	12	$NiCl_2 \cdot 6H_2O$	10
$MgSO_4 \cdot 7H_2O$	12		
$Ca(NO_3)_2 \cdot 4H_2O$	8		
$FeSO_4 \cdot 7H_2O$	6		
$NaHCO_3$	buffer to pH = 7		

Various biofilms were cultivated under different cultivation conditions (e.g. different substrate or Reynolds number) for the deformation experiments.

Table 3: Cultivation conditions for all biofilms.

substrate	substrate concentration [<i>mg/L</i>]	Reynolds number during cultivation [–]	Number of experiments [–]
Acetate	20	11 – 472	15
Acetate	30	165	3
Glucose	24	11 – 472	15
Glucose	30	4	3
Phenylalanine	40	11 – 472	15

Table 3 lists all biofilms cultivated for the experimental part. However, only biofilm patches with sufficient large structure were chosen for deformation experiments to determine material properties. From all performed experiments only a selection of biofilms could be shown and discussed in detail. Table 4 lists the biofilms which are shown in figures and implemented in simulations in this thesis, together with the substrates used and flow conditions set during cultivation.

Table 4: Cultivation conditions for biofilm presented in this thesis as images or structural templates for FSI simulations.

Biofilm	Substrate	Substrate concentration [mg/L]	Reynolds number during cultivation [–]	Chapter
I	Gl	30	4	3.2.1
II	Gl	30	4	3.2.1
III	Gl	30	4	3.2.1
IV	Gl	30	4	3.2.2
V	Ac	30	165	3.2.3
VI	Ac	20	137	3.3.1
VII	Gl	24	55	3.4.6
VIII	Ac	20	11	3.4.6
IX	Gl	24	55	3.4.6

2.2 Optical coherence tomography (OCT)

Optical coherence tomography (OCT) was invented by Huang *et al.* (1991) as a non-destructive imaging method to visualize the retina of the eye. Originally used in ophthalmology (Kitchens *et al.*, 2005, Broecker and Dunbar, 2005, Cabrera *et al.*, 2006), OCT systems showed promising features for clinical applications in dermatology (Steiner *et al.*, 2003, Gelikonov and Gelikonov, 2006) or integrated in an endoscope to check the interior of the body, such as lung tissue (Tsuboi *et al.*, 2005). Xi *et al.* (2006) were the first to adapt OCT imaging for 3D biofilm visualization on a larger scale (mesoscale). The penetration depth of 1 mm allowed for the first time to visualize and understand the deeper layers of the biofilm matrix *in situ*, and following biofilm formation over time. The strength of OCT to acquire images fast was captured by Haisch and Niessner (2007), when they added H_2O_2 to a biofilm system and visualized the interaction of the chemical with the biofilm matrix. These 'transient processes' of solving the matrix showed the possibility of dynamic imaging with OCT. Wagner *et al.* (2010b) were the first to put OCT in context of another elaborated visualization technique, namely confocal laser scanning microscopy (CLSM). They found OCT to be quite suitable to measure biofilm thicknesses reliably, if light penetration is not limited. Further biofilm studies included membrane systems (Dreszer *et al.*, 2014b, West *et al.*, 2015), or dynamic changes within the biofilm matrix due to deformation (Blauert *et al.*, 2015). To visualize biofilm formation and deformation a spectral domain optical coherence tomograph (GANYMEDE I, Thorlabs GmbH, Lübeck, Germany) was used. The principle of a spectral domain (SD-) OCT is a Michelson interferometer experiment in which the reference mirror is fixed and a broadband light source is used to generate an interference pattern. This is a faster way to generate the interference signal compared to time domain (TD-) OCTs. The TD-OCTs use a reference mirror, which moves forth and back in time to generate an interference pattern. Details about OCT design and application can be found in Drexler and Fujimoto (2015) or Fercher *et al.* (2010). SD-OCT measures depth-resolved intensity profiles (OCT A-scan) from translucent samples such as biofilms. As shown in Fig. 2, a broadband super luminescent diode (SLD) with a central wavelength of $930 \pm 80 \text{ nm}$ is used as light source in a Michelson interferometer. The light is split at the beam splitter into the reference and the sample arm. Through the sample arm, the light penetrates the sample and is reflected. The reflected light superimposes with the light from the reference arm and creates an interference pattern. This interference pattern is transformed via a fast Fourier transformation into a depth-resolved intensity signal for one spot (z-axis). By acquiring several scans along one lateral axis (x-axis is along the flow direction), a cross-sectional image through the biofilm structure is produced in the xz-plane (OCT B-scan). Consecutive cross-sections along the other lateral axis generate a volumetric representation (OCT C-scan), as detailed in (Haisch and Niessner, 2007, Wagner *et al.*, 2010b, Xi *et al.*, 2006). This 3D data-set is called a stack of cross-sections. OCT is suitable for *in situ* biofilm imaging at the mesoscale

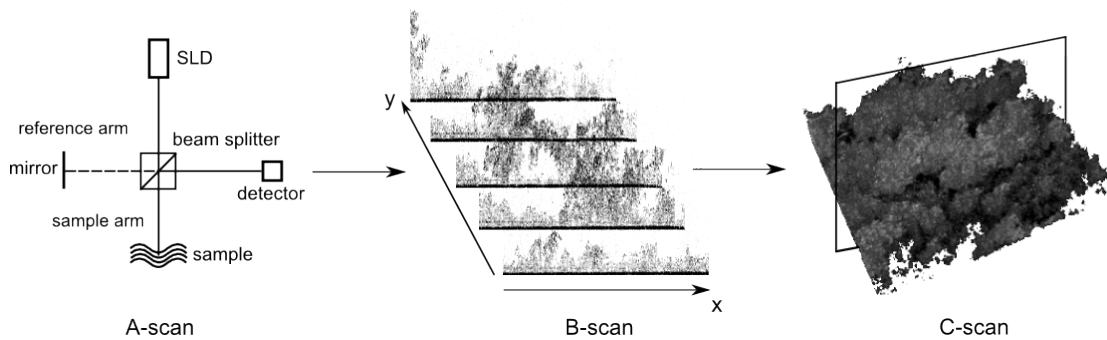


Figure 2: Principle of SD-OCT. Left: scheme of the measurement using a Michelson interferometer setup, middle: series of cross-sections, right: combination of several cross-sections to form a volumetric representation of the biofilm. Taken from Blauert *et al.* (2015).

(e.g., millimeter scale) (Morgenroth and Milferstedt, 2009). It is a non-invasive technique since no staining or other preparation is required, and acquires imaging data-sets fast. Cross-sections are obtained within milliseconds and full volumetric representations can be visualized within seconds. This allows OCT to follow fast processes over time either in real time (for 2D cross-sections) or in time-lapsed mode (for 3D volumetric representations). The lateral field of view is $10\text{ mm} \times 10\text{ mm}$ (using a LSM03 lens), with an axial resolution of < 5.8 and $8\ \mu\text{m}$ in the lateral dimension (both in air). Since only reflecting materials show a signal, voids are reliably displayed. The detection of voids depends on the resolution of the imaging device. Therefore, only voids $\sim 50\ \mu\text{m}^2$ (1 pixel) are detected as empty space. Furthermore, a stack of OCT cross-sections in the xz -plane can be resliced horizontally to a stack of cross-sections in the xy -plane. This creates a series of z -cross-sections, similar to confocal microscopy images, which are slices through the biofilm structure from top. The main usage of these reslices is the creation of z -projections, a color coded topography of the bulk-biofilm interface. This helps to easily visualize biofilm formation in 3D on a 2D image.

2.3 OCT settings for cultivation and deformation experiments

Deformation experiments were performed in the same flow-cells used during the cultivation. Fig. 1 shows the position of the OCT device placed above the flow cell. For higher fluid flows during the deformation experiments a separate peristaltic pump (Ecoline VC-MS/CA8-6, Ismatec, Weinheim, Germany) was used. In deformation experiments two different imaging modes of the OCT were used to investigate mechanical properties. Due to the fast image acquisition it is possible to measure real time processes in dynamic mode, or slower processes in a time-lapsed mode. For a better understanding of the performed experiments, it has to be stated that the term dynamic is used for experiments in which the time between consecutive cross-sections is short compared to the time it takes to acquire a single cross-sectional scan (t_1 is larger than Δt , see Fig. 3). In time-

lapsed experiments the time between consecutive acquired cross-sections or volumetric scans is much longer compared to the acquisition time of a single scan (t_1 is smaller than Δt). In consequence, time series of cross sections can be dynamic or time-lapsed, while volumetric representations are always time-lapsed measurements.

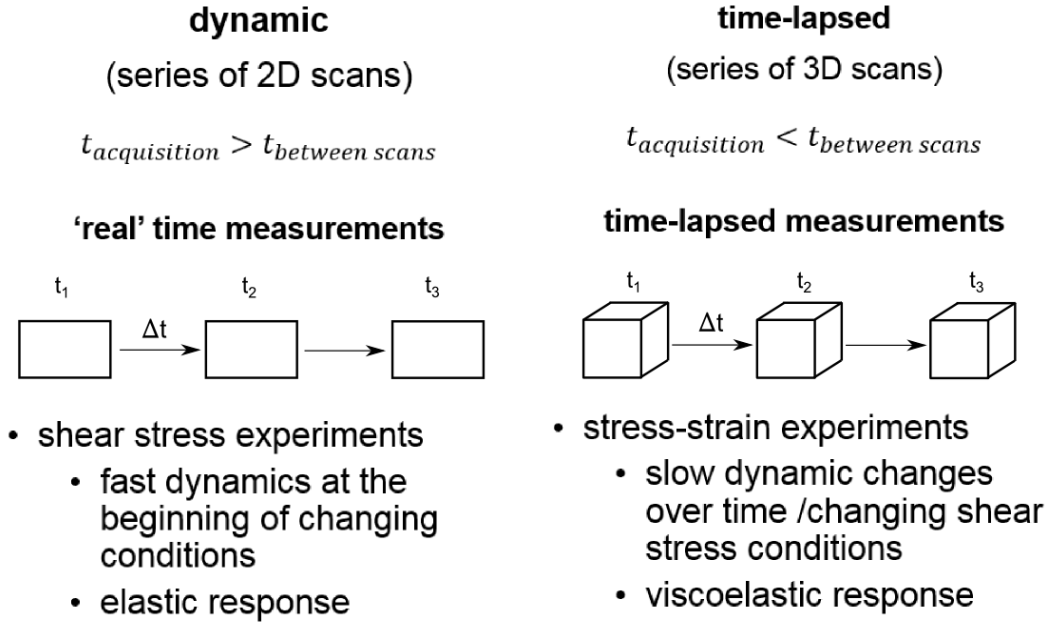


Figure 3: OCT is capable of imaging with different modes. Dynamic images are acquired when the time t between consecutive cross-sections is short compared to the time it takes to acquire a single cross-sectional scan. If the time d between consecutive acquired cross-sections or volumetric scans is much longer compared to the acquisition time of a single scan, the OCT mode is termed time-lapsed.

2.3.1 Dynamic deformation experiments

In dynamic deformation experiments the impact of a changing shear stress onto the biofilm structure was investigated. This allowed to investigate fast dynamic processes and elastic deformation processes of biofilms. For shear stress induced experiments, biofilms were cultivated in flow cells as described in section 3.3.1. The investigated structures were either round and patchy, or flat and streamer-like shaped. The OCT was set to measure cross-sections along the flow in the center of the flow channel, to reveal the inner structure of the biofilm and its change during deformation. The OCT scan rate was set to 10,000 A-scans/s for enhanced image quality, acquiring cross-sections of $2.00\text{ mm} \times 1.46\text{ mm}$ ($1,024\text{ pixel} \times 700\text{ pixel}$) along the flow within 100 ms (10 frames/s). Each acquired cross-section therefore consisted of 1,024 A-scans. This implies a theoretical resolution of $\Delta x \approx 2\ \mu\text{m}$ in the lateral, and an axial resolution of $\Delta z = 2.1\ \mu\text{m}$ (in water). These settings result in a higher theoretical resolution than the physical resolution itself, which is called oversampling. Oversampling can increase the

resolution. At the beginning of the experiment the peristaltic pump was turned off (e.g. no shear stress). The flow velocity was set and the pump was turned on for 10 s (full shear stress). During the 10 s the volumetric flow (Q) was measured and the mean flow velocity u_{mean} was calculated from eq. 2. Within the 10 s fluid flow, the elastic biofilm deformation occurred. The pump was turned off and the relaxation was recorded.

The shear stress τ acting on the biofilm boundary was estimated from Stoodley *et al.* (2001a):

$$\tau = \frac{6 \cdot \eta \cdot u_{mean}}{D_h} \quad (5)$$

with η the dynamic viscosity of water at 20 °C. Here, it needs to be stressed that the shear stress τ was approximated from the wall shear stress, assuming an ideal fully developed laminar flow between two infinite parallel plates. Therefore, τ does not account for local disturbances of the fluid flow by the heterogeneity of the biofilm structure and movement of the biofilm itself. However, it is still a good evaluation of the stress acting on the biofilm structure from experimental measurements and allows to compare results with existing measurements, e.g. (Stoodley *et al.*, 1999c,a). In this thesis a better estimation to describe the stress conditions at the bulk-biofilm interface was investigated by including real biofilm geometries in fluid-structure interaction simulations (FSI). The shear stress was then evaluated from computational fluid-dynamics, which gave a better estimation of the shear stress. Therefore, eq. 5 was used in section 3.2 in which the methods to measure mechanical properties from biofilms were introduced. In section 3.3 shear stress assumptions based on FSI simulations were used.

2.3.2 Time-lapsed experiments

Since viscoelasticity is a time-dependent process, time-lapsed experiments can reveal the viscoelastic nature of biofilms when exposed to shear stresses for a longer period of time, e.g. several minutes to hours. In stress-strain experiments biofilms were exposed for a duration of 36 min to incrementally increasing (load cycle) and decreasing shear stresses (unload cycle). Figure 4 gives an overview over the experiment, indicating OCT measurements with arrows. Similar to shear stress induced experiments, the pump was turned off at the beginning of the experiment. The flow velocity was then increased every 120 s in steps, until a maximum was reached. In the first 60 s the biofilm adapted elastically to a new shear stress. After these 60 s a 3D OCT scan was acquired. After a total of 120 s the next flow velocity was set and the experiment continued until the maximum flow velocity was reached. The maximum flow velocity occurred at the expected transition time from elastic to viscoelastic deformation of 18 min (Shaw *et al.*, 2004). The experiment followed the same procedure with the incremental decrease of the flow velocity until the flow was stopped. In this unload cycle the viscoelastic nature prevailed. Stress-strain experiments were performed at shear stresses ranging from $\tau = 0 - 5 Pa$. During the experiment the imaged volume was $2.00 mm \times 2.00 mm \times 1.46 mm$ ($500 \times 500 \times 700 voxel$). These settings were also used during biofilm cultivation to keep

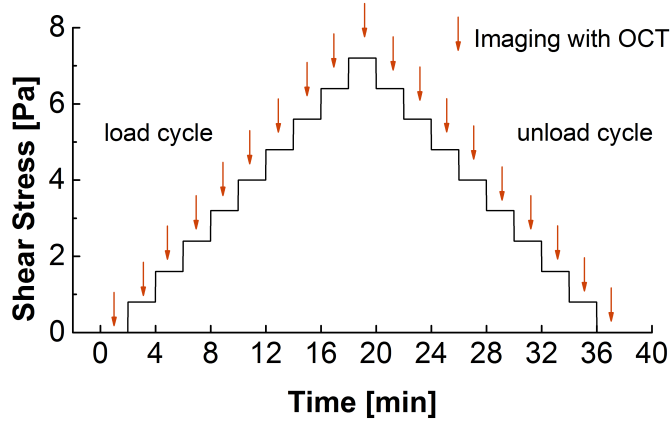


Figure 4: Stress-Strain Scheme for the time-lapsed experiments. A new shear stress was set every 120 s. The shear stress was incrementally increased in the load cycle and decreased in the unload cycle. The biofilm adapted to the new environment for 60 s at each shear stress, followed by a 3D OCT scan (arrows).

the same position during cultivation and deformation experiments. During cultivation an A-scan averaging of $n = 10$ was set to capture a clear volumetric representation, increasing the signal-to-noise ratio. During the deformation experiment the averaging had to be set to $n = 3$ to reduce the acquisition time to 36 s. This was a necessary step in order to stay in the 60 s imaging window before a new shear stress was set. These data-sets were the basis for the calculation of the strain (Young’s modulus) and angle of deformation (shear modulus). Shear stresses were calculated similar to shear induced experiments, by measuring the mean volumetric flow rate Q in each step of the stress-strain experiment.

2.4 OCT data-set analysis

OCT data-sets were processed using the software Fiji 1.52d (Schindelin *et al.*, 2012). Structural properties of the biofilm geometry were extracted from the OCT data-sets by *in-house* macros, containing the calculations explained in the following section. The macros allowed to follow intrinsic changes of the biofilm matrix during cultivation and deformation experiments.

2.4.1 OCT data processing

OCT data-sets were acquired as 32-bit images and were converted to 8-bit TIFF-files for further data processing. The 3D data-set consists of a collection of several cross-sections, which build up the volumetric representation. This is called an image ‘stack’. Each cross-section can be processed separately in the stack. Thresholding and separation of signal and noise were processed with the whole stack, while structural parameters were identified from single cross-sections and averaged over the stack. Dynamic exper-

iments, in which fast processes were investigated, were acquired as an image sequence of cross-sections. The 2D data-sets in which each cross-section represents the structure at a different time are similar to a video film. Parameters are calculated similar to the 3D data-sets, but not averaged, since each cross-section represents the structure at a different time. Biofilm signals have grey-values close to the mean value of the noise. This creates problems to remove the noise via conventional thresholding methods. For conventional images a method dependent value is set, which defines pixels with a value smaller than the threshold as background (pixel value 0), and pixels with values equal or higher than the threshold as biofilm structure (pixel value 1). Thresholding methods often make decisions based on the histogram of the image, e.g. Otsu (1979). In OCT images the noise distribution often overlaps with the biofilm signal, making it impossible to use conventional thresholding methods. For reliable biofilm structure recognition noise was first reduced by Fiji's Brightness/Contrast method, based on the mean intensity value of the image histogram. For almost all OCT images a mean value +5 was sufficient to erase enough of the noise to move to the next step. A wrong identified threshold value occurs approximately only 1 in 300. In the prepared image the biofilm structure was then identified with a Fiji plugin: 'Find Connected Regions'. The tool identifies reliable connected structures of a defined minimal volume. Structure recognition always started at the bottom of the flow channel (substratum). This includes the biofilm which formed on the bottom of the flow cell. Problems may occur in flow cells where the top of the flow channel is covered with biofilm. This limits the identification of biofilm thickness and porosity. Here an alternative is to analyze only a part of the flow cell in order to exclude overgrowth of the walls. The output of the plugin was a binary image of 0's and 1's, ready for further image processing. The pre-processed images were cropped to the minimal size possible without losing biofilm-related information. The structural parameters calculated from single cross-sections are given below. Image preparation for the determination of biofilm deformation from the stress-strain experiments required to extract cross-sections of the same position for different flow velocities. Stacks of the undeformed biofilm geometry, deformed at medium shear stress, and deformed at highest shear stress, were compared with Fiji's 'Compare Stack' plugin. This allows to view the same cross-sections simultaneously at three different shear stresses. Cross-sections with a clear biofilm structure were extracted for each shear stress and formed a new stack. This new stack contained cross-sections of the same position during the stress-strain experiments. This stack was used to measure the angle of deformation as well as elongation of the biofilm structure (explained below).

2.4.2 Mean biofilm thickness

The mean biofilm thickness \bar{L}_F of each OCT cross-section was calculated from the following equation:

$$\bar{L}_F = \frac{1}{N} \sum_{i=1}^N L_{F,i} \quad (6)$$

where $L_{F,i}$ is the biofilm thickness from a single A-scan i in the corresponding cross-section and N is the total number of A-scans (columns of pixels in the image). The biofilm thickness $L_{F,i}$ is the highest point detectable above the substratum in the corresponding A-scan. All signals detected below this point are treated as either biomass (intensity = 1) or void (intensity = 0). The average thickness of all A-scans in the corresponding cross-sections equals the mean biofilm thickness \bar{L}_F . In dynamic deformation experiments the thickness change in each cross-section was compared. For the volumetric scans the thicknesses of the 3D structure were averaged for the whole stack and stacks for different shear stresses were compared. This offers the possibility to monitor a change of the biofilm structure (e.g. compression or formation) during the experiments.

2.4.3 Surface roughness coefficient

The surface roughness coefficient R_a^* of the biofilm was calculated according to Murga *et al.* (1995):

$$R_a^* = \frac{1}{N} \sum_{i=1}^N \frac{|L_{F,i} - \bar{L}_F|}{\bar{L}_F} \quad (7)$$

where i represents a particular A-scan and N is the overall number of A-scans in a cross-section. This value is comparable to the variation of the biofilm thickness over the mean biofilm thickness. Biofilms with a smooth surface and only few variations from the mean biofilm thickness have low values close to 0. The higher the roughness coefficient, the more variations of the biofilm surface structure are expected. These values can be larger than 1 if an area is imaged which is not evenly covered.

2.4.4 Biofilm porosity

OCT is unique in measuring porosity reliable and non-invasive. In the experiments conducted, the development of the porosity was recorded until stress-strain experiments were performed. Lewandowski (2000) stated the problem with porosity quite accurate: "However, biofilm matrix is not solid, it is a highly hydrated gel and this difference is the source of our difficulties. Simply put, if the biofilm matrix itself is more than 90% water, then how can we distinguish the water within the matrix as different from the water in the pores?". In literature a wide variety of porosity values are discussed. Most biofilm studies rely on dry mass measurements (Zhang and Bishop, 1994, Bishop *et al.*, 1995, Lewandowski, 2000) or image based calculations (Yang *et al.*, 2000, Wagner *et al.*, 2010b). In dry mass experiments the water content of the biofilm matrix is

measured by weighting the moist and dry biofilm matrix. The fraction of water content to moist biomass results in the porosity. These calculations can overestimate biofilm porosity because water, which is embedded in the EPS as hydrogel, is accounted for, too. Calculation of the porosity should only include vacant spaces in the EPS matrix, filled with water. Furthermore, in dry mass calculations the biofilm is destroyed in the measurement, making it impossible to follow changes during the cultivation. Imaging techniques have drawbacks, too. Beyenal *et al.* (2004) showed that calculation of intrinsic parameters vary with resolution and image processing technique. They concluded that only changes should be monitored with imaging techniques. OCT is the right imaging method to fulfill the demand of non-invasively following changes over time. Due to the resolution of the OCT the calculated porosity is considered as macro-porosity, compared to porosities calculated from confocal laser scanning microscopy images (which have higher resolution) or dry mass measurements (measuring the water content of the biofilm matrix). The biofilm macro-porosity Φ is the ratio of identified voids (A_{voids}) to the total biofilm signals ($A_{biofilm}$) in the corresponding cross-section. In this study, the biofilm macro-porosity excludes background signals above the bulk-biofilm interface. Biofilm macro-porosity is thus the ratio of void signals inside the biofilm to the total area of the biofilm containing both, biomass and voids.

$$\Phi = \frac{A_{voids}}{A_{biofilm}} = \frac{A_{voids}}{A_{biomass} + A_{voids}} \quad (8)$$

Increase or decrease of the macro-porosity during cultivation gives a hint of the density of the developing structures. Unlike other methods, such as gravimetric porosity or porosity calculated from confocal laser scanning microscopy images, OCT does not alter the structure during preparation or relies on staining (i.e. estimating the stained signals), providing a more reliable method to determine this value.

2.5 Mechanical properties of biofilms

Biofilms are complex heterogeneous materials which deform when a stress is applied onto the biofilm structure. Local variations within the biofilm matrix makes it extremely difficult to describe the deformation process in detail. In deformation or compression tests the material's response to an applied force is quantified by mechanical properties, describing the material as one entity. Elastic as well as viscoelastic deformation occur in biofilms as pictured in Fig. 5.

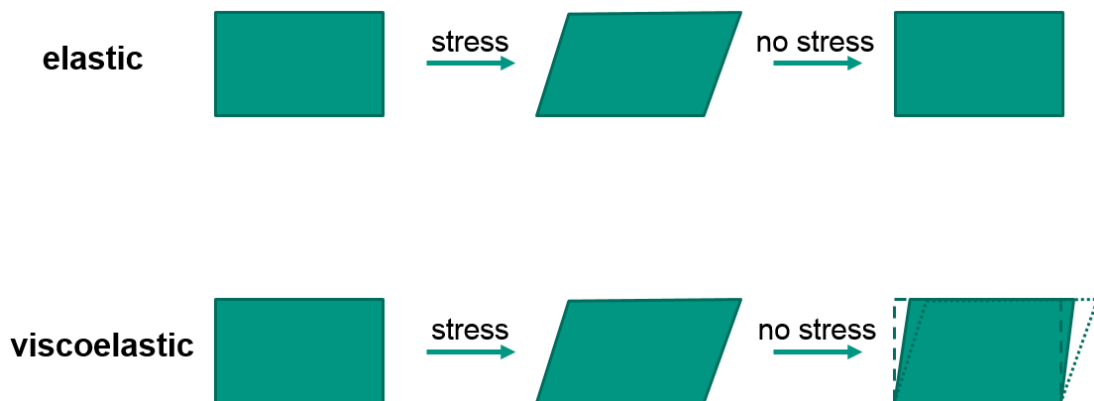
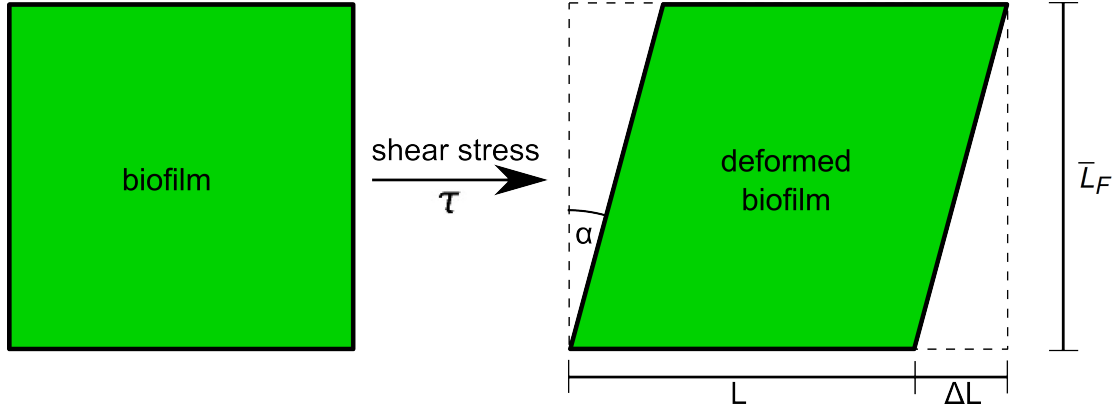


Figure 5: Elastic and viscoelastic deformation in biofilms depend on the duration of the applied stress. Biofilms exposed to a stress for a short time (seconds to a few minutes) show elastic deformation. If the stress is removed the biofilm regains its original conformation fast. For longer duration of stress, the biofilm stays in a deformed state for some time after the stress is removed.

Is the duration of the applied stress on a biofilm short (seconds to minutes), elastic deformation occurs. Elastic materials regain their original conformation immediately after an invoking stress is released. Rubbers are best known for this behavior. However, if the duration of stress continues, viscoelastic deformation occurs in biofilms. Viscoelastic materials possess not only the ability for elastic deformation, but also show a viscous flow behavior if the stress persists. Over time the solid material will flow like a liquid and gain a deformed geometry. This altered geometry stays deformed until the stress is released and slowly regains its conformation over time (Banks *et al.*, 2011). As a consequence of the stress duration investigated in the deformation experiments the biofilm matrix was considered to behave as an ideal homogeneous isotropic and elastic material. Which means that the material shows the same elastic response regardless of the orientation of the applied stress. To access mechanical properties of biofilms, OCT images of relaxed biofilms (without flow) and under (full) deformation were compared. The deformation of the biofilm was investigated independently for each cell. Elastic deformation can be quantified by three mechanical moduli. The shear modulus G , Young's modulus E , and bulk modulus K . All three mechanical moduli are related to each other through the Poisson's ratio ν (Lubliner and Papadopoulos, 2017, Vincent, 2012).



angle of deformation	elongation	mean biofilm thickness
α	ΔL	\bar{L}_F
shear modulus	strain	Young's modulus
$G = \frac{\tau}{\alpha}$	$\varepsilon = \frac{\Delta L}{L}$	$E = \frac{\tau}{\varepsilon}$

Figure 6: Shear stress induced structural changes are used to measure and calculate mechanical properties. Important properties in biofilm research are the angle of deformation α , the shear modulus G , and the Young's modulus E .

Material properties are derived from Hooke's law assuming an ideal elastic homogeneous material. Hooke's law states that a force F , needed to compress or extend a spring (elastic material), is proportional to a distance X and a spring constant k :

$$F = k \cdot X \quad (9)$$

The mechanical properties of interest for biofilm deformation are the shear modulus G and the Young's modulus E (see Fig. 6). The shear modulus, or modulus of rigidity, is defined as the ratio of shear stress τ along the fluid flow (the force F) to the shear strain γ (the distance X):

$$G = \frac{\tau}{\gamma} = \frac{\tau}{\tan(\alpha)} \approx \frac{\tau}{\alpha} \quad (10)$$

The shear strain γ can be expressed with the change in the angle of deformation α (in radians). It describes the tendency of materials to withstand viscous stresses. For small deformations, which usually occur, the equation can be simplified by assuming $\tan(\alpha) \approx \alpha$. The higher the shear modulus, the stiffer the material. The Young's modulus E , or modulus of elasticity, is defined in a similar way by relating tensile stress σ_T to the strain ε :

$$E = \frac{\sigma_T}{\varepsilon} \quad (11)$$

The Young's modulus for homogeneous materials is typically measured by stretching the

material (tensile stress) and measuring the relative elongation (strain) along the flow as the fraction of elongation ΔL to the original length L :

$$\varepsilon = \frac{\Delta L}{L} \quad (12)$$

This engineering (or Cauchy) strain is used in small deformations. The engineering strain requires the displacement field v and the displacement gradient ∇v to be small compared to unity, i.e. $v \ll 1$ and $\nabla v \ll 1$. To simplify the complex situation of real biofilms the strain was assumed to be uniform throughout the body, and the (tensile) stress stretching the biofilm is the shear stress τ .

$$E \approx \frac{\tau}{\varepsilon} \quad (13)$$

This is a simplified assumption used in flow cell experiments to estimate the normal stresses stretching the biofilm along the flow. Stoodley *et al.* (1999b) used the wall shear stress to evaluate an apparent shear Modulus G_{app} as well as Young's modulus E_{app} . The advantage of the wall shear stress is that it can be estimated from a numerical solution (confer eq. 5). The Young's modulus can then be estimated from the elongations at different shear stresses as the slope in a stress-strain curve. Aravas and Lapidou (2008) showed in a mathematical study that the wall shear stress is not the optimal description of stress and might underestimate the actual forces stretching the biofilm depending on the geometry of the biofilm. Therefore, in this thesis the estimation of shear stress (eq. 5) was used in section 3.2 to introduce the methods and later replaced by shear stresses accessed from fluid-structure interaction simulation (section 3.3 and 3.4). The third modulus describing ideal elastic deformation is the bulk modulus K . It relates the volumetric change dV to an isotropic pressure change dp . The Bulk modulus is defined as:

$$K = -V \frac{dp}{dV} \quad (14)$$

It is a resistance towards volumetric compression of the elastic material. However, all moduli evaluated in this study describe a real, non-ideal system. Therefore, the evaluated moduli are considered 'apparent' moduli, describing the heterogeneous structures. Details are discussed in the results and discussion part. For biofilm deformation the relation between shear, Young's modulus and the Poisson's ratio is the most important one:

$$\nu = \frac{E}{2G} - 1 \quad (15)$$

Poisson's ratio is the ratio of transverse strain to the longitudinal strain and describes the deformation field within the biofilm matrix (explained in detail in section 3.3.7).

2.6 Fluid-structure interaction model

Biofilm models are widely used to predict growth (Noguera *et al.*, 1999, Picioreanu *et al.*, 2004, Alpkvist and Klapper, 2007b), transport of substrates in biofilms (De Beer and Stoodley, 1995, Stewart, 2003), as well as to simulate fluid-structure interaction (FSI) (Alpkvist and Klapper, 2007a, Böhl *et al.*, 2009). The new concept of this thesis was to implement the real undeformed and deformed geometries as structural templates in the FSI simulations. In addition to the evaluation of material properties from deformation experiments using OCT, FSI simulations were used to get a better estimation of the stress acting on the bulk-biofilm boundary. This improves the calculations of the material properties, which are estimated from the stresses acting on the bulk-biofilm interface. In addition, a new concept to access material properties directly from the simulations is introduced. This provides a new way of measuring material properties non-invasively of biofilms. During the deformation processes, the biofilm structure experiences forces resulting from the interaction with the moving liquid onto the bulk-biofilm interface. At the same time, inner cohesive forces prevent the biofilm from breaking apart and giving rise to internal stresses. Other processes which may create internal forces (such as bacteria growth, motility, production, and re-arrangement of EPS as well as aging of the biofilm matrix) were neglected in the simulation. This assumption was made due to the short time of seconds to minutes in which the elastic biofilm deformation was investigated.

2.6.1 Model domain

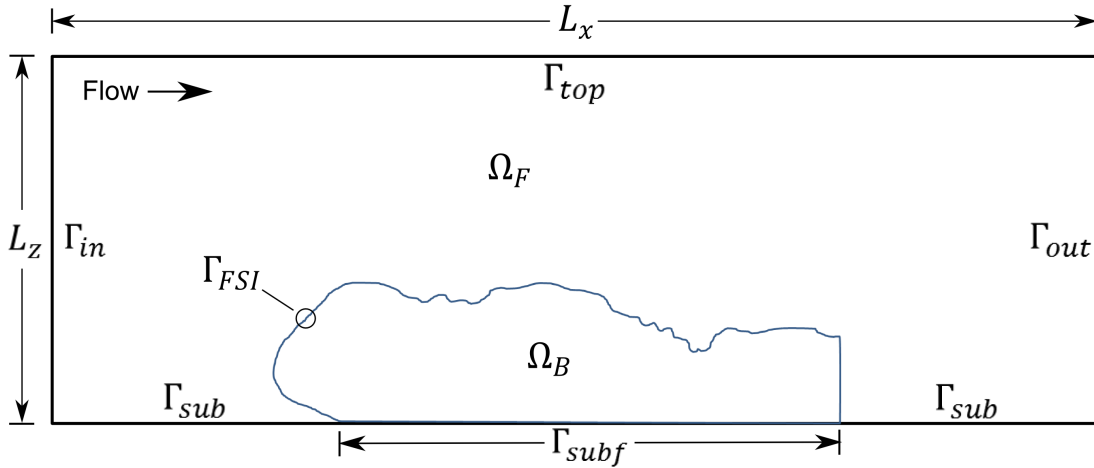


Figure 7: Model domains and boundary conditions. Ω_F : water domain in which the fluid dynamics were computed; Ω_B : biofilm domain in which the solid mechanics were calculated. Γ_{FSI} : fluid-structure interaction boundary with continuity for velocity and stresses; Γ_{in} , Γ_{out} : water inlet and outlet with periodic flow driven by an applied pressure difference; Γ_{top} , Γ_{sub} : no slip (zero flow velocity); Γ_{subf} : fixed solid structure (zero displacement). L_x and L_z are the length and height of the box in which fluid and solid mechanics were calculated. Flow was from left to right.

The two-dimensional biofilm geometry shown in Fig. 7 (domain Ω_B) was extracted from an OCT cross-section and formed the basis for the fluid and solid mechanics calculations. The biofilm domain was placed in a rectangular box representing an OCT cross-section of the flow cell along the flow. The rectangle had a length L_x along the main flow direction and a height L_z perpendicular to the main flow and to the substratum on which the biofilm formed. The difference between the outer rectangle and the biofilm domain represents the fluid domain Ω_F .

2.6.2 Model domain equations

Fluid-structure interaction was modeled by coupling the stationary incompressible laminar Navier-Stokes equation of momentum conservation and the continuity of water flow in Ω_F (eq. 16 and 17):

$$\nabla \sigma_F = \rho(\mathbf{u}_F \cdot \nabla)\mathbf{u}_F \quad (16)$$

$$\nabla \mathbf{u}_F = 0 \quad (17)$$

with the poroelastic structural mechanics (eq. 18 and 19) in the biofilm domain Ω_B :

$$\nabla \sigma_B = 0 \quad (18)$$

$$\nabla \mathbf{u}_B = 0 \quad (19)$$

The liquid produces pressure and viscous forces, included in the stress tensor σ_F :

$$\sigma_F = -p_F \mathbf{I} + \mu(\nabla \mathbf{u}_F + (\nabla \mathbf{u}_F)^T) \quad (20)$$

The the viscous force is known as the shear stress τ of the fluid. The variables solved for are the flow field velocity vector \mathbf{u}_F and the liquid pressure p_F . In the model water density ρ and dynamic viscosity μ were assumed to be constant at 20 °C. Biofilms, which are considered viscoelastic materials, display elastic deformation in short stress exposure and viscous flow behavior during long stress exposure (Klapper *et al.*, 2002, Shaw *et al.*, 2004, Stoodley *et al.*, 2002). In the experiments the biofilm deformation occurred within seconds or minutes, which is shorter than the expected transition time from elastic to viscoelastic deformation of 18 min (Shaw *et al.*, 2004). Therefore, viscous flow (creep) of the biofilm material was neglected. To simplify the complex situation, the biofilm was assumed to behave as a homogeneous isotropic elastic material. The stress tensor σ_F of the liquid produces a stress within the biofilm matrix given by the cauchy stress tensor σ_B for the 2D simulations:

$$\sigma_B = \begin{bmatrix} \sigma_x & \tau_{xz} \\ \tau_{zx} & \sigma_z \end{bmatrix} \quad (21)$$

The shear stress is symmetric, which demands $\tau_{xz} = \tau_{zx}$. Therefore, the stress tensor can be written in vector form:

$$\sigma_B = \begin{bmatrix} \sigma_x \\ \sigma_z \\ \tau_{xz} \end{bmatrix} \quad (22)$$

However, the porous nature of the biofilm cannot be overlooked for a correct representation of the fluid pressure within the biofilm matrix, which has to balance the pressure in the water domain. The Biot-Willis coefficient α regulates the pore pressure in relation to the volume change due to water uptake or release from the pores. The Biot-Willis coefficient ranges between 0 – 1, with $\alpha = 1$ indicating that water can be released upon deformation. The stress tensor σ_B in the biofilm included a poroelastic, as well as a linear elastic component:

$$\sigma_B = -\alpha_B p_B \mathbf{I} + \frac{1}{2} \mathbf{C} : (\nabla \mathbf{v}_B + (\nabla \mathbf{v}_B)^T) \quad (23)$$

Here the variables solved for are the displacement field \mathbf{v}_B and the fluid pore pressure inside the biofilm p_B . A constant Biot-Willis coefficient $\alpha_B = 1$ was assumed and \mathbf{C} represents the elasticity tensor (Coussy, 2003). In all equations \mathbf{I} is the identity matrix and ∇ is either the gradient or divergence operator. The ':' stands for the double-dot tensor product (or double contraction). 2D simulations were performed under plane strain condition, assuming a negligible small deformation out of the 2D plane (y - axis). This includes the assumption of $\varepsilon_y = \gamma_{xy} = \gamma_{yz} = 0$ and $\tau_{xy} = \tau_{yz} = 0$. Therefore, the strain vector is reduced to:

$$\varepsilon = \begin{bmatrix} \varepsilon_x \\ \varepsilon_z \\ \gamma_{xz} \end{bmatrix} \quad (24)$$

The elasticity tensor C relates the strain ε to the Cauchy stress tensor σ :

$$\sigma = C : \varepsilon \quad (25)$$

For the 2D simulations the elasticity tensor C for a linear isotropic elastic material was expressed as a function of the Young's modulus E and Poisson's ratio ν .

$$\mathbf{C} = \frac{E}{(1 + \nu)(1 - 2\nu)} \begin{bmatrix} 1 - \nu & \nu & 0 \\ \nu & 1 - \nu & 0 \\ 0 & 0 & \frac{1-2\nu}{2} \end{bmatrix} \quad (26)$$

The deformation field, which is calculated from this equation via strain, is directly influenced by the Young's modulus. The Young's modulus can therefore be used as sensitive parameter in fluid-structure interaction simulations to fit the simulated deformation to a real deformed geometry. The Poisson's ratio regulates thereby the lateral to the horizontal deformation. In 2D the internal stress of the biofilm structure during deformation

is expressed as the von Mises stress σ_v :

$$\sigma_v = \sqrt{\sigma_x^2 + \sigma_x\sigma_z + \sigma_z^2 + 3\tau_{xz}^2} \quad (27)$$

With the normal stresses $\sigma_{x,z}$ along x and z, and τ_{xz} representing the shear stress, both from the Cauchy stress tensor. The von Mises stress reduces the local stress in all directions to one scalar value. This makes it easier to compare the local stress to a failure criteria for which the material breaks. Additionally, the Biot-Willis coefficient α_B in eq. 23 relates the volume change of fluid absorbed into or released from the biofilm to the volumetric change of the porous matrix. For soft porous materials $\alpha_B \approx 1$. Furthermore, Darcy's equation (eq. 28) couples the gradient of pore liquid pressure p_B from the deformation of the porous structure with the liquid velocity \mathbf{u}_B through the biofilm having the permeability κ_B (Coussy, 2003).

$$\mathbf{u}_B = -\frac{\kappa_B}{\mu} \nabla p_B \quad (28)$$

Here μ is the water viscosity at 20 °C.

2.6.3 Model boundary conditions

The solution of the hydrodynamic equations (eq. 16, 17, and 20) involves the assumption that upstream and downstream of the imaged biofilm structure other similar biofilm patches grew. Therefore, the inlet and outlet flow was treated as periodic (cyclic) boundaries (equal \mathbf{u}_F on Γ_{in} and Γ_{out}). The flow was driven by a pressure difference Δp_F imposed between inlet and outlet. It was calculated from an additional constraint that the experimental measured mean flow velocity u_{mean} was obtained. The flow channel walls were impermeable, therefore no-slip conditions ($\mathbf{u}_F = 0$) were applied on Γ_{top} and Γ_{sub} . For the solution of poroelastic biofilm mechanics (eq. 18, 19, 23, and 28), zero deformation (fixed structure, $\mathbf{v}_B = 0$) was set on the biofilm/substratum boundary Γ_{subf} , together with a no-flow condition ($\mathbf{u}_B = 0$). The liquid and biofilm domains share the fluid-structure interaction boundary Γ_{FSI} . No exchange of liquid was assumed through the biofilm surface, which translates into zero liquid velocity conditions both for the hydrodynamics and for poroelasticity ($\mathbf{u}_F = \mathbf{u}_B = 0$). Finally, continuity of total stress ($\sigma_B = \sigma_F$) was implemented on the FSI boundary as a load force exerted by the flow of liquid on the biofilm surface. To improve the estimation of the mechanical properties, the shear stress can be evaluated as average over the FSI boundary:

$$\tau = \gamma_{SR} \cdot \mu \quad (29)$$

Here, γ_{SR} is the shear strain and μ the dynamic viscosity of water.

2.6.4 Model solutions

All model equations were implemented and solved in COMSOL (COMSOL Multiphysics v. 5.2, COMSOL AB, Stockholm, Sweden) by a finite element method. All variables and parameters are listed in Table 5 (page 27). Meshing in 2D was performed with a triangular mesh with element sizes between 1 to 25 μm .

2.6.5 Evaluation of the Young's modulus from the simulation

To match the simulated deformation to the real biofilm deformation recorded with OCT, the Young's modulus was left free as sensitive parameter. A parametric sweep was performed between $E = 50 - 500 Pa$ to find the best overlap of the simulated and real deformed geometry. The deformation field was exported and overlapped with the OCT data-set in Fiji. Image subtraction highlighted areas where the simulation deformed further as the real geometry as well as areas not covered by the simulation. The combined areas were compared to the area of the real deformed geometry. The Young's modulus was chosen so that the difference was minimized between the simulation and the real deformation.

Table 5: Model variables and parameters

Name	Description	Value	Units	Source
\mathbf{u}_F	Fluid velocity field	State variable	$m \cdot s^{-1}$	-
p_F	Fluid pressure field	State variable	Pa	-
\mathbf{u}_B	Biofilm pore water velocity field	State variable	$m \cdot s^{-1}$	-
p_B	Biofilm pore water pressure field	State variable	Pa	-
\mathbf{v}_B	Biofilm displacement field	State variable	m	-
σ_F	Cauchy stress tensor in fluid	Auxiliary variable	Pa	-
σ_B	Cauchy stress tensor in biofilm	Auxiliary variable	Pa	-
u_{mean}	Average flow velocity	0 to 0.7	$m \cdot s^{-1}$	Experimental data
ρ	Water density outside and within biofilm pores	1000	$kg \cdot m^{-3}$	Value at 20 °C
μ	Water dynamic viscosity outside and within biofilm pores	0.001	$Pa \cdot s$	Value at 20 °C
κ_B	Biofilm permeability	10^{-14}	m^{-1}	Dreszer <i>et al.</i> (2013)
α_B	Biofilm Biot-Willis coefficient	1	-	Assumed
\mathbf{C}	Biofilm elasticity tensor	Matrix	-	Function of E and ν
ν	Biofilm Poisson's ratio	0.4 / -0.33	-	Assumed / experimental data
E	Biofilm Young's modulus	70 to 520	Pa	Fitted

3 Results and discussion

The stability of a biofilm is an interplay of structure and composition of the biofilm matrix. The responsible factors to give the biofilm matrix its mechanical strength to withstand high shear stress, while being able to adapt to new environmental stresses, are not yet well known. Biofilms, which consist of bacteria and hydrated molecules, form a stable and complex hydrogel network. This network does not behave purely elastic nor purely viscous under applied stress. Specialized techniques, such as rotating disc rheometry, dynamic fluid gauging, or shearing techniques were applied in order to understand the mechanical nature of biofilms. Guélon *et al.* (2011) as well as Böhl *et al.* (2013) summarized these techniques in detail. Early work in biofilm mechanics showed that biofilms behave as viscoelastic materials (Klapper *et al.*, 2002, Stoodley *et al.*, 1999c, 2002). Therefore, most studies focused on the viscoelastic behavior of biofilms, but neglected the elastic nature of biofilms. Studies from Körstgens *et al.* (2001a,b) or Mathias and Stoodley (2009) reported an elastic deformation behavior of biofilms when they were subjected to low shear stresses over a short time. From the experiments conducted it is evident that the EPS network must be responsible for the viscoelastic nature of biofilms. However, a detailed overview, which EPS component might be responsible for the elastic or viscoelastic behavior, is missing. The substances in question are polysaccharides and polypeptides. The following section reviews the possible influences both substances have on the biofilm matrix and elucidates the choice for the substrates tested in section 3.3.

3.1 Structural integrity of biofilms

The main components of the EPS, which may give the biofilm its stability, are polysaccharides and polypeptides. Both are known to possess elastic properties when the molecules arrange a stable network of cross-linking chains, and viscoelastic properties when present as hydrogels. Biofilms are known to be highly hydrated, which makes these two classes highly probable to be the dominant factor in the mechanical stability. Polysaccharides, such as hyaluronic acid, can bind up to 1 kg water per 1 g polysaccharide. This is partially due to the hydrophylic groups. The stability of the matrix often relies on the form of aggregated polysaccharides as helices. In some rigid polysaccharides the backbone is composed of 1,4- β - or 1,3- β - linkages, as it is known for the cellulosic backbone of xanthan from *Xanthomonas campestris* (Sutherland, 2001b). Other linkages in polysaccharides produce more flexible structures. These 1,2- α - or 1,6- α - linkages can be found in many dextrans. Battin *et al.* (2003) investigated the (exo-)polysaccharide composition in biofilms. Separation of the polysaccharides via high performance liquid chromatography (HPLC) revealed that glucose is the dominant monomer, followed by mannose, rhamnose, galactose, or xylose. Non-invasive lectinbinding assays, visualized with confocal laser scanning microscopy, support the

frequent occurrence of these monomers and further provided specific insight into the spatial heterogeneity of the biofilm matrix. Their results were the first to show a relative shift of the monosaccharide composition during biofilm development. They found a dependence of the exopolysaccharide/cell ratios in biofilms cultivated under different Reynolds numbers ($Re = 1870$ and $Re = 7560$). At higher Reynolds numbers, the amount of exo-polysaccharides increased while the amount of cells decreased. Therefore, the ratio changed from $3 \text{ fg glucose} \cdot \text{cell}^{-1}$ to $9 \text{ fg glucose} \cdot \text{cell}^{-1}$. Elevated exo-polysaccharide/cell ratios are a stress response and should improve adhesion under high shear stress. This is a functional response to avoid detachment through erosion or sloughing. Many of these polysaccharides are quite soluble, therefore the stability comes from cations binding to the carboxylic groups. Several studies showed that exposure of Ca^{2+} ions to biofilms increase the biofilm stability (Safari *et al.*, 2014, Sutherland, 2001b, Lembre *et al.*, 2012, Körstgens *et al.*, 2001a). The binding of divalent ions is often associated with specific polysaccharide chain coupling and hints that the carbohydrates in the biofilm matrix are a major reason for structural integrity. Sutherland (2001b) compared bacterial and algal alginates, which give a clear indication of the relationship of polysaccharide structure and function. The algal polysaccharides formed rigid, non-deformable gels due to the highly specific interaction with either Ca^{2+} or Sr^{2+} . This is not seen in bacterial alginates from *Azotobacter vinelandii*, even though the EPS closely resemble the algal one (Ertesvåg and Valla, 1998). The bacterial polysaccharides are often acetylated, which prevent interaction between polymer chains and cations, resulting in gel formation. However, some binding of cations does occur, and there is also some specificity towards Ca^{2+} .

The other main component of the EPS are polypeptides. Amino acids form hydrogels too, which behave as viscoelastic material (Roy and Banerjee, 2011). Phenylalanine, which has been used as substrate in this study, has been shown to effectively produce hydrogels as short peptides (Smith *et al.*, 2008, Jayawarna *et al.*, 2007). Panda *et al.* (2008) investigated the structural behavior of low molecular weight peptide hydrogels. Peptides, especially dipeptides, form stable hydrogels with properties relevant for the mechanical stability of biofilms. They found that the structure of the gel, investigated using tunnel electron microscopy, showed a dense network of fibers. Each fiber was $15 - 20 \text{ nm}$ in diameter and had a length of several micrometers. This network has a high surface to volume ratio to bind water efficiently. It is generally believed that these dense fiber networks, with junction points, give the hydrogel matrix high mechanical strength and solvent retention properties (Weiss and Terech, 2006). The hydrogel is further responsive to temperature, pH, and salt changes. The gel can entrap and release bioactive molecules through pH and salt concentration changes. This is an important functionality for the biofilm matrix. Especially diffusion as well as entrapment of bioactive molecules is crucial as regulation mechanism. Roy *et al.* (2013) looked at possible application of these biomaterials and mentioned that most of the low molecular weight

hydrogels are highly sensitive towards mechanical stress or strain. Typically, these hydrogels irreversibly release water molecules, which were bound in their self-assembled network system, if shear stress is applied to them. These gels behave as a solid suspension that loses its original elastic properties after the stress is removed. This causes viscoplastic deformation due to the rearrangement of the network. Hollenbeck *et al.* (2016) were able to show that viscoplastic deformation does occur in biofilms for large elongations. However, the gels can break up into a viscous solution under an externally applied mechanical stress and regain their previous elastic properties, when the stress is released. This is only valid for pure hydrogels, but describes very well which role the proteins play in the biofilm matrix.

Mayer *et al.* (1999) investigated the contribution of polysaccharides and proteins on the stability of biofilms. They used a variety of spectroscopic techniques, such as nuclear magnetic resonance spectroscopy (NMR) or fourier transform infrared spectroscopy (FTIR). These techniques are capable to detect functional groups, such as the hydrogen-bonds with carboxylic groups, which hold the biofilm structure together. Their model EPS system was *P. aeruginosa*. The EPS was mainly composed of two macromolecular components: polysaccharides (mostly containing uronic acid) and polypeptides. The most important functional groups were identified as carboxyl (or possibly carboxylate and amide) groups, hydroxyl groups and acetal groups. A number of molecular interactions are possible with these residues. The mechanisms involved in the cross-linking within the biofilm matrix are mainly:

- electrostatic forces between various ionic or non-ionic functional groups
- hydrogen bonds
- dispersion interactions such as van-der-Waals forces

Considering the strength of the potential interactions, carboxylate groups and hydroxyl groups are expected to play the most important roles among the functional groups present in EPS. Both polysaccharides as well as polypeptides seem to possess the ability to give the biofilm structure its stability. As Mayer *et al.* (1999) proved, the stability is probably more a combination of well interacting functional group rather than single portions of the EPS.

To test the influence of sugars and proteins on the mechanical stability, biofilms were cultivated with three different substrates: acetate, glucose and phenylalanine. Each substrate contributes differently to the composition of the EPS matrix.

Chapter 3.2 builds the basis for the investigation of material properties with optical coherence tomography. It is shown how the shear modulus (rigidity), as well as the Young's modulus (elasticity) can be estimated from the deformation experiments. Based on these experiments the influence of the substrate and the Reynolds number during cultivation on the mechanical stability of biofilms is investigated in chapter 3.3. This helped to gain a deeper understanding of the mechanical nature of biofilms.

3.2 Accessing the mechanical properties of biofilms

3.2.1 Elastic biofilm deformation

Körstgens *et al.* (2001a,b) and Mathias and Stoodley (2009) reported an elastic deformation behavior of biofilms when they were subjected to low shear stresses over a short time of seconds to minutes. However, up to now no experimental study investigated the elastic deformation of biofilms in detail. For the first time it was possible to visualize dynamic processes, such as change of the macro-porosity during deformation or measure the time a biofilm needs to adapt to a change of shear stress, using optical coherence tomography. The fast processes responsible for elastic deformation occur in the first few seconds after a stress is applied onto the biofilm.

Shear stress applied over a short period of time

To visualize elastic biofilm deformation, series of 2D OCT cross-sections were acquired in dynamic shear stress experiments at different Reynolds numbers. Shear stresses ranging from $\tau = 0.01 - 1.64 \text{ Pa}$ were applied for 10 s and the corresponding deformation was recorded. Fig. 8 shows the deformation for different shear stresses of biofilm **I** (cultivated with glucose, see Table 4). Setting the shear stress to $\tau = 0.01 \text{ Pa}$ ($Re = 4$) resulted in no detectable compression or deformation compared to no flow conditions (within the resolution of the OCT). The resistance to deform at low shear stresses imply a general existence of a shear strength, which means that the material will start to deform only at shear stresses higher than this value. Consecutive testing of higher shear stresses $\tau = 0.3, 0.6,$ and 0.8 Pa ($Re = 91, 172,$ and $250,$ respectively) showed a deformation/compression of the biofilm along the direction of flow. The white line in Fig. 8 represents the maximum compression the biofilm could withstand before it detached at $\tau = 1.1 \text{ Pa}$.

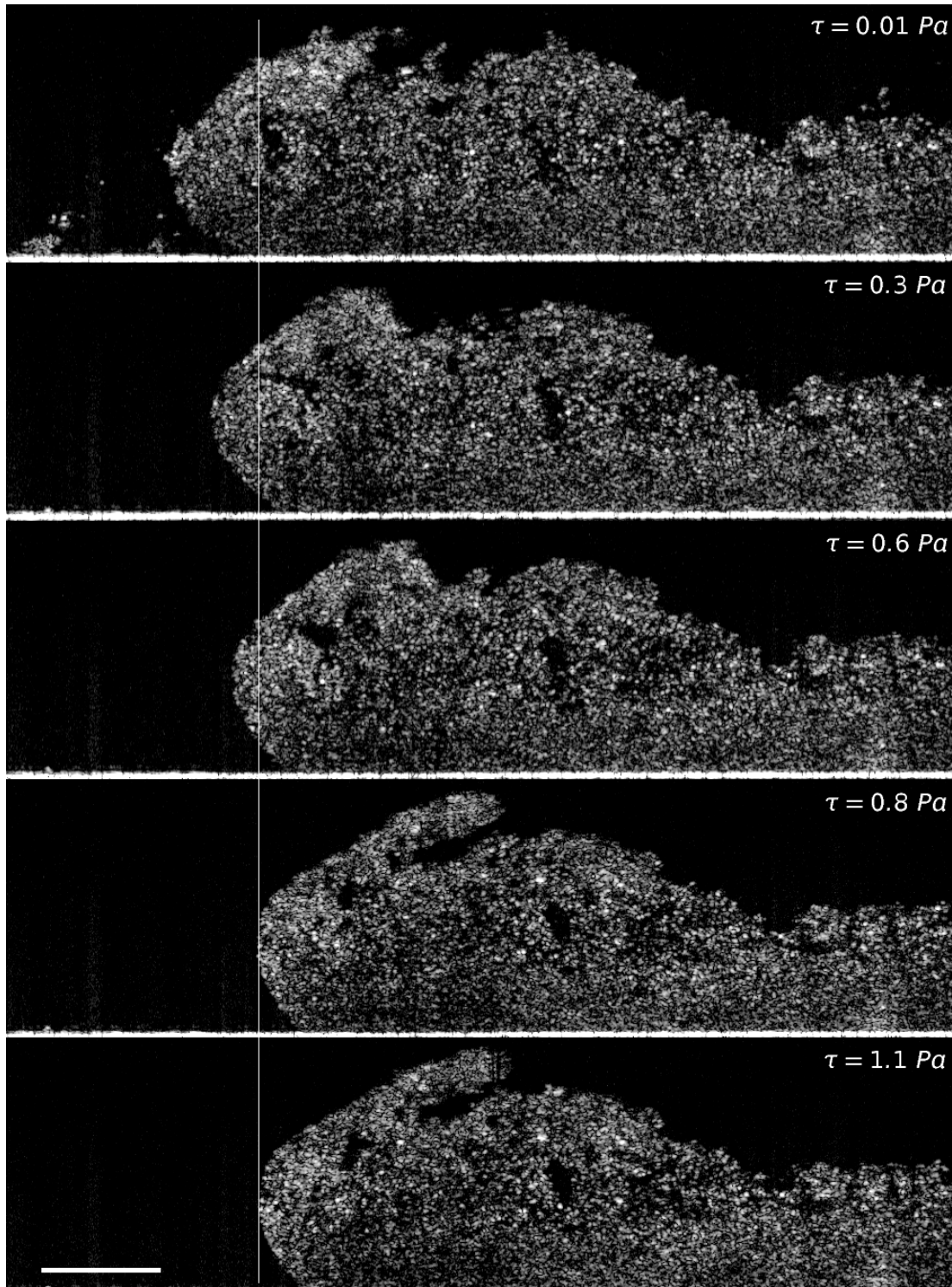


Figure 8: Maximum displacement at different shear stresses for biofilm **I**, cultivated with glucose. The white line represents the maximum deformation at $\tau = 1.1 Pa$ the biofilm could withstand during the shear stress experiments. At $\tau = 0.8 Pa$ the maximum deformation was already achieved. The biofilm detached at $\tau = 1.1 Pa$, after the adaption phase of the biofilm (after $\sim 2 s$ of flow). Flow from left to right. Scale bar equals $250 \mu m$.

The experiments showed that it took approximately 2 s for the biofilm at all shear stresses to adapt to the new conditions by deformation. In Fig. 9 the deformation of biofilm **I** is shown exemplary for $\tau = 0.6 Pa$ (A video is available online from Blauert *et al.* (2015)). The image sequence shows the biofilm structure before the flow starts (0 s), as well as 2 and 10 s after flow started, respectively. The white line represents the undeformed biofilm at 0 s. The upstream part of the biofilm, where the highest

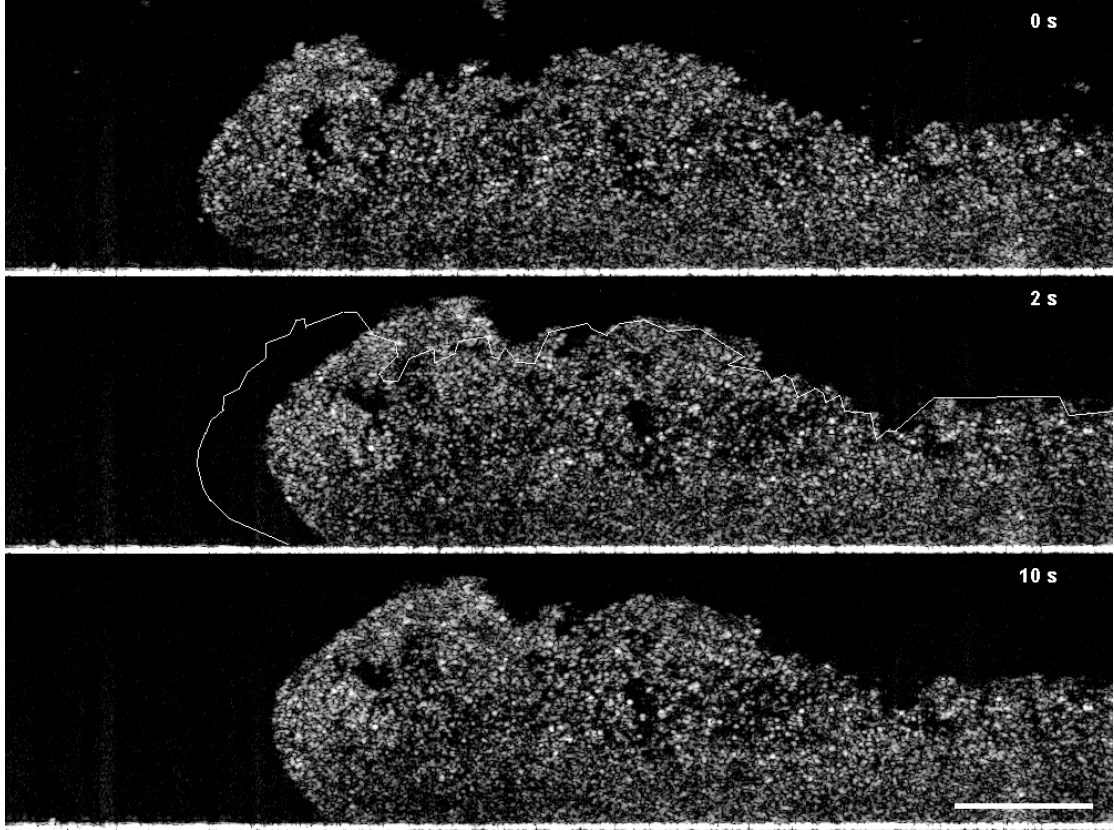


Figure 9: Biofilm **I** in a shear stress experiment over 10 s. Full deformation was achieved after 2 s of flow and the deformation remained until the flow was stopped. The white line represents the undeformed biofilm at 0 s. Scale bar equals $250 \mu m$. Flow from left to right.

shear occurred, deformed the most. The biofilm macro-porosity decreased during the experiment by $\Delta\Phi = 2\%$ to a value of $\Phi = 45\%$ and fully recovered to $\Phi = 47\%$, when the shear stress was reduced to $\tau = 0 Pa$. This is the first time the change in macro-porosity was observed during deformation of the biofilm structure. OCT makes it possible to look into the biofilm structure non-invasively and use the acquired images in data processing to calculate structural changes. The biofilm compressed $148 \mu m$ along the flow within the 2 s of adaption time. Until the flow was stopped no further compression or change was detected. This compression behavior of the biofilm occurred for the other deformations at $\tau = 0.3, 0.8$ and $1.1 Pa$, too. Thereby, it was validated that the maximum deformation occurs within the first seconds after increasing the shear

stress.

He *et al.* (2013) showed that according to the Maxwell model the viscoelastic behavior of biofilms can be described by three stress relaxation processes; each with a characteristic time constant. The fastest process corresponds to water extrusion and occurs within the first few seconds during externally applied load. The other two relaxation processes are related to the rearrangement of biofilm constituents (e.g. EPS) occurring between 5 and 100 s after the load was created. The rearrangement of bacteria within the deformed biofilm occurs, when the load is applied for more than 100 s. This coincides well with the initial deformation behavior found in the shear stress experiments at different shear stress levels. Within 2 s, the biofilm either compressed/deformed or detached. The whole biofilm adapted quickly to the applied stress, while the largest compression was measured in the upstream part of the biofilm structure. After the adaption phase, no changes in the position of the biomass or voids was detected until the flow were stopped. The behavior seems to be plausible as the upstream part of the biofilm faces the highest forces (shown by CFD simulation in section 3.4). Especially biofilm clusters with mean biofilm thicknesses $> 200 \mu m$ show this deformation at the front, while smaller biofilm structures deform completely. For the 10 s of applied shear stress, no creep was expected and the biofilm returned to its initial shape. For the highest applied shear stress $\tau = 1.1 Pa$, the biofilm detached within $\Delta t = 250 ms$ shortly after the adaption phase. The detachment happened within the time resolution the OCT measurement. It could be shown that the biofilm first adapted to the new shear stress prior to detachment. However, the strength of OCT to reveal non-invasively dynamics within the biofilm allowed to provide a more detailed insight into the deformation process within the first 2 s.

To study the biofilm deformation within the 2 s in more detail, a shear stress experiment was conducted at $\tau = 1.64 \text{ Pa}$. The deformation process of biofilm **II** (cultivated with glucose, see Table 4) was analyzed cross-section by cross-section within the first 2.1 s after the flow was started. During the deformation 21 OCT cross-sections were acquired at 10 frames/s. The series of cross-sections is illustrated in Fig. 10. Comparing the first and last image at 2100 ms (the white line represents the undeformed structure at 0 ms) indicates the necessity to differentiate the observed biofilm structure into two parts. The upstream and downstream part of the biofilm showed a different deformation process. The main deformation was located in the upstream part, while little compression was detected for the downstream region.

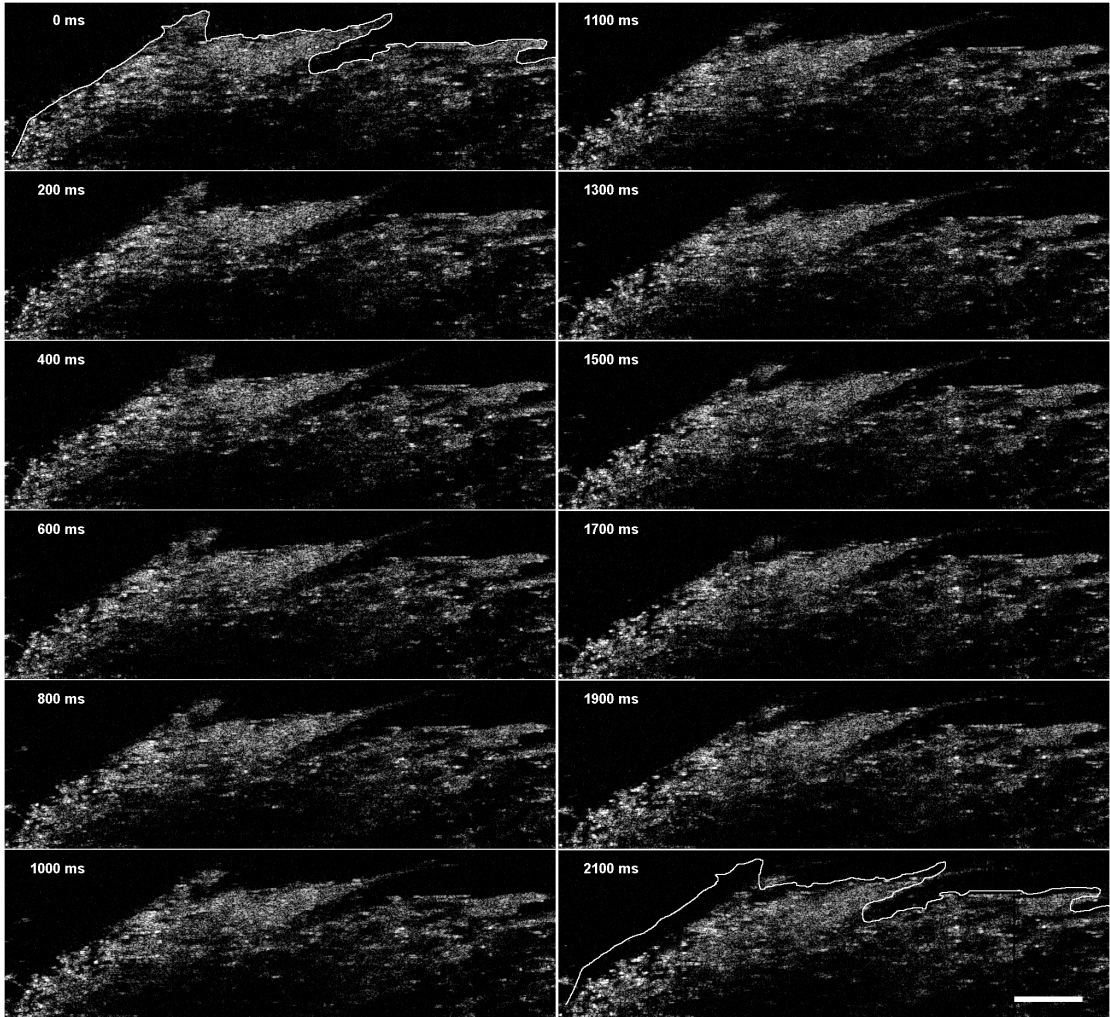


Figure 10: Detailed deformation process of biofilm **II** within the first 2 s after the flow started. The montage shows every second cross-section recorded. The white line at 2100 ms represent the outline of the undeformed biofilm at 0 s. Scale bar equals $250 \mu\text{m}$. Flow from left to right. Taken from Blauert *et al.* (2015).

The development of the mean biofilm thickness is presented in Fig. 11 **A**. Within 400 ms the mean biofilm thickness decreased from $\bar{L}_F = 420 \mu\text{m}$ to $\bar{L}_F = 408 \mu\text{m}$ (cross-

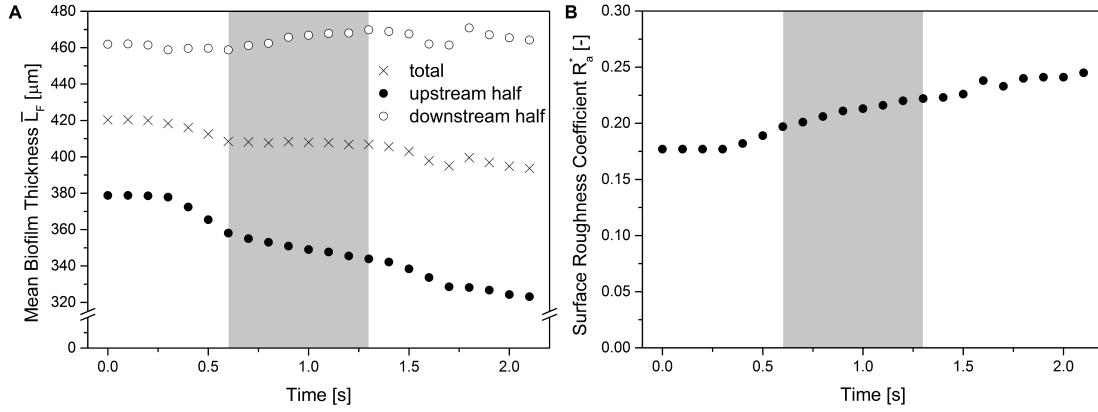


Figure 11: **A** Change of mean biofilm thickness \bar{L}_F and **B** the surface roughness coefficient R_a^* during the first 2.1 s of applied shear stress. The steady biofilm thickness during the deformation is indicated in grey. Taken from Blauert *et al.* (2015).

sections 200 – 600 ms in Fig. 10). The mean biofilm thickness (displayed as crosses \times) of the complete biofilm structure decreased after the plateau to $\bar{L}_F = 394 \mu\text{m}$ and the average biofilm thickness reduction/compression was $\Delta\bar{L}_F = 27 \mu\text{m}$; $\approx 6\%$ of the initial mean biofilm thickness. The mean biofilm thickness of the total structure showed a plateau between cross-sections captured at 600 and 1300 ms. This is indicated by the gray area in Fig. 11 **A**. The cause for the plateau region can be understood by dividing the image in an upstream and downstream half and investigating the changes of the mean biofilm thickness separately. The calculated mean biofilm thickness for the upstream (filled circle \bullet) and downstream part (empty circle \circ) of the biofilm structure showed different trends. The upstream part showed a steady decrease of the mean biofilm thickness, while the thickness for the downstream part kept increasing with a fluctuation between 1500 and 1700 ms. The plateau of the total mean biofilm thickness is the result of two effects in the downstream region. First, the elongation of the upper filamentous structure which causes the mean biofilm thickness to rise. Second, the effect of the elastic expansion perpendicular to the flow caused by the compression along the flow. This is known for elastic materials and the Poisson's ratio provides a number for this behavior (explained in detail in chapter 3.3.7). Both effects compensate the thickness decrease of the upstream region, creating the plateau. Due to the shape of the biofilm structure it is expected that the flow bypassed the downstream part of the biofilm structure causing less changes there, as seen in Fig. 10 and 11 **A**. The filamentous structure at the biofilm surface started to elongate shortly after the shear stress was raised until the end of the experiment (see Fig. 10, cross-sections 400 - 2100 ms). During the experiment the filament oscillated perpendicular to the scan axis, which caused intensity variations influencing the mean biofilm thickness (see decrease of \bar{L}_F after 1.5 s for the downstream part in Fig. 11 **A**).

The surface roughness coefficient unexpectedly increased over the experimental du-

ration. The development of the surface roughness coefficient is presented in Fig. 11 **B**. The surface roughness coefficient rose during the deformation from $R_a^* = 0.177$ to 0.245. At the beginning of the plateau in the roughness coefficient curve (Fig. 11 **B**), the slope of the roughness coefficient decreased. Subsequent compression did not influence the slope further. The constant rise of the roughness coefficient during the plateau phase indicated that the biofilm structure was compressed unequally over its length. The deformation of the upstream surface led to a reduced biofilm thickness compared to the downstream part. As a result, the variation of the local biofilm thickness compared to the mean biofilm thickness increased; consequently, the roughness coefficient increased, too. In Fig. 12, the calculation of the biofilm elongation is illustrated. The measured elongation of the filamentous structure was $220 \mu\text{m}$. This change is comparable to whole biofilm structures reported from other mechanical studies, e.g. Klapper *et al.* (2002), or Stoodley *et al.* (1999c). Stoodley *et al.* (1999c) conducted similar flow cell experiments on the microscale with biofilm streamers forming at high shear stress ($\tau = 5.1 \text{ Pa}$). They used light microscopy to determine the angle of deformation and elongation of the structure as well as applied fluorescent particles to calculate strain. The limitations of such experiments are on the one hand the size of the biofilm structure of only a few hundred micrometers. This is due to the restricted field-of-view of microscopes used. On the other hand, the limitation is the visualization of silhouette structures of the biofilm, rather than xz-cross-sections (2D) or volumetric scans (3D), acquired by means of OCT. One way to overcome these restrictions would be to add fluorescent particles, which are embedded into the biofilm structure, and follow their displacement by stereo-microscopy imaging (Hu *et al.*, 2013). This is somehow similar to the impact of nanoparticles used to measure diffusion in biofilms (Peulen and Wilkinson, 2011). Nevertheless, with microscopic techniques, it is still not possible to describe validly the cavity distribution or reveal dynamics inside the biofilm without manipulation of the structure. A limitation of the acquisition of OCT cross-sectional images is the movement of biofilm out of the imaging plane during the imaging process. For example, oscillation of the filamentous part of the biofilm caused the structure to bend/move out of the cross-section. This led to signal depletion especially in measurements under dynamic flow conditions. As a consequence, the OCT lost biomass-related signals, explaining the drop at 1600 ms in the mean biofilm thickness curve. Another consequence was a variation of the surface roughness coefficient. Similar signal depletion can occur due to detachment. OCT is sensitive for particles blocking the light path (Haisch and Niessner, 2007). Biomass flushed through the flow channel scatters the light rather than reflects it, causing the depletion of signal. Scattering can cause problems in time-resolved measurements and might create data variations influencing the quality of calculated structural parameters. To reduce the impact of such imaging artifacts, averaging of A-scans or cross-sections can be acquired with the drawback of prolonged measurement time. Following these structural changes shows the strength of the OCT. Unlike other imaging techniques, the

fast acquisition of cross-sectional images instead of the whole biofilm silhouette allows to extract specific areas of interest. The deformation process analyzed in this section revealed that biofilms do not deform as ideal elastic material. They rather show different deformation processes in the upstream and downstream part. This indicates a heterogeneity in the biofilm structure. To access the mechanical properties cross-sections with a defined upstream edges were chosen.

The mechanical parameter which can be extracted from these deformations is the shear modulus G . The comparison of the biofilm structure with and without fluid flow (shear stress) is presented in Fig. 12. From the cross-sectional images the overall

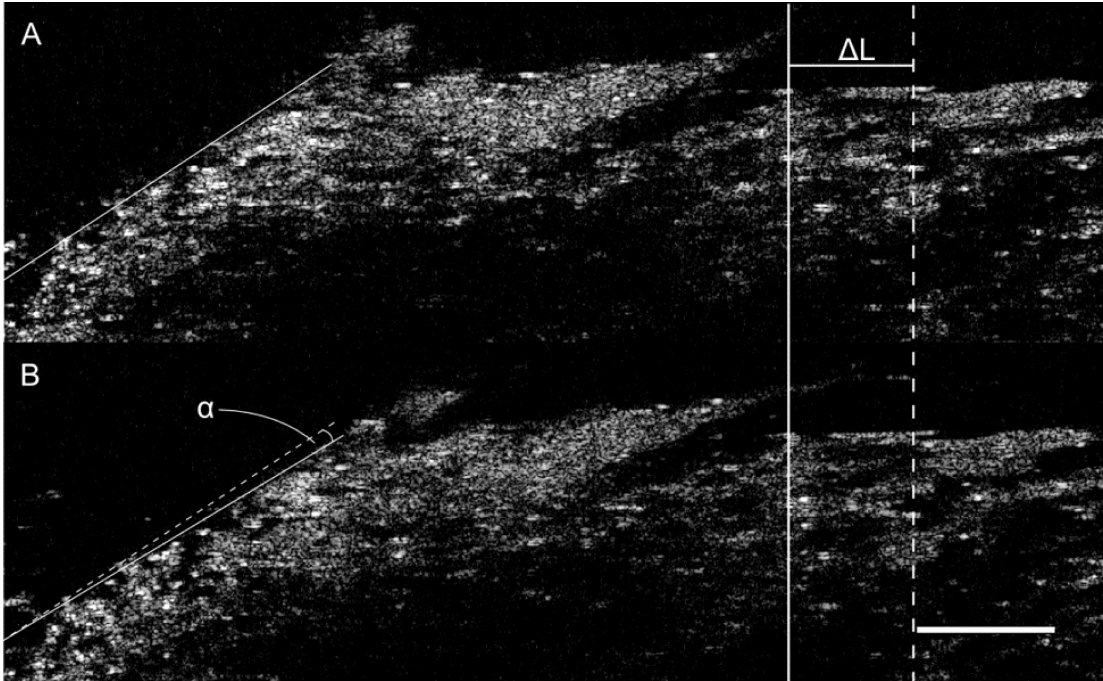


Figure 12: Evaluation of the shear modulus G from the angular change α during the biofilm deformation. **A** shows the biofilm without flow, **B** at full deformation. Scale bar equals $250 \mu m$. Flow from left to right. Taken from Blauert *et al.* (2015).

structure appeared intact and no detachment was detected. For the particular biofilm structure, OCT did not allow to acquire all signals in depth. Especially, signals from deeper regions and the bottom of the biofilm are missing in Fig. 12. These regions appear black and it was not possible to distinguish between cavities/voids and signal depletion. However, this did not influence the evaluation of the shear modulus G . To evaluate the shear modulus, the angle of deformation α was determined from the two lines (solid and dashed) in Fig. 12 **B**. They mark the position of the undeformed ($\tau = 0 Pa$) and deformed biofilm ($\tau = 1.64 Pa$). The measured change in the angle of deformation was $\alpha = 3^\circ$. From this deformation a shear modulus of $G = 31.3 Pa$ was estimated using eq. 5. In the experiments of Stoodley *et al.* (1999c) an effective shear modulus of $G = 27.1 \pm 0.9 Pa$ was estimated.

OCT could in future be used to link and understand differences of mechanical ex-

periments on the micro- and macroscale. Structural mechanics experiments on the macroscale need to be interpreted differently (Ochoa *et al.*, 2007). Unlike experiments on the microscale setups on the macroscale, such as rotating disk rheometers, do not investigate local or individual biofilm structures. They rather investigate a community and therefore an average of the mechanical properties. The OCT deformation experiments already showed that the biofilm does not behave as ideal homogeneous material. It is expected that local heterogeneity exists. Therefore the measure of macroscale experiments need to be interpreted carefully. Towler *et al.* (2003) conducted rotating disk rheometry experiments with multispecies biofilms. In their macroscale experiments, a shear modulus ranging $G = 0.3 - 45 Pa$ was measured. This validates the assumption of heterogeneity within the biofilm structure and between different biofilms. Thereby, a detailed examination of local structures (as presented here) is justified, since the local biofilm characteristics merge in macroscale experiments. Experiments on the macroscale lack information of how the inner structure of the biofilm changes, and further how these changes influence the mechanical stability and mass transfer. Furthermore, OCT was used to measure the macro porosity change during the elastic deformation. For the investigated biofilm **II**, a decrease of the biofilm porosity $\Delta\Phi = 2\%$ was again calculated over the entire experiment, with a biofilm porosity Φ changing from 66% to 64%. All elastic deformation experiments showed the same 2% decrease in the macro porosity. Properties such as porosity as well as biomass and cavity distribution have an influence on structural stability and need to be considered. Large cavities tend to deform first, extruding the water. This was further investigated in time-lapsed measurements and is discussed in the following section.

Testing material properties of biofilms is a challenging task. Several devices destroy the biofilm in the measurement (e.g. rotating disc rheometer) or measure averaged mechanical properties on the macroscale. Even though material properties are important to be investigated, a non-invasive test method is preferred. This allows to potentially test material properties over time. Flow cell experiments using OCT or light microscopy have a clear advantage over other techniques, since imaging is non-invasive and the measurement can be done *in situ*. Using OCT imaging additionally allows to access the whole biofilm structure on the mesoscale. Local material property variations can be revealed (as discussed below) addressing the heterogeneity of the biofilm matrix, which is not considered by measurements on the macroscale. Furthermore, OCT provides the possibility to measure changes of and within the biofilm matrix. This includes changes in the porosity and a more accurate description of thickness and surface roughness compared to light microscopy images, which produce a crude silhouette.

Shear stress applied over a long time

The viscoelastic deformation of biofilms is a time-dependent process. In a study of 44 biofilms Shaw *et al.* (2004) found that the transition time from elastic to viscoelastic deformation is ~ 18 min. Nevertheless, elastic deformation can be found in larger biofilm clusters subjected to shear stress for a longer period of time. Fig. 13 shows the defor-

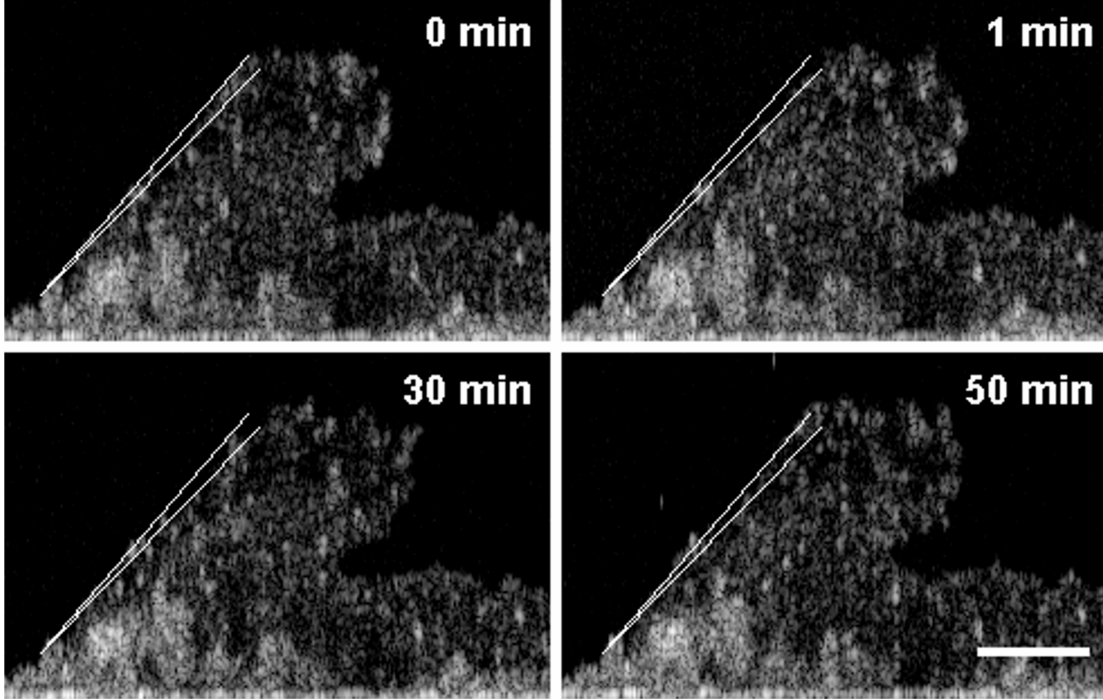


Figure 13: Elastic deformation of biofilm **III** over 30 min constant shear stress. After the flow was stopped, the biofilm showed an elastic recovery. Scale bar equals $250 \mu m$. Flow from left to right. Taken from Blauert *et al.* (2015).

mation and recovery properties of biofilm **III** cultivated with glucose (see Table 4). The location of the cross-section in the flow cell was constant between the images acquired over the 50 min of fluid flow. The shear stress was set to $\tau = 1.64 Pa$ to compare the long time exposure of shear stress to the experiments with 10 s of fluid flow. The biofilm reached a maximal angle of deformation of $\alpha = 3^\circ$. This deformation occurred within the first OCT scan after 1 min and kept the same deformation for 30 min until the applied shear stress was removed. The biofilm in the time-lapsed measurement showed a similar deformation behavior compared to the dynamic deformation experiments described in the previous section. Again, from the deformation over time a shear modulus of $G = 29.7 \pm 1.7 Pa$ ($n = 10$) was estimated, confirming the results of the shear stress experiments. After the flow was stopped, the biofilm showed an elastic response by returning into its original position. Within the resolution of the OCT device no major deviations between 0 and 50 min could be evaluated. The elastic response was not expected for a long shear stress exposure. However, the expected 18 min of transition time can not be valid for all biofilms. Composition and EPS arrangement can differ for all

biofilms. Moreover, biofilms have been shown to withstand several pascal of shear stress before yielding to the applied stress (discussed in detail in section 3.3.5). Indicating that the shear stress might not be enough to trigger viscoelastic deformation.

Another interesting feature of OCT is to identify denser structures at the bottom of biofilm **III**. The intensity of the biofilm signals in the image is proportional to the density of the biofilm matrix. In theory the signals can be converted to a certain biofilm mass density, given that the proportional factor is known. This relation is influenced by the refractive index of the medium (water and biomass), the optical path length, and a signal to noise ratio drop along the optical axis. For a correct interpretation of the signal intensities the signal of the biofilm matrix must be calibrated first. This is not yet possible. However, the intense signals such as in Fig. 13 still indicate denser structures at the bottom of the biofilm matrix. This has been measured experimentally in several studies (Masuda *et al.*, 1991, Zhang and Bishop, 1994, Bishop *et al.*, 1995) and later been predicted in a model approach by Lapidou and Rittmann (2004). OCT data validated again the heterogeneity of the biofilm matrix, which are responsible for locally changing mechanical properties.

3.2.2 Viscoelastic biofilm deformation

As mentioned before, elastic and viscoelastic deformation are time-dependent processes. The transition from elastic to viscoelastic deformation was investigated for several different biofilms by Shaw *et al.* (2004). They found in a study with 44 biofilms that the average time for this transition is ~ 18 min. The processes which play a role are water extrusion within the first few seconds, re-arrangement of biofilm constituents (e.g., EPS) occurring between 5 and 100 s, and rearrangement of bacteria within the deformed biofilm, when the load is applied for more than 100 s (He *et al.*, 2013). This time-dependent process was investigated in stress-strain experiments.

Time-lapsed biofilm deformation

Fig. 14 shows the z-projections of a 3D time-lapsed deformation experiment. The image sequence displays the color-coded biofilm thickness from top onto biofilm **IV** (cultivated with glucose, see Table 4). For better visualization, the area of interest was cut to $1108 \mu\text{m} \times 476 \mu\text{m}$ ($277 \text{ pixel} \times 119 \text{ pixel}$). The duration of the stress-strain experiment was 36 min. Therefore, the time of the maximum applied shear stress coincides with the expected transition time of 18 min from elastic to viscoelastic deformation according to Shaw *et al.* (2004). The load cycle will show mainly elastic deformation while the unload cycle is dominated by viscoelastic effects. The changes of the 3D biofilm structure can be described by the macro-porosity, the mean biofilm thickness, and the surface roughness coefficient. Viscoelastic deformation and calculation of the strain (elongation along the flow direction) were processed from cross-sections. The strain is important for the stress-strain curve from which the apparent Young's modulus was estimated. Fig. 14 shows every second z-projection of the biofilm adapted to the corresponding shear stress τ during the experiment. The first z-projection in the sequence shows the relaxed biofilm structure without applied shear stress. By raising the shear stress to $\tau = 0.43 \text{ Pa}$ the filaments attached to the biofilm and the overall structure became smoother. In Fig. 14 the color indicates the biofilm thickness. The brighter the color the thicker the biofilm. Smoothing of the surface roughness is visualized by harmonizing the colors. Setting the shear stress to $\tau = 1.21 \text{ Pa}$ part of the downstream biofilm detached. Elongation of the biofilm structure is difficult to identify by eye but measurable in image processing. Vertical lines such as in (g) and (j) are imaging artifacts due to fast movement during the image acquisition. During decreasing shear stress the biofilm structure relaxed and the relaxed structure at $\tau = 0 \text{ Pa}$ could be compared to the structure before the experiment at $\tau = 0 \text{ Pa}$ to determine detachment and viscoelastic effects (discussed in detail below).

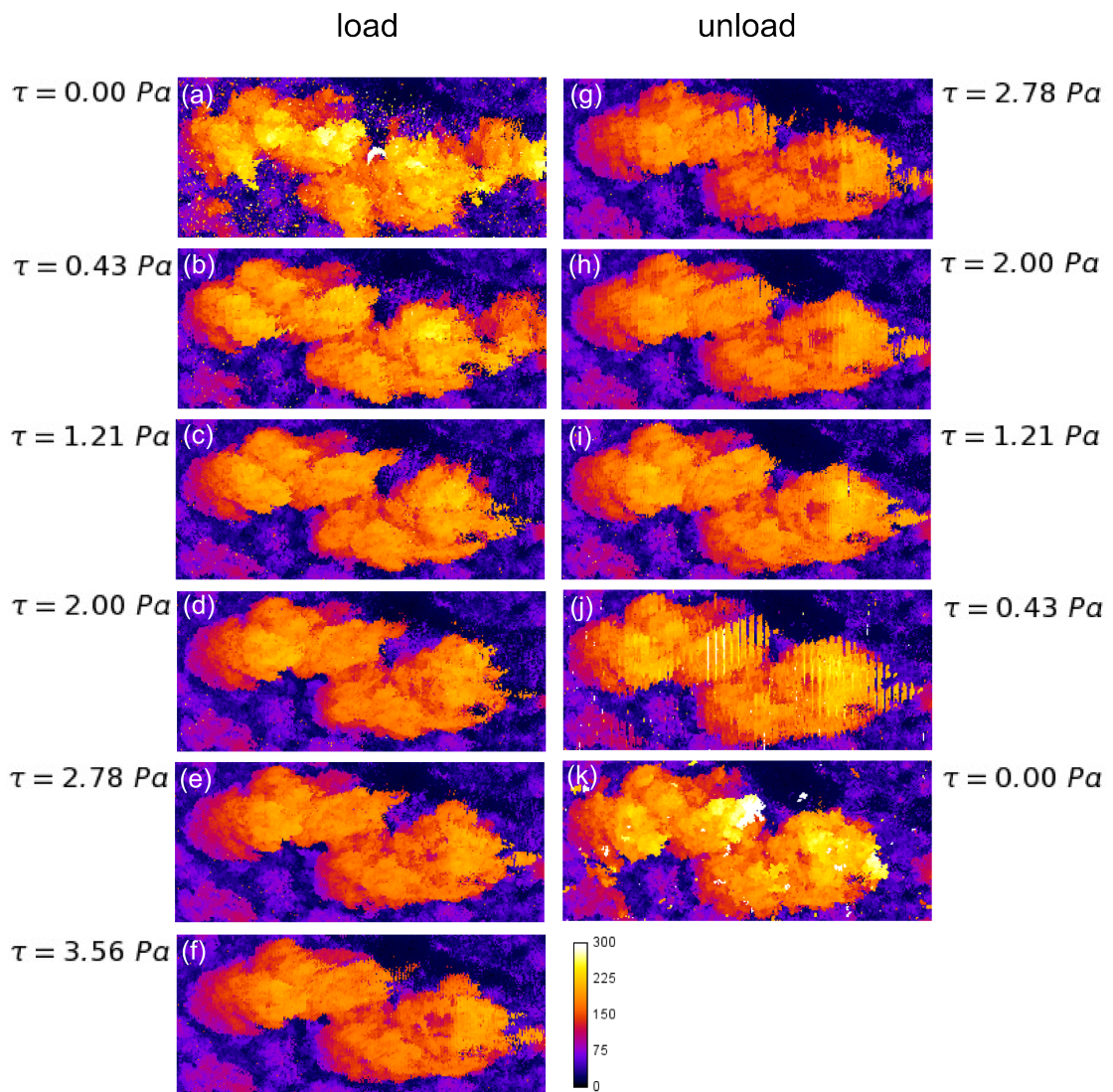


Figure 14: The image sequence shows the z-projections of biofilm **IV** in a stress-strain experiment. Each z-projection is $1108 \mu m \times 476 \mu m$. The shear stress was increased in the load cycle(a)-(f) and decreased in the unload cycle (g)-(k). The color-coded biofilm thickness is expressed in μm (calibration bar). Flow from left to right.

Porosity change

The dynamic changes, discussed in section 3.2, occurred in each of the loading steps. The development of the volumetric macro-porosity is shown in Fig. 15 **A**. It decreased during the load cycle by $\Delta\Phi \approx 8\%$ from $\Phi = 51\%$ to 43% . The linear decrease of the porosity fits with the findings from the elastic deformation. Comparing the macro-porosity change at a shear stress of $\sim 1.6 Pa$ shows that the time-lapsed deformation has a similar macro-porosity decrease of $\Delta\Phi = 3\%$ compared to the 2% of the elastic deformation. This is

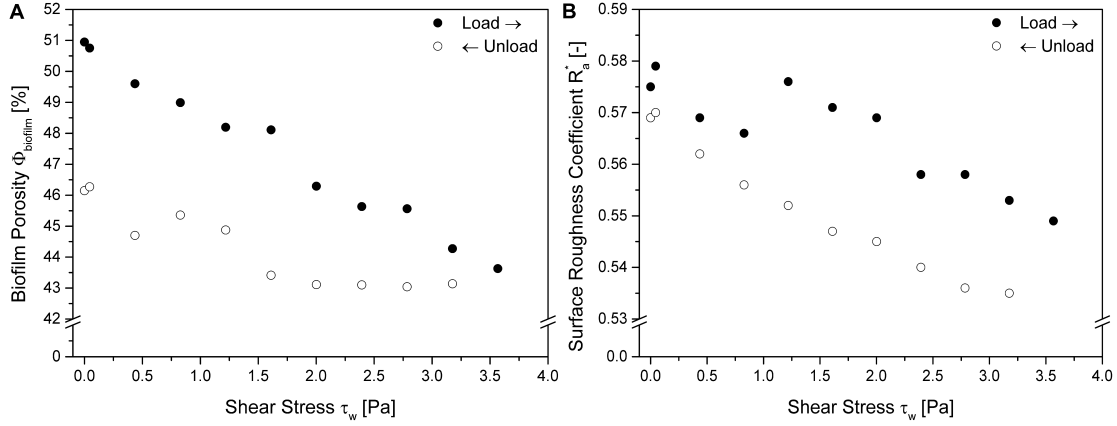


Figure 15: Internal time-lapsed changes of the volumetric biofilm macro-porosity **A** and the surface roughness coefficient **B** during the stress-strain experiments. Taken from Blauert *et al.* (2015).

in agreement with the assumption that the load cycle is dominated by elastic processes. During the unload cycle (at the transition period of 18 min) the macro-porosity dropped slightly by approximately 1% and remained then constant at a level of $\Phi = 43\%$ until a shear stress of $\tau = 1.6 Pa$ was reached. This demonstrates the influence of the viscous property of the biofilm matrix. The biofilm structure did not regain linearly its initial porosity, as it would be expected from a purely elastic material. A further decrease of the shear stress ($\tau = 1.6 \rightarrow 1.2 Pa$) increased the biofilm macro-porosity to $\Phi = 46\%$. The recovery of porosity during the decreasing shear stress supports that the biofilm did not regain its original conformation. In consequence, the adaption to further changing shear stress conditions is influenced or restricted. While the biofilm macro-porosity during elastic deformations changed by $\Delta\Phi = 2\%$ (at $\tau = 1.64 Pa$), viscoelastic deformation showed a higher change of $\Delta\Phi = 8\%$ (at $\tau = 3.56 Pa$). A lower porosity indicates a higher biomass and bacteria density. This does not only influence the biofilm structure, but will also influence the diffusive transport of nutrients within the biofilm matrix. In several studies the effect of changing diffusion coefficients in biofilms, cultivated at different cultivation velocities, were demonstrated (Beyenal and Lewandowski, 2002, Brito and Melo, 1999). Brito and Melo (1999) showed with flow cell experiments that an increase of the mass transfer coefficients by up to 20% is possible. This is in agreement with a dynamic 2D modeling approach introduced by Taherzadeh

et al. (2012), who showed how mass transfer is influenced by moving biofilm streamers; similar to the biofilm structures presented. Taherzadeh *et al.* calculated an increase in substrate uptake for the whole biofilm streamer of up to 20% and even higher at the end of the oscillating streamer tip.

Surface roughness coefficient change

During the stress-strain experiment the surface roughness coefficient R_a^* of the volumetric representation showed a similar decreasing trend as it has been shown for the macro-porosity. The development of the surface roughness coefficient is presented in Fig. 15 B. The roughness kept decreasing in the load cycle ($R_a^* [0 Pa] = 0.58 \rightarrow R_a^* [3.6 Pa] = 0.55$) and increasing in the unload cycle ($R_a^* [3.1 Pa] = 0.535 \rightarrow R_a^* [0 Pa] = 0.57$). This smoothing of the biofilm structure is indicated by a harmonization of the color-coded biofilm thickness. In Fig. 14 this harmonization is dominant in the first three z-projections. Increasing shear stress is expected to align filaments of the biofilm matrix providing less friction to the flow. This reduces the roughness coefficient in consequence. During the load cycle large changes of the roughness coefficient occurred at a shear stresses of $\tau = 1.2$ and $2.8 Pa$, respectively. These show detachment events, which created a change in roughness. Picioreanu *et al.* (2000) showed in a 2D biofilm simulation that the two dominant processes of detachment, namely erosion and sloughing, alter the structure of the the bulk-biofilm interface differently. Erosion events are determined by detachment of small biofilm parts, which make the biofilm surface smoother. Sloughing on the other hand means that large parts detach, creating a rougher surface. Based on the simulation the dominant detachment process was presumably sloughing. In the unload cycle, the surface roughness coefficient increased linearly. Unlike the macro-porosity the roughness coefficient regained almost the same value than before the experiment. This is expected, since smoothing at higher shear stresses is a reversible process. Movement of (filamentous) structures sticking to the biofilm matrix and detachment have great impact on the surface roughness coefficient. This creates irreversible changes of the surface roughness. Surface roughness coefficient calculated for volumetric representations are always higher than those calculated for cross-sections. Volume scans have a greater variation in thickness as a result of uncovered parts on the substratum.

Viscoelastic deformation

Viscoelastic deformation occurred during the stress-strain experiment, which is visualized best in cross-sections. Fig. 16, shows a montage of two horizontal cross-sections of biofilm **IV**: **A** before the experiment ($\tau = 0 Pa$), **B** after the deformation (also $\tau = 0 Pa$), and a vertical cross-section **C** comparing both deformations. The white lines in **A** and **B** represent the location of cross-section **C**. The biofilm structure shown in **C** represents the deformed geometry after the deformation experiment ($\tau = 0 Pa$) and the white outline equals the biofilm geometry before the experiment. The overlay allows to qualify the structural change between the beginning and end of the stress-strain experiments. After the deformation, the structure did not regain its original shape as expected for a viscoelastic behavior of biofilms. At the upstream part, the biofilm structure deformed while at the downstream part detachment occurred. The detachment events fit with the roughness increases in Fig. 15 **B**. As mentioned before, changes in the mean biofilm thickness and measurement of the strain were calculated from single cross-sections of the volumetric representation (i.e. Fig. 16 **C**).

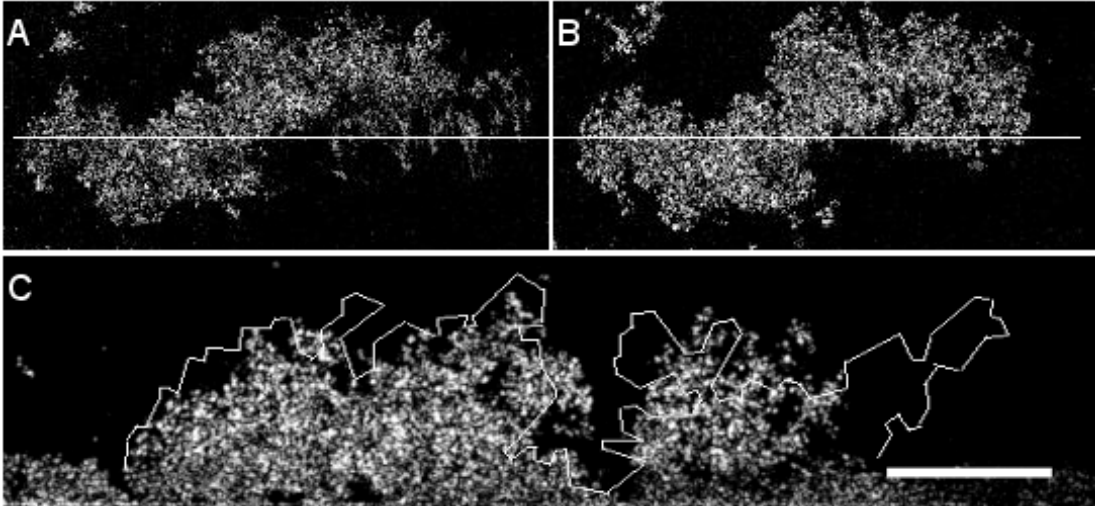


Figure 16: Viscoelastic deformation shown in an overlay of cross-sections. **A** horizontal cross-section of the biofilm before the deformation experiment at $\tau = 0 Pa$ and **B** horizontal cross-section after the experiment, also at $\tau = 0 Pa$. The white lines in **A** and **B** represent the location of the vertical cross-section **C**. **C** shows the deformed biofilm geometry with the white outline representing the biofilm structure before the deformation experiment, both at $\tau = 0 Pa$. The structure is visibly elongated as well as irreversible deformed at the front. Moreover, detachment occurred at the downstream part. Scale bar equals $250 \mu m$. Flow from left to right. Adapted from Blauert *et al.* (2015).

Fig. 17 **A** shows the change of the the mean biofilm thickness during the stress-strain experiment. The mean biofilm thickness decreased during the load cycle from $\bar{L}_F = 220$ to $160 \mu m$ ($\tau = 0 \rightarrow 3.56 Pa$), corresponding to an average compression of 27%. As the shear stress was increased in the load cycle, the mean biofilm thickness decreased as a result of compression. At $\tau = 1.2 Pa$ detachment occurred, shown by a reduced slope in the mean biofilm thickness curve. The compressible part detached, which leads to a reduced compression. During the unload cycle, the mean biofilm thickness increased linear to $\bar{L}_F = 175 \mu m$. This corresponds to 80% of the initial mean biofilm thickness of $220 \mu m$. A reduced biofilm thickness was expected due to detachment. However, the thickness recovery overcame the thickness after detachment (at $\tau = 1.2 Pa$), meaning that detachment did not influence the compression too much. Therefore, the reduced thickness corresponds to a viscoelastic deformation. This is supported by Fig. 16 **C**, showing the viscoelastic effect. Only a few experiments have been conducted visualizing a viscoelastic effect. Dreszer *et al.* (2014a) showed in a lab-scale cross-flow membrane filtration application that flow normal to the biofilm surface has a high impact on biofilm compression. They increased the permeate flux from 20 to $60 L \cdot m^2/h^2$ for 1 h, followed by a decrease to the original flux. In their experiment they imaged the recovery of the mean biofilm thickness of 75 % using OCT, which fits well to the compression measured here. However, comparing both experiments might lead to wrong interpretation, since the normal flow creating the shear stress is in flow cells along the flow (this thesis) and in membrane applications perpendicular. Nevertheless, both experiments demonstrated the viscoelastic properties of biofilms to stay in a deformed geometry.

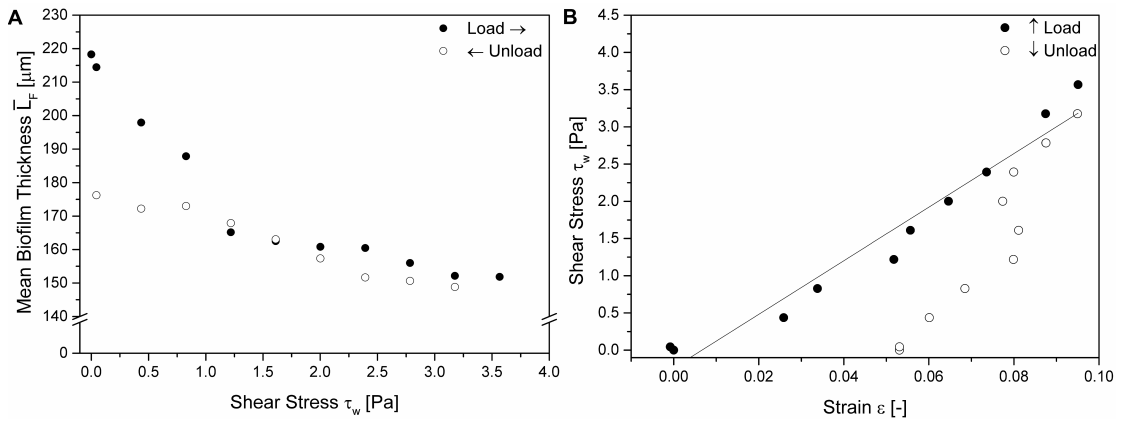


Figure 17: **A** displays the change in the mean biofilm thickness \bar{L}_F for the cross-sections, and **B** shows the measured strain ϵ to calculate the Young's modulus E from the slope of the stress-strain curve. Taken from Blauert *et al.* (2015).

Evaluation of the apparent Young's modulus

Furthermore, strain was calculated based on the center cross-section and linked to the shear stress. The stress-strain correlation is given in Fig. 17 B. In the load cycle, the applied shear stress τ was linearly correlated to the resulting strain ε (relative elongation along the flow direction). A linear fit allowed the estimation of the apparent Young's modulus E using eq. 30:

$$E = \frac{\tau}{\varepsilon} \quad (30)$$

The apparent Young's modulus was evaluated to equal $E = 36 \pm 3 \text{ Pa}$ ($n = 3$). This is in good agreement with other studies. Stoodley *et al.* (1999c) performed similar stress-strain experiments in flow cells and estimated an average apparent Young's modulus of $E = 40 \pm 8 \text{ Pa}$ for their biofilm, applying shear stresses up to $\tau = 10 \text{ Pa}$. They could report the viscoelastic behavior of biofilms and additionally found a shear thickening for shear stresses over $\tau = 5 \text{ Pa}$. Shear thickening implies that the change in strain increases slower at higher shear stresses, leading to a change in the slope of the stress-strain curve. Shear thickening was not detected in the stress-strain experiments performed in this thesis, probably as a result of a maximum applied shear stress of $\tau = 3.6 \text{ Pa}$. During the unload cycle, a hysteresis was detected and no clear correlation between applied shear and strain could be estimated in the unload cycle. A hysteresis not ending at a strain of $\varepsilon = 0$ is known for viscoplastic, rather than viscoelastic materials. If the strain stays positive ($\varepsilon > 0$) the deformation is permanent. Viscoelastic deformed materials show a hysteresis, but will regain their original shape after the stress is removed. This might take a long time, however the result is an intact structure. If the deformation is permanent, it is described as viscoplastic deformation. Hollenbeck *et al.* (2016) showed with a simple setup that biofilms do have an internal tensed EPS network. They could demonstrate that biofilms indeed behave as viscoplastic rather than viscoelastic material under consecutive shear stress testing. If the deformed biofilm is stretched beyond a yield strain, the resulting structure shows signs of a rearrangement of the EPS. The biofilm network is more tensed. This was true for several consecutive tests with different stresses and led to the conclusion that biofilms indeed show viscoplastic deformation. Guélon *et al.* (2011) discussed the possibility of viscoplastic deformation. Conclusive tests are still missing though. Due to the number of measurements demonstrating viscoelastic rather than viscoplastic deformation (Peterson *et al.*, 2015, Rupp *et al.*, 2005, Towler *et al.*, 2003, Klapper *et al.*, 2002, Peterson *et al.*, 2013, Lau *et al.*, 2009), biofilms are still considered to behave viscoelastic. Another technique to describe biofilm morphology and measure the Young's modulus on the microscale is atomic force microscopy (AFM). AFM is a powerful technique to image biofilm surface structures at nanometer resolution. The technique is often used to investigate single cell attachment on substrata or interfaces (Beech *et al.*, 2002, Lau *et al.*, 2009). Disadvantages, however, are the incapability to investigate insights of the structure as well as a destruction of the biofilm caused by the cantilever (Böl *et al.*, 2013). During the indentation of the can-

tilt into the biofilm structure, the cantilever bends and the disposition is correlated to a force needed to push into the structure. From the force and indentation depth a Hertz model is used to find an apparent Young's modulus. These measurements often find Moduli ranging in the kPa . Baniasadi *et al.* (2014) measured a Young's modulus of $E = 40 - 45 kPa$ for biofilms. These high values often relate to the measurement of the bacteria surface instead of the softer overall structure of the biofilm, including the EPS (Pelling *et al.*, 2005). Indentation however is not a realistic description of stresses on the biofilm in the environment. To understand the resistance of biofilms to withstand this great variety of stresses, techniques must be combined.

3.2.3 Material property variations in biofilms

Towler *et al.* (2003) found in rotating disk rheometry experiments with multispecies biofilms that the shear modulus was ranging between $G = 0.3 - 45 Pa$. This is not the only study reporting a certain range for material properties of biofilms. Böl *et al.* (2013) gave an overview over the variation of material properties. One reason for the variety might be due to different measurement techniques for the mechanical properties. Especially, when comparing measurements on the micro- and macroscale (μm vs cm). As discussed before, local heterogeneity makes it difficult to measure an exact value. Another reason concerns the change of the biofilm matrix composition. This varies from experiment to experiment as well as over time. Therefore, experiments under the same conditions might not result in same mechanical properties. Especially, when working with multispecies biofilms. The best estimation is to find the range of material properties under certain conditions, e.g. influence of substrate and Reynolds number during the cultivation. Macroscopic techniques such as rotating disc rheometry, average the mechanical properties for a biofilm. This makes it unusable for detailed local determination of material properties, which can be accessed by OCT image analysis.

Biofilm cultivation under same cultivation conditions and device can result in local variations of material properties. The influence of variations in biofilm material properties can be seen in Fig. 18. Biofilm **V** was cultivated with acetate at a Reynolds number of $Re = 165$. The Figure shows the deformation of biofilm patches in a stress-strain experiment. As a result of increasing shear stress, single patches detached. Knowing the maximum stresses the biofilm withstood before detachment allowed to estimate the shear modulus from each biofilm patch individually. For biofilm patches 3 and 4, which detached first, an angle of deformation of $\alpha = 9.8^\circ$ was measured at $\tau = 2.5 Pa$. This relates to a shear modulus of $G = 14.6 Pa$. For biofilm patch 2 a deformation of $\alpha = 7.4^\circ$ was measured at $\tau = 3.6 Pa$, relating to $G = 27.9 Pa$. Biofilm patch 1 withstood the highest shear stresses tested ($\tau = 3.8 Pa$) deforming with an angle of $\alpha = 5.0^\circ$. This corresponded to a shear modulus of $G = 43.5 Pa$ (shown in Table 6). Biofilms with high shear moduli are able to absorb more stress by deformation before a yield stress is reached and the biofilm detaches from the substratum. The experiment confirmed that

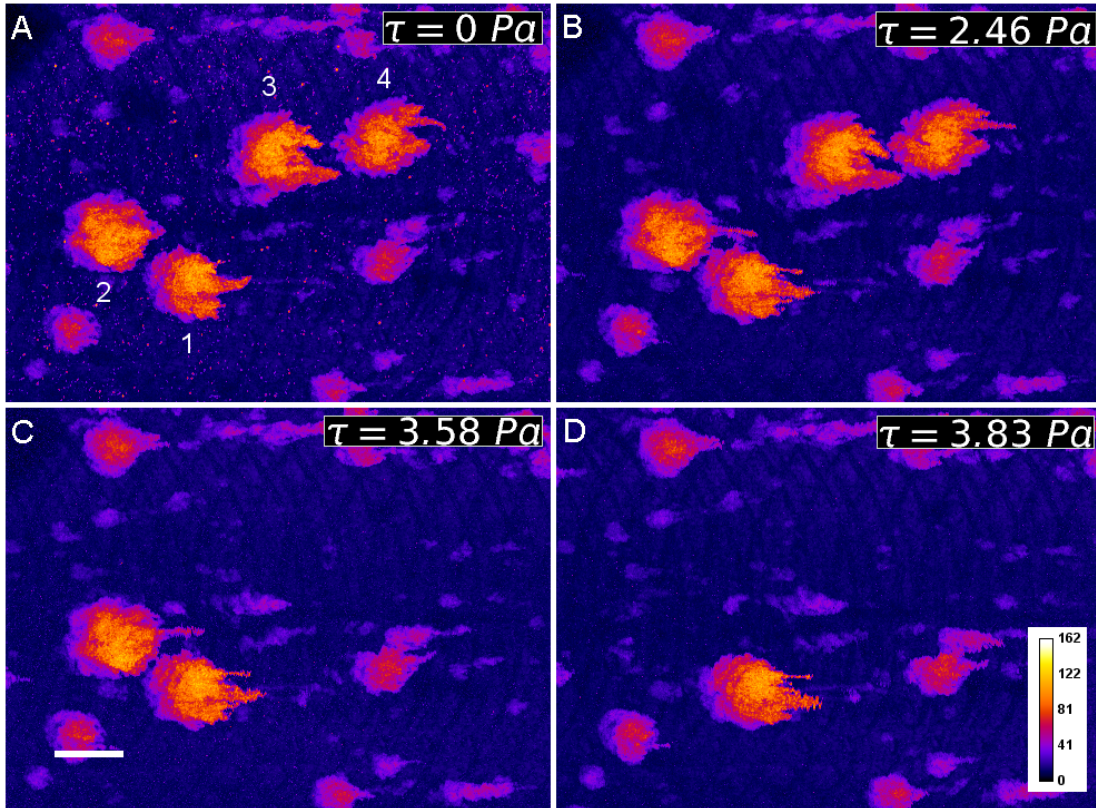


Figure 18: Variances in material properties of biofilm **V**. Top-view onto the biofilm patches. **A** without flow, **B** at maximum deformation before detachment occurs, **C** patches 3 and 4 detached, **D** patch 2 detached. Calibration bar in μm . Scale bar equals $250 \mu m$. Flow from left to right.

variances of the shear modulus occur in biofilms cultivated in the same device under same cultivation conditions. One reason for the different mechanical stability of the patches can be attributed to the shielding of the downstream patches from the hydrodynamic stress. The highest exposure of shear stress is at the upstream side of the first biofilm patch, which was more rigid than the separate patches (3 and 4) downstream. This correlates with the assumption that cultivation under more stress results in more stable biofilms (Dunsmore *et al.*, 2002). However, even though the upstream biofilm was exposed to the highest shear stresses during cultivation, it did not develop the most stable structure. The remaining biofilm patch 2 developed a structure with the highest shear modulus, which might have had a profit from the shelter of biofilm patch 1.

Table 6: Local material property variations of a biofilm. The shear modulus decreases from patch 1 to 4. Patches shown in Fig. 18.

Biofilm patch	1	2	3	4
shear modulus G [Pa]	43.5	27.9	14.6	14.6

3.3 Dependence of mechanical properties on substrate and Reynolds number

The methods introduced in chapter 3.2 were used to investigate the influence of different substrates and Reynolds numbers during the cultivation on the mechanical properties of biofilms. Three substrates were chosen which were supposed to change the composition and mechanical properties of the biofilm matrix: Na-acetate, D-glucose, and L-phenylalanine. These substrates were the only carbon source available for the bacteria. Five Reynolds numbers were chosen for the cultivation ranging from $Re = 11 - 472$. Stoodley *et al.* (1999a) studied the influence of hydrodynamic drag and glucose concentration on the development of biofilms structures. However, imaging capabilities and data interpretation were limited at that time. Therefore, they could only show that biofilms, which developed at low Reynolds numbers ($Re = 120$) differ from biofilms cultivated under high (turbulent) Reynolds numbers ($Re = 3600$). At $Re = 120$ biofilms formed circular-shaped microcolonies and at $Re = 3600$ biofilm streamer with an elongated tail developed. A more systematic investigation was needed. Biofilms were cultivated in flow cells until single patches were visibly large enough to perform stress-strain experiments. Each substrate was tested in triplicate for individual Reynolds numbers during cultivation. The biofilm formation was monitored daily using OCT. Biofilm thickness, surface roughness, and macro-porosity were followed over time, and the final values were linked to mechanical properties.

3.3.1 Cultivated biofilms

Fig. 19 shows a time-series of depth-coded height maps (z-projections) to visualize the biofilm formation in 3D. The view is from top to bottom into the flow cell channel. A specific $2\text{ mm} \times 2\text{ mm} \times 1\text{ mm}$ volume was visualized over time to follow changes non-invasively and *in situ*. In total 36 experiments developed a biofilm structure with separated patches suitable for stress-strain experiments.

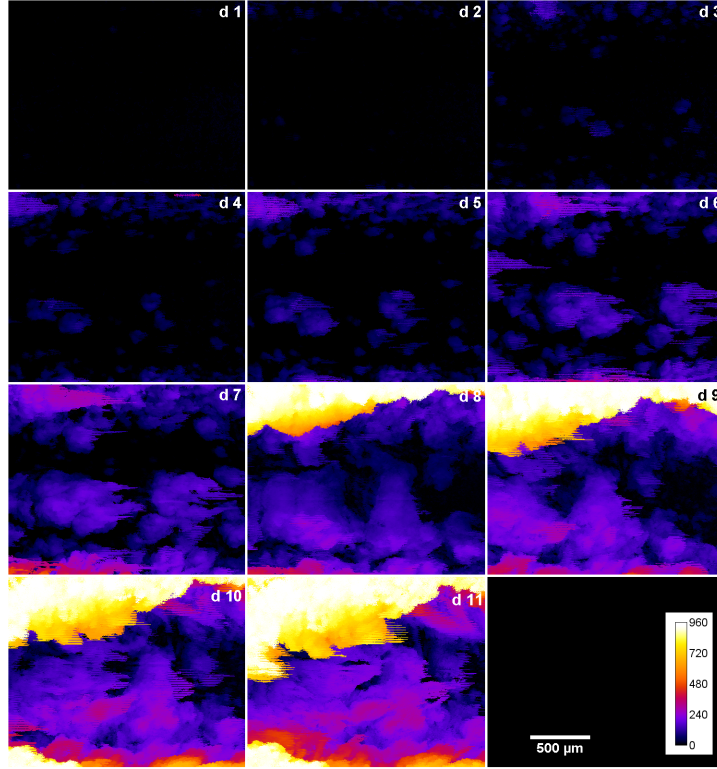


Figure 19: Z-projections of biofilm **VI** (cultivated with acetate). The time-series shows the biofilm development at $Re = 139$ over 11 days of cultivation in the flow cell (visualized volume equals $2 \text{ mm} \times 1.8 \text{ mm} \times 1 \text{ mm}$). Exponential growth started around day 6. Calibration bar in μm . Flow from left to right.

Mean biofilm thickness

The mean biofilm thickness is an important indicator whether the biofilms experience a similar shear stress during the stress-strain experiments or not. Since the flow velocity increases toward the center of the flow cell, so does the shear stress. On average the biofilm structures should possess a similar biofilm thickness to experience the same amount of stress. Therefore, biofilm patches with similar mean biofilm thicknesses were investigated in stress-strain experiments. The mean biofilm thicknesses for all experiments are shown in Fig. 20 **A**. The thicknesses are low for the smallest Reynolds number ($Re = 11$) due to the missing shear stress. This has already been demonstrated experimentally by comparing cultivation under static (no flow) and shear stress (flow) conditions (Al-Fattani and Douglas, 2006, Hawser *et al.*, 1998). Biofilms cultivated with glucose or phenylalanine tend to converge towards $\bar{L}_F \approx 200 \mu\text{m}$ for all other cultivation velocities. The variance of the mean biofilm thickness shows a widespread distribution of the thicknesses. This is due to the fact that the biofilm structure starts to cover the walls and top of the flow cell channel. If the biofilm structures forming on the top are not directly connected to the rest of the biofilm through the side walls, the image processing macro is able to distinguish between these structures. If not, the thickness is

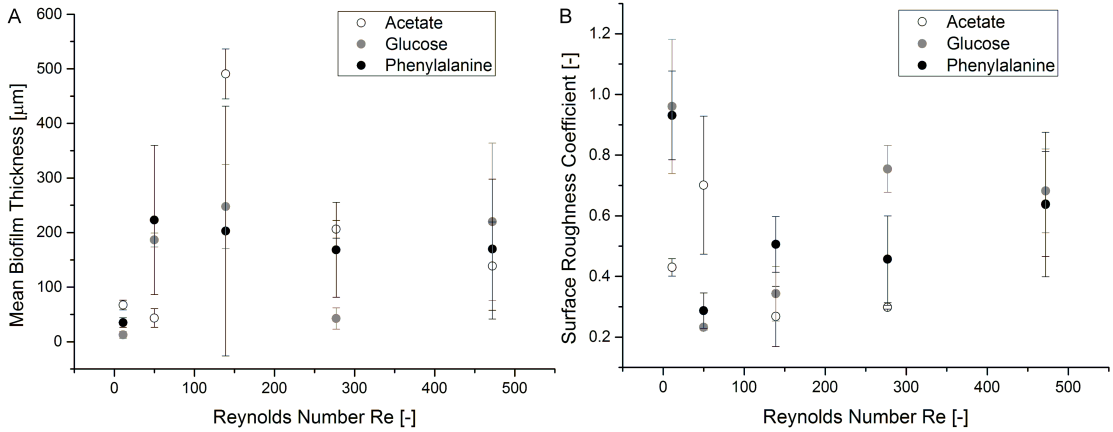


Figure 20: Final biofilm thicknesses before the stress-strain experiments.

artificially increased and the variance might become as large as the mean thickness itself. Examples are the biofilm structures cultivated at a Reynolds number of $Re = 139$. The thickness of the acetate biofilms, cultivated at $Re = 139$, showed an average value of $\bar{L}_F \approx 500 \mu m$. This would fill half of the flow cell. The large variance of the phenylalanine biofilms at this Reynolds number result from the same phenomenon. It is expected that the biofilm thickness of the bottom structures was less.

Surface roughness coefficient

Fig. 20 **B** shows the roughness coefficient at different cultivation conditions before the deformation experiments. Biofilms cultivated with glucose or phenylalanine developed more similar rough structures compared to cultivation on acetate. This can be linked to the mean biofilm thicknesses. Biofilms, which cover the flow cell mainly as patches, create a rougher surface than a smooth thick biofilm, since the roughness indicates the biofilm thickness variation. At low Reynolds numbers during cultivation the roughness coefficient R_a^* is higher. As the Reynolds numbers increase, it is expected that the biofilms develop smoother structures. The higher fluid flow prevents filamentous structures to form in order to reach more substrate. However, the roughness coefficient converged towards $R_a^* \approx 0.65$ for Reynolds numbers $Re > 200$. Picioreanu *et al.* (2000) investigated in a theoretical study the influence of the surface roughness on substrate conversion and found that a rougher biofilm is more beneficial than a smooth one, to a certain degree. However, the biofilm model was a rigid and not moving geometry, which does not describe real biofilm systems. Nevertheless, a high surface roughness coefficient is usually expected to be more beneficial for mass transfer into the biofilm structure. The common explanation is that overall mass transfer will increase with an enhanced biofilm-liquid interface. Picioreanu *et al.* (2000) stated, if the surface roughness is too high, the concentration boundary layer can not follow the structure silhouette and it remains outside the biofilm. Consequently, a larger biofilm surface area is only beneficial to a certain extend. Otherwise there is poor convective transport towards the biofilm.

Macro-porosity

The final macro-porosities before the stress-strain experiments are shown in Fig. 21. As it would be expected, the macro-porosity decreased as the Reynolds number was increased during cultivation. It is expected from biofilms developing under higher stress to develop denser structures (Dunsmore *et al.*, 2002). Under slower fluid flows the macro-porosity of biofilms, cultivated with acetate, is lower than for those cultivated with glucose or phenylalanine. At Reynolds numbers above $Re = 100$ the macro-porosities of all biofilms converged towards similar values, ranging between 20 – 45%. Such small macro-porosities are not unexpected and have been reported in other OCT related publications (e.g. Blauert *et al.* (2015) or Wagner *et al.* (2010b)). At a Reynolds number of $Re = 472$ the porosities of all biofilms developed towards a similar value. This leads to the conclusion that differences in material properties between biofilms cultivated with either acetate, glucose, or phenylalanine must be due to internal arrangements of the biofilm matrix.

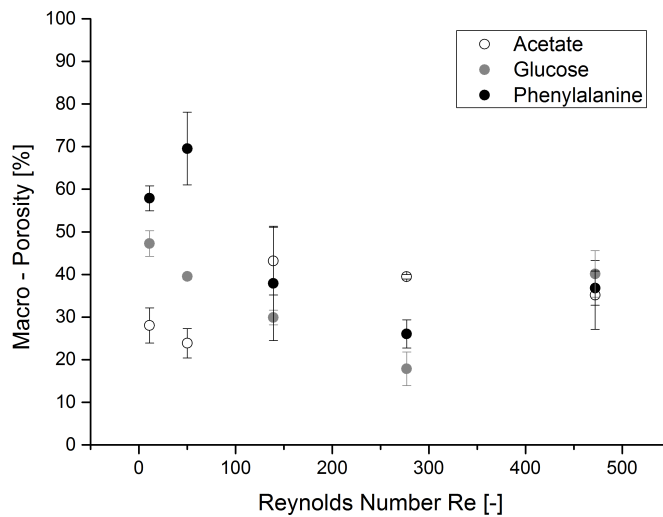


Figure 21: Porosity for the five Reynolds numbers during cultivation, before the deformation experiments.

3.3.2 Influence of cultivation conditions on the shear Modulus G

The evaluation of material properties in combination with OCT (which was introduced in chapter 3.2) relied on the estimation of the shear stress using eq.5. It was mentioned before that this idealized formula does not represent the optimal description of stresses acting on the biofilm boundary. Therefore, an improved estimation of the shear stress acting onto the bulk-biofilm interface was gained from the fluid-structure interaction simulations, and is further discussed in chapter 3.4. The shear modulus was evaluated for the three different substrates under five different Reynolds numbers during cultivation ($Re = 11, 55, 139, 277, 472$). The shear modulus was more reliable to measure compared to the Young's modulus, since only an angular change had to be determined from the deformed structures. This was possible for most biofilm structures. In total 52 biofilm patches could be analyzed. All evaluated material properties are listed in Table 9 (page 72).

Fig. 22 gives an overview how the shear modulus G is influenced by the Reynolds number during cultivation for the three substrates tested. An overview over all evaluated material properties is given in chapter 3.3.8 Table 9. It was expected that the biofilm matrix develops a stability proportional to the Reynolds number (and therefore the shear stress) during cultivation. The shear modulus of acetate biofilms first showed a decreasing pattern from $Re = 11 - 139$. At the low fluid flow conditions of $Re = 11$ only acetate biofilms developed colonies with sufficient large structure to measure material properties. Colonies proved to be stable structures with shear moduli ranging between $G = 15 - 65 Pa$. Under slower fluid flows the macro-porosity of acetate biofilms was lower than for glucose and phenylalanine biofilms. This might explain the more rigid acetate biofilms at $Re = 11$ and 55 . The low shear moduli towards $Re = 139$ were related to the thickness of the biofilm patches. At $Re = 139$ the measured mean biofilm thickness reached up to $\bar{L}_F \approx 500 \mu m$ (see Fig. 20 A). The closer the structures come towards the center of the flow channel, the higher the shear stress from the fluid flow. This is a consequence from the reduction of the channel cross-section. Acetate biofilms cultivated under higher Reynolds numbers ($Re = 130 - 472$) showed the expected increase of the shear modulus.

Biofilms cultivated with either glucose or phenylalanine showed an increasing shear modulus for the tested range of Reynolds numbers during cultivation. The material property variation of glucose biofilms changed from the cultivation at $Re = 55$ with $G = 6 - 25 Pa$, to $G = 15 - 55 Pa$ at $Re = 139 - 277$. At the highest Reynolds number ($Re = 472$) the shear modulus reached $G = 133 - 158 Pa$. The biofilms cultivated with phenylalanine showed a similar development of the mechanical properties. The distribution is smaller compared to glucose biofilm, but the trend is similar. At low Reynolds numbers the shear modulus of phenylalanine biofilms ranged between $G = 11 - 13 Pa$, increasing towards high shear moduli at $Re = 472$ of $G = 102 - 155 Pa$.

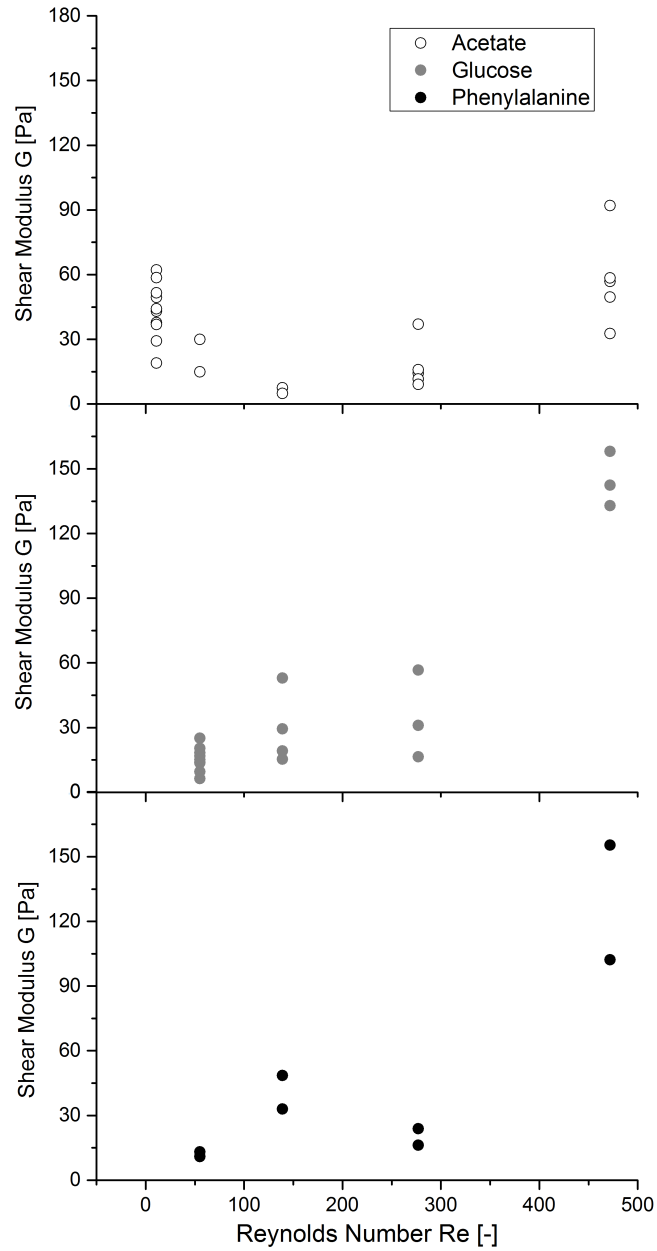


Figure 22: Development of the shear modulus G for biofilms cultivated under increasing Reynolds numbers with three substrates: sodium-acetate (top row), D-glucose (middle row), and L-phenylalanine (bottom row).

Table 7: Ranges of experimentally determined shear moduli from flow cell setups.

Range	Unit	Species	Reference
27	Pa	mixed culture	Stoodley <i>et al.</i> (1999c)
29.7	Pa	mixed culture	Blauert <i>et al.</i> (2015)
0.9 – 5	Pa	<i>S. aureus</i>	Rupp <i>et al.</i> (2005)
0.3 – 45	Pa	mixed culture	Towler <i>et al.</i> (2003)
0 – 280	Pa	<i>P. aeruginosa</i> (diff. strains)	Stoodley <i>et al.</i> (2002)
190 – 380	Pa	<i>S. mutans</i>	Vinogradov <i>et al.</i> (2004)
6 – 158	Pa	mixed culture	this study

The shear moduli evaluated fit well in the range of $G = 5 - 380 Pa$ found with other techniques (see Table 7). However, direct comparison to other techniques is difficult. Even though all techniques aim to measure the same material property, the ways to quantify differ from experiment to experiment. Flow cell experiments mimic more realistic environments compared to shear rheometry or compression measurements, providing moduli more relevant to real world applications. Both, glucose and pheylalanine biofilms developed quite similar structures in terms of the mean biofilms thickness and surface roughness coefficient. Since the estimated material properties are close too, this implies that the micro-structure of the EPS must be responsible for the difference in stability rather than the chemical composition.

3.3.3 Influence of cultivation conditions on the Young's modulus E

The trend for the Young's modulus is similar to the trend of the shear modulus. The determination of the modulus itself is restricted to measure the relative elongation of the biofilm structure (strain), which was impossible for some patches. At high shear stresses structures moved too fast to be captured clearly with OCT. Therefore, the tested range contains less data compared to the shear modulus.

In Fig. 23 the development of the Young's modulus E under increasing Reynolds numbers during cultivation is shown. Acetate biofilms showed the expected trend of increasing moduli. The Young's modulus ranged between $E = 24 - 130 Pa$. Bacteria cultivated with glucose showed a similar trend of increasing Young's modulus. However, the Young's modulus showed smaller values compared to acetate biofilms, especially for lower Reynolds numbers during cultivation ($Re = 55$ and 139). For glucose biofilms a Young's modulus between $E = 4 - 113 Pa$ was evaluated. Phenylalanine biofilms showed the same distribution of the Young's modulus than with the shear modulus, ranging between $E = 9 - 58 Pa$. However, a clear trend could not be given, since data for $Re = 472$ could not be evaluated for the experiments. The Young's moduli evaluated in this study fit well in the range of moduli from literature, under similar conditions (flow cells, see Table 8). Other tests of the mechanical strength of biofilms, such as compression measurements, were investigated by Paramonova *et al.* (2009) and others. These measurements are close to the values evaluated in flow cell experiments ($E = 17 - 310 Pa$). In the experiments of Paramonova *et al.* (2009) biofilms were compressed arbitrarily by 20% (a strain of $\varepsilon = 0.2$), and the Young's modulus was calculated as the applied stress over strain (eq. 11). Single compression measurements include the assumption of the biofilm matrix behaving as ideal homogeneous elastic material. In this case the evaluation from one strain would suffice in the elastic region. However, it was demonstrated that biofilms will change porosity during deformation, resulting in a consolidation of the biofilm matrix. A single strain measurement might lead to wrong conclusions. Other techniques can lead to even larger Young's moduli. Körstgens *et al.* (2001b) used uniaxial compression measurements and determined a Young's modulus of $E = 6500 Pa$, which is 20-fold higher than deformation experiments in flow cell setups. They assigned these findings to the expected range of weak polymer gels. Even higher moduli can be reached with atomic force microscopy (AFM). In AFM experiments a cantilever with a sharp tip, in the micrometer range, is lowered onto the biofilm structure. When the cantilever touches the biofilm matrix, it deforms and the corresponding force, until failure, is recorded. These force measurements over depth can be used to evaluate the Young's modulus via the Hertz model (Roa *et al.*, 2011). Experiments by Chen *et al.* (2014) and others measured Young's moduli ranging between $E = 7 - 22 kPa$, manifold higher than the values evaluated in flow cell measurements. However, AFM measurements need to be interpreted carefully. Manufactures (e.g. JPK) hint the user the limits of AFM in biological samples. The Hertz model is only valid for

the first few hundred nanometer of indentation (JPK, 2008). This is a serious limitation, mainly due to the measuring depth of several tens to hundreds of micrometer measured in AFM experiments. Furthermore, it is likely that the cell wall rather than the EPS is measured, resulting the expected range of kP for the stiffer cell walls. This shows the importance of carefully interpreted experiments.

Similar to the study presented here, Stoodley *et al.* (2001b) investigated the influence of Reynolds numbers during cultivation on the Young’s modulus in flow cells, too. They used rectangular glass flow cells and imaged the biofilms from the side with light microscopy. This produced a crude silhouette of the whole biofilm within the cell. Only the overall outline of the biofilm structure was visible. The drawback was that parts of the biofilm structure might have overlapped others. Therefore, a less accurate interpretation of the strain could result from these measurements. However, they could show a positive correlation between the increasing Reynolds number and increasing Young’s modulus. One explanation of Stoodley *et al.* (2001b) was that lower molecular weight components, which filled interstitial voids, could have been washed out of the EPS leaving a stronger matrix. Battin *et al.* (2003) showed that certain types of biofilms contain a large amount of mono sugars, which might influence the stability. It is known that hydrogels with high porosity can form a stable network (discussed in detail in section 3.3.7). Also selection for bacteria, which produced a stronger EPS matrix, is possible. However, there exists a more active response in which biofilm cells can sense shear stress and regulate the strength of their EPS accordingly. This is called mechanosensing and has been studied and discussed thoroughly by Harapanahalli *et al.* (2015). Bacteria cells are able to react to cell wall deformation. This creates a chemical signal, which triggers the bacteria to react to invoking shear stress. The consequence is enhanced production of EPS or changes in the EPS composition. The correlation of the material properties with the macro-porosity is similar to the shear stress. However, the Young’s modulus has been investigated more thoroughly, especially with metals, metal foams and ceramics.

Table 8: Ranges of experimentally determined Young’s moduli from flow cell setups.

Range	Unit	Species	Reference
40	Pa	mixed culture	Stoodley <i>et al.</i> (1999c)
36	Pa	mixed culture	Blauert <i>et al.</i> (2015)
65	Pa	<i>P. aeruginosa</i> (PAO1)	Klapper <i>et al.</i> (2002)
1 – 33	Pa	<i>Desulfovibrio sp.</i> (EX265)	Stoodley <i>et al.</i> (2001b)
20 – 240	Pa	<i>P. aeruginosa</i> (PAO1)	Stoodley <i>et al.</i> (1999c)
1 – 336	Pa	<i>P. aeruginosa</i> (PAO1)	Stoodley <i>et al.</i> (2001b)
4 – 130	Pa	mixed culture	this study

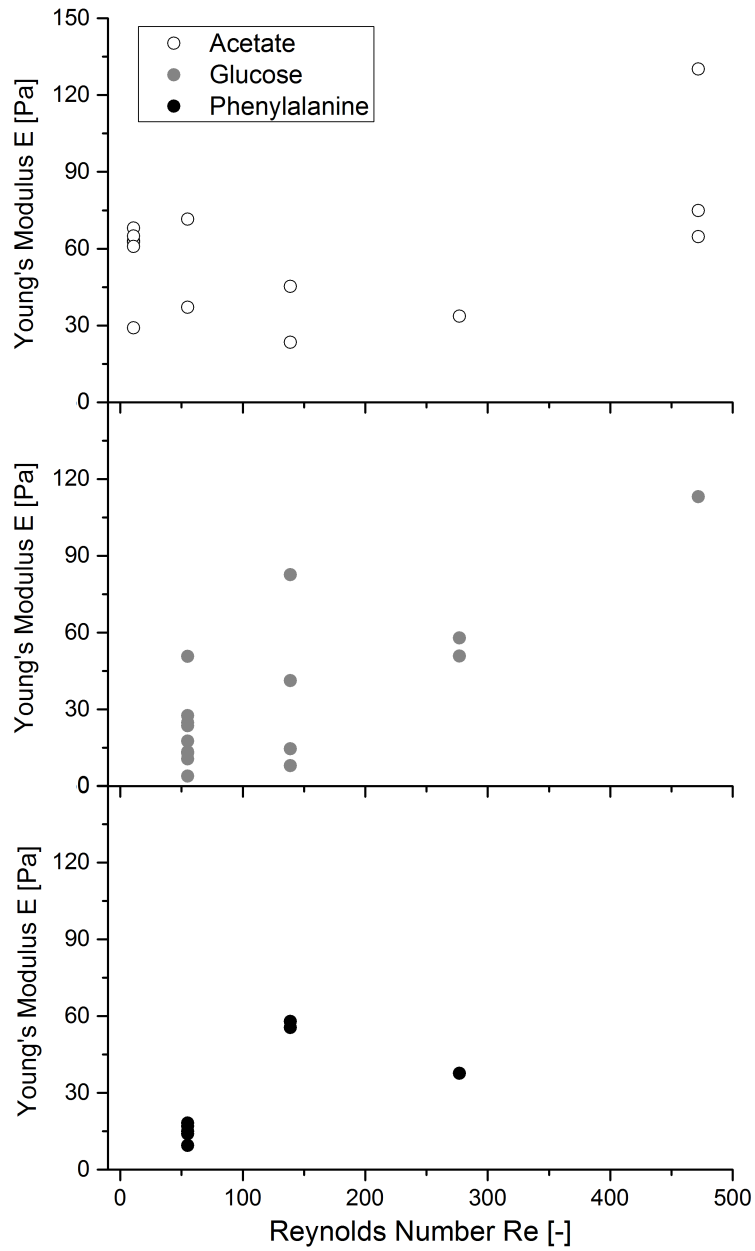


Figure 23: Development of the Young's modulus E for biofilms cultivated under increasing Reynolds numbers with three substrates: sodium-acetate (top row), D-glucose (middle row), and L-phenylalanine (bottom row).

3.3.4 Influence of porosity on material properties

It has been known for several decades that material properties depend on the porosity of the material. It has been shown in the 1950s that empirical formula can describe very well the dependence of mechanical strength on porosity for ceramics and polycrystalline metal (Knudsen, 1959). Metals and ceramics tested showed a good relationship between the Young's modulus E of the material and the porosity P :

$$E = E_0 \exp(-bP) \quad (31)$$

This equation is known as the Ryshkewitch-Duckworth or Spriggs' equation (Ryshkewitch, 1953, Spriggs, 1961). E_0 describes the theoretical Young's modulus without porosity, while b is an arbitrary constant for the metal/ceramic. This formula worked well except for high porosities. Since it is an empirical formula it fails to satisfy the boundary condition that the Young's modulus becomes zero for $P = 1$. When the porosity reaches 100%, there is no material any more, only voids. Therefore, the Young's modulus must become zero. As the porosity increases, the material runs into a limitation of contact points between parts of the material itself. Phani and Niyogi (1987) considered a more theoretical approach. The easiest equation, which satisfies the boundary conditions $E = E_0$ at $P = 0$ and $E = 0$ at $P \leq 1$, was a power function in the form of $(1 - aP)^n$ in which a and n are material constants:

$$E = E_0(1 - aP)^n \quad (32)$$

The material constant a can be defined as the inverse of a critical porosity P_{crit} for which the Young's modulus becomes zero ($a = 1/P_{crit}$). This implies an interesting physical meaning that there exists a porosity limit for natural materials, which is valid for biofilms, too. This creates the basis for the understanding of increasing Young's moduli with decreasing porosity during the biofilm deformation.

To find out whether the macro-porosity during cultivation has an influence on the material properties or not, the shear as well as Young's modulus were plotted versus the porosity in Fig. 24. Ideally, a correlation of the moduli versus the porosity should show an increase of the material properties towards $\Phi = 0$. For the shear modulus this is not true. Fig. 24 **A** shows that biofilms with the highest shear moduli possess porosities around 40%. There is no clear trend indicating a connection between the shear modulus and the porosity. The stability of biofilms is more complex than the dependency of the porosity alone. The heterogeneity plays a crucial role. Rearrangement of EPS, connectivity of the EPS constituents and density variation in the biofilm matrix complicate this matter. The Young's modulus in Fig. 24 **B** shows a clearer trend. As the porosity decreases, the Young's modulus increases. However, this is only valid considering all biofilms. Looking at the individual substrates does not show a clear trend either. Again the highest Young's moduli were found at porosities around 40%.

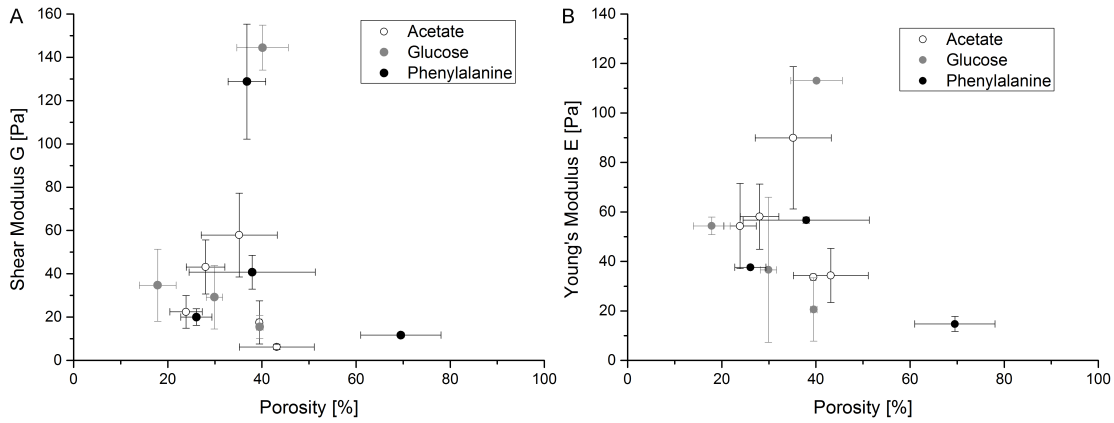


Figure 24: Correlation of the shear modulus **A** as well as Young's modulus **B** with the porosity.

3.3.5 Shear strength of biofilms

During deformation experiments all biofilm patches showed a general resistance to deform for low shear stresses. Shear strength is the resistance of a material to deform, until a certain shear stress is reached. Wloka *et al.* (2004) and Wloka *et al.* (2005) investigated this phenomenon with *P. aeruginosa* biofilms and related the resistance to the polysaccharide network, which hold the structure together. Fig. 25 shows exemplary the relative mean biofilm thickness change in a stress-strain experiment for a Reynolds number of $Re = 139$. It is evident that the biofilms, regardless of their substrate, withstand shear stresses of $\tau \approx 2 Pa$. At higher shear stresses the biofilm thickness decreases. This was valid for all substrates and Reynolds numbers during cultivation. Aggarwal

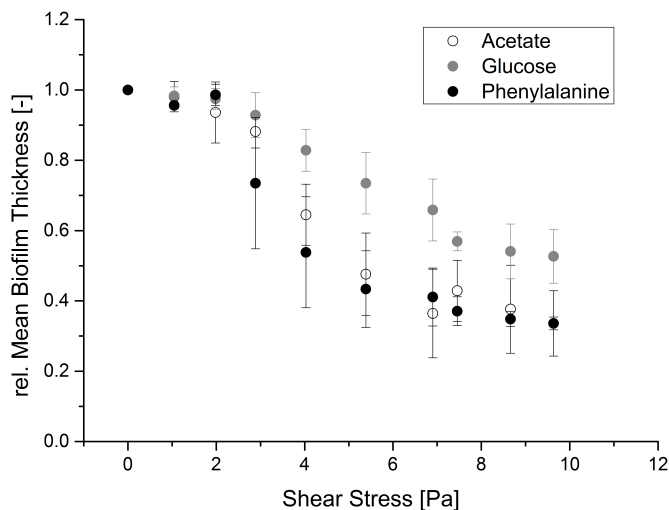


Figure 25: The change of relative mean biofilm thickness in a stress-strain experiment is exemplary shown for a Reynolds number of $Re = 139$.

et al. (2015) investigated the cohesive strength of biofilm. Heterotrophic biofilms were cultivated in a rotating disc reactor under defined hydrodynamic conditions ($\tau = 0.07, 0.18$ and $1.9 Pa$). The cultivated biofilms were stretched with a cantilever until failure. From the measured force needed to stretch the material, the cohesive strength was calculated and related to the shear stress during cultivation. This ratio is known as factor of safety (*FOS*) and widely used in engineering for constructing bridges and buildings. Adapting this to biofilms they showed that the biofilm structure withstands several hundred times the shear force of the liquid ($FOS = 330 - 55,000$). This can be calculated for every experiment testing cohesive strength (not flow cell experiments though). In experiments by Möhle *et al.* (2007), who used fluid dynamic gauging to test the cohesive strength of biofilms, the calculated factor of safety ranged between $FOS = 200 - 1,100$. The estimation of shear stress onto the bulk-biofilm interface is one fact, which might underestimate the shear stress during cultivation. Therefore, the *FOS* values might be overestimated. Nevertheless, it appears that bacterial biofilms developed to withstand high shear forces and not just typical or average applied forces. Douarche *et al.* (2015) and Hollenbeck *et al.* (2016) showed similar structural tension of a *B. subtilis* biofilm cultivated in a rectangular petri dish. An air-liquid interface biofilm attached on one side on the petri dish wall and on the other side to a force sensor. By stretching the biofilm (strain) they could measure the corresponding force inside the biofilm structure. They found that these biofilms form a specific internal network during cultivation. The biofilm showed a compressive force until it was stretched to a strain of $\varepsilon = 0.25$. Stretching the biofilm further resulted in a tension. This is associated with re-arrangement of the EPS during the stretching. Validating that unstressed biofilms have a certain stress inside to withstand stresses from outside (e.g. shear stress during cultivation).

3.3.6 Biofilm relaxation after deformation

During the unload cycle of the stress-strain experiments the biofilm regains its uncompressed structure. The pores fill with liquid again, the structure is pushed upwards, and the internal structure is rearranged/rebuild over time. Possible detachment only occurred in the load cycle, when the shear stress was increased. Therefore, the final biofilm thickness at $\tau = 0 Pa$ can be assumed as completely relaxed biofilm. This final mean biofilm thickness was used to extract the rel. biofilm relaxation. The rel. biofilm relaxation is the slope of the increasing mean biofilm thickness as the shear stress decreases. This value quantifies how much of the thickness is restored by reducing one pascal of shear stress from the highest shear load. It is different from the shear and Young's modulus. The biofilm relaxation measures the change in the biofilm thickness, perpendicular to the flow, while the moduli determine a resistance along the flow. Fig. 26

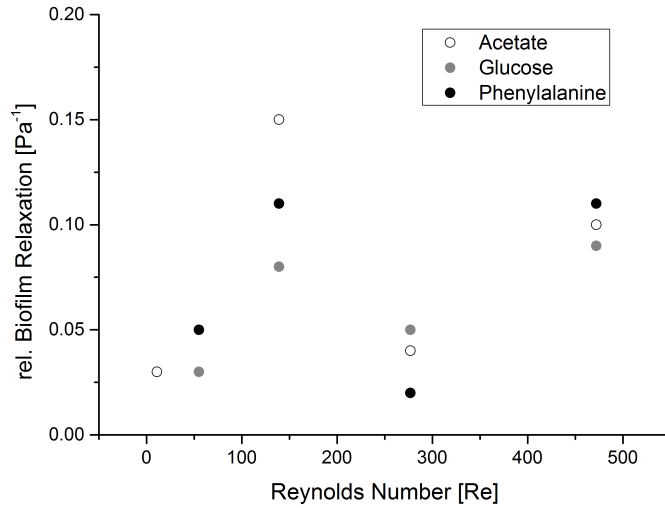


Figure 26: The relaxation constant expresses how much thickness is restored after one pascal of the maximum shear stress is reduced.

shows the relaxation of the biofilms for the five Reynolds numbers during cultivation. Biofilms recovered 2 – 10% of their final thickness after the shear stress was reduced. The biofilm structures have been shown to compress between 6% in shear stress experiments (Blauert *et al.*, 2015), and 25% in membrane reactor experiments in which the flux was increased (Dreszer *et al.*, 2014b). The high relaxation of biofilms cultivated at $Re = 139$ is related to the high biofilm thicknesses measured (see chapter 3.3.1). As mentioned above, there is a difference between compression perpendicular and along the flow. Therefore no direct correlation between relaxing biofilms and shear or Young's modulus could be found.

3.3.7 Poisson's ratio ν of biofilms

Poisson's ratio describes the perpendicular contraction most elastic materials show when stretched. Fig. 27 illustrates how the Poisson's ratio is defined. It is the ratio of transverse strain ε_z to longitudinal strain ε_x , with respect to the direction of the applied stress:

$$\nu = -\frac{\varepsilon_z}{\varepsilon_x} \quad (33)$$

The definition of Poisson's ratio has a minus sign, since most materials contract laterally when stretched, and expand when compressed. The Poisson's ratio for such materials is then positive. Compact and little compressible materials, such as rubber or a liquid, have Poisson's ratios ~ 0.5 (Greaves *et al.*, 2011). These materials often show no or little compression, when stress is applied. They rather tend to change shape, therefore deform. Since biofilms are highly hydrated structures it was assumed for a long time that the Poisson's ratio is close to $\nu \sim 0.5$. For solids such as metals, polymers, and ceramics the Poisson's ratio ranges between $0.25 < \nu < 0.35$. Glasses and minerals, which are more compressible, have a Poisson's ratio of $\nu \approx 0$. These materials possess interesting features. Cork is one of those materials. If cork had a Poisson's ratio $\nu \gg 0$ and would be pushed in a wine bottle, the bottle neck would explode from the expanding cork structure. The change in shape and size can be expressed in terms of the shear modulus G and bulk modulus K . The Poisson's ratio is related to these two by:

$$\nu = \frac{3K - 2G}{2(3K + G)} \quad (34)$$

When the bulk modulus greatly exceeds the shear modulus the Poisson's ratio approaches $\nu = 0.5$, as in rubbery solids, and the material is referred to as incompressible (mainly deformation). But when the bulk modulus is much smaller than its shear modulus, the Poisson's ratio approaches $\nu = -1$, the material becomes highly compressible. This defines the numerical limits for Poisson's ratio, $-1 \leq \nu \leq 0.5$ for $0 \leq K/G < \infty$.

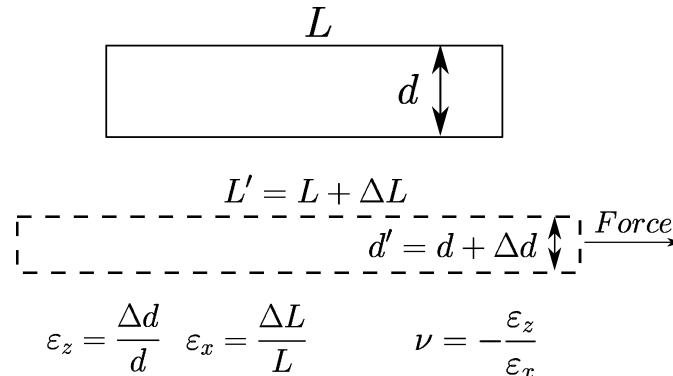


Figure 27: Scheme of the Poisson's ratio ν . The ratio of transverse ε_z and longitudinal ε_x strains defines the Poisson's ratio.

From a thermodynamical point of view, materials with negative Poisson's ratios do exist. These materials are called 'auxetics'. This terminology was introduced by Evans (1991), when he first fabricated microporous polyethylene with a negative Poisson's ratio. This contra-intuitive material does expand vertically when stretched instead of contracting. The idea of microstructures being responsible for the auxetic effect came up and mathematical simulations followed soon. Saxena *et al.* (2016) give a good overview over the different microstructures and thermodynamic considerations for negative Poisson's ratios. One of the most recognized microstructures with a negative Poisson's ratio is the inverted honeycomb.

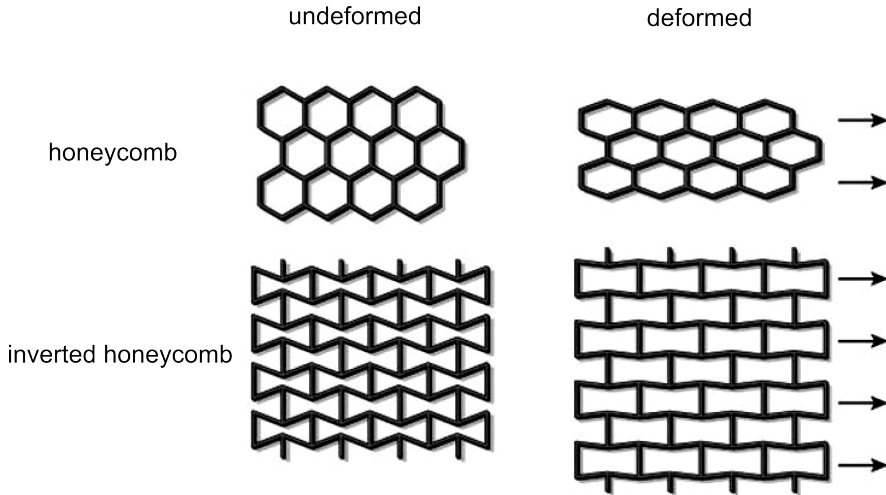


Figure 28: Scheme of the normal and inverted honeycomb structure. The left side displays both structures without deformation, while the right side displays the different deformation behavior under stretching (arrows). The inverted honeycomb, an auxetic structure, expands perpendicular to the stretch.

Anisotropy plays a crucial role for the auxetic effect. The inverted honeycomb structures displayed negative Poisson's ratios only in certain directions. Fig. 28 shows the schematic of a honeycomb and an inverted honeycomb structure. Stretching the material along the arrows contracts the honeycomb structure laterally, while the inverted honeycomb structure expands. Stretching the inverted honeycomb structure perpendicular to the arrows results in a structural change towards the normal honeycomb structure and its deformation process. The effect might only occur in some directions and is highly dependent on the interaction of stretching force and shear deformation. Due to lack of experimental data, the value for the Poisson's ratio of biofilms has been assumed to range between $\nu = 0.3 - 0.5$. The Poisson's ratio connects the Young's modulus E and shear modulus G via:

$$G = \frac{E}{2(\nu + 1)} \quad (35)$$

Hence, a plot of the Young's modulus versus the shear modulus gives the Poisson's ratio

as a function of the slope k :

$$\nu = \frac{E}{2G} - 1 = \frac{1}{2} \frac{E}{G} - 1 = \frac{1}{2}k - 1 \quad (36)$$

The data of all biofilms for which the shear and Young's modulus could be measured simultaneously in deformation experiments was used to determine for the first time a Poisson's ratio of biofilms. Fig. 29 shows the plot of the Young's modulus versus the shear modulus. As indicated with dashed lines, the theoretical limits of Poisson's ratio are $-1 \leq \nu \leq 0.5$ for homogeneous isotropic materials. Biofilms were categorized as nearly incompressible materials due to the high water content, therefore arbitrarily setting a range of $0.3 < \nu < 0.5$. As it has been shown and discussed earlier, the measured biofilm structures show a wide variety of shear and Young's moduli even under similar cultivation conditions. The data in Fig. 29 shows this behavior. Some biofilms exhibit

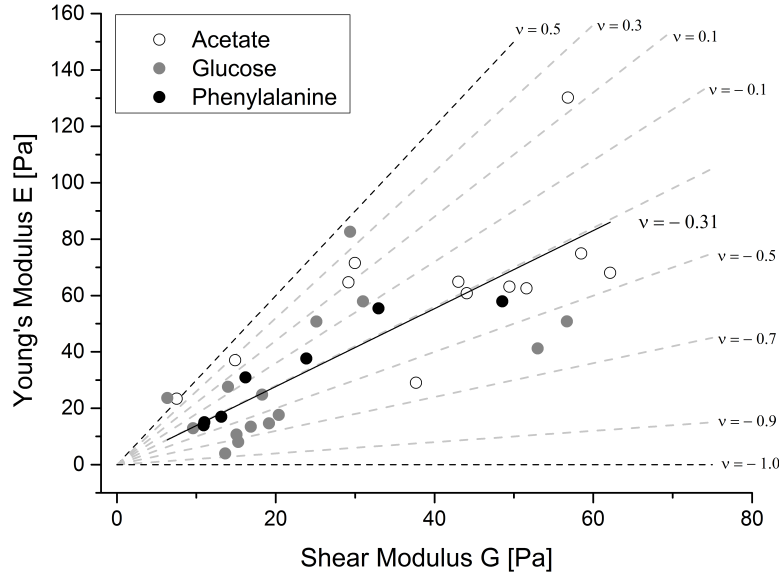


Figure 29: The slope of the linear fit (solid line) gives the Poisson's ratio $\nu = -0.31$ for biofilms in this thesis. The dashed black lines represent the theoretical limits of $-1 \leq \nu \leq 0.5$.

the expected behavior with Poisson's ratios of $0.3 < \nu < 0.5$, but the vast majority shows a different trend. Most biofilms (76%) demonstrated a negative Poisson's ratio. A linear fit revealed an average Poisson's ratio of $\nu = -0.31$ ($R^2 = 0.87$, $n = 34$). In general there is no indication that the substrate has any influence, whether the biofilm exhibits a positive or negative Poisson's ratio. A few biofilms showed an exceptional low Poisson's ratio, with a small Young's modulus compared to the shear modulus (an overview of all material properties is given in Table 9 on page 72). This occurred with larger biofilms where the front deforms as a consequence of the invoking shear stress, but almost no elongation was detected. The question arises how exact these values are. The crude assumption is that the shear stress, extracted from fluid-structure interaction simulations

(see chapter 3.4), describes the right stress conditions. This is valid for the shear stress, but might underestimate slightly the value for the Young's modulus. As the Young's modulus increases, the Poisson's ratio shifts towards positive values. However, experimental data validated the findings of this study. The idea of negative Poisson's ratios for biofilms seems to be counter-intuitive. This comes from the idea that ideal homogeneous materials should conserve volume. However, there is no law of conservation of volume. It has indeed been shown that biofilms do not conserve volume at all (Blauert *et al.*, 2015, Dreszer *et al.*, 2014b, Derlon *et al.*, 2016). The highly porous biofilm structures extrude water during deformation, rearrange EPS, or detach. This behavior of biofilms must be explained by a functional microstructure of the EPS. Many groups investigated this EPS microstructure. Confocal laser scanning microscopy (CLSM) is preferable since it is possible to visualize the different components of the biofilm matrix separately. These components, which give the biofilm its stability, are carbohydrates, proteins, or other extracellular products (as discussed in chapter 3.1). The arrangement of carbohydrate chains give the structure a general stability, supported by the cross-linking by divalent ions in the EPS. Waters *et al.* (2014) measured the internal rigidity of biofilms with oscillatory shear rheometry. They explained the importance of biofilm microstructures with the disruption of biofilms due to shear. In their experiment shear stress destroyed the connections and reduced the shear modulus by approximately two orders of magnitude. Battin *et al.* (2003) monitored the development and activity of biofilms in streamside flumes, operated under two flow regimes ($Re = 1870$ and $Re = 7560$), by combining confocal laser scanning microscopy with cryosectioning. They targeted polysaccharides and found quasihexagonal patterns as major building blocks in biofilms. This validates the assumption of a functional microstructure within the biofilm matrix. The mechanical advantages of auxetic materials compared to non-auxetic ones of the same material are versatile. It has been demonstrated with metals and foams that auxetic materials can improve mechanical properties including shear resistance, indentation resistance, fracture toughness, etc. (Alderson and Alderson, 2007, Avellaneda and Swart, 1998, Friis *et al.*, 1988, Baughman *et al.*, 1998). Prawoto (2012) summarized that the application of auxetic materials are a good choice if one of the following features is requested:

- Poisson's ratio being negative or zero
- Large shear resistance
- Hardness improvement
- Large toughness and modulus resilience
- Vibration absorption

Generally, auxetic materials need substantial porosity as it has been widely demonstrated for biofilms. Therefore, this type of material is less stiff than the solids from which they are made. The obvious advantages are the greater ability to absorb stress

and adapt due to internal structure re-arrangement. This partially explains the high factor of safety discussed before.

3.3.8 Bulk modulus K and compressibility β of biofilms

The bulk modulus K is a measure for the force is needed to elastically compress the structure. It relates the volume change of the material to the applied pressure change (eq. 14). The bulk modulus can be calculated from the shear and Young's modulus via:

$$K = \frac{E \cdot G}{3 \cdot (3G - E)} \quad (37)$$

Fig. 30 shows the bulk modulus over the Poisson's ratio. It has been shown before that biofilms behave as auxetic materials with an average Poisson's ratio of $\nu = -0.31$. The inverse of the bulk modulus is the compressibility β . Compressibility is a measure of the relative volume change of a fluid or solid as a response to a pressure or stress change.

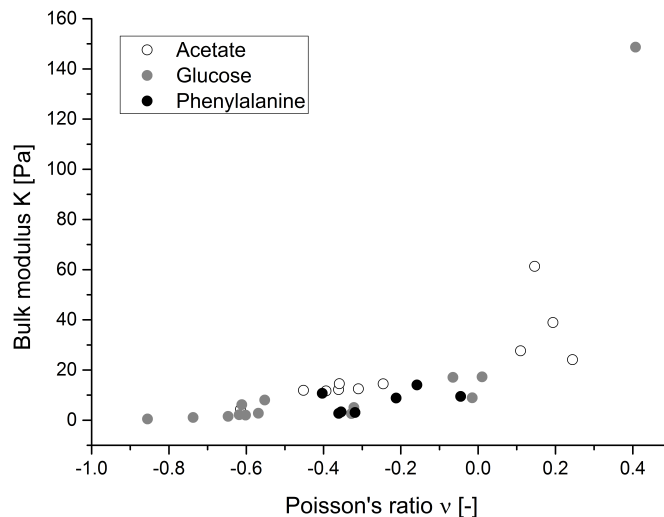


Figure 30: The bulk modulus is a measure for the isotropic pressure needed to elastically compress the biofilm structure. The bulk modulus strongly increases for Poisson's ratios > 0 . For negative Poisson's ratios the bulk modulus was $K < 20 Pa$.

Therefore, the smaller the bulk modulus, the more compressible the material. This can be seen from the trend in Fig. 30. For the lowest Poisson ratio of $\nu = -0.86$ the bulk modulus was $K = 0.25 Pa$. This corresponds to a highly deformable material. The modulus increased slightly, until $\nu = 0$ was reached. To this point the bulk modulus ranged between $K = 0 - 17 Pa$. For positive Poisson's ratios the bulk modulus increased up to $K = 150 Pa$. This resembles a more incompressible material in relation to other biofilms. The bulk modulus in the region of $\nu = -0.31$ ranged between $K = 9 - 17 Pa$. This would correlate to a compressibility of $\beta = 0.06 - 0.11 Pa^{-1}$. This is in good agreement with the data from the relaxation measurements (Fig. 26). Since the deformation is assumed to be ideally elastic, compression and relaxation should be

similar. The trend of the bulk modulus explains what has been observed experimentally. On average, biofilms are compressible materials. Since the bulk modulus K has not been evaluated for biofilms before, it is difficult to compare these values to other studies. Dreszer *et al.* (2014b) investigated young biofilms cultivated on membrane surfaces with acetate-based feed solutions. They used OCT to show that biofilms compress when the permeate flux is increased from 20 to 60 $Lm^{-2}h^{-1}$. From the OCT cross-sections they could show that the biofilm thickness decreases to 80% of the initial biofilm thickness, and stayed compacted when the pressure was increased further. This demonstrates that biofilms are compressible structures (as it has been shown before). However, they could not calculate the bulk modulus K or the compressibility β from this study. Derlon *et al.* (2016) used the term 'compressibility' qualitatively to describe changes of flux or permeability of a biofilm cultivated in a gravity-driven membrane reactor.

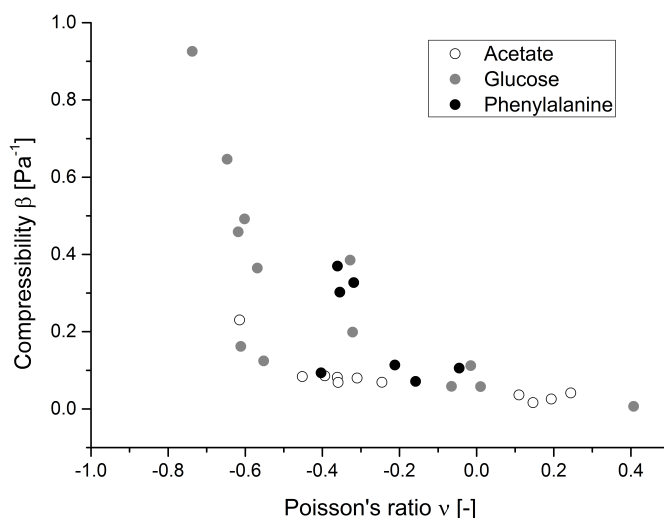


Figure 31: Compressibility of biofilms for the evaluated Poisson's ratios. Biofilms cultivated with glucose showed on average higher compressible structures compared to acetate biofilms.

Fig. 31 shows the compressibility for the biofilms in detail. Real data revealed that the compressibility of biofilms ranged between $\beta = 0.1 - 0.4 Pa^{-1}$. Biofilms cultivated with acetate showed a general lower compressibility than glucose or phenylalanine biofilms. Glucose biofilms exceed the average values and reached compressibilities of $\beta = 0.5 - 0.9 Pa^{-1}$. This value was larger than the measured biofilm relaxation. An explanation for the difference can be addressed to viscoelastic instead of elastic deformation. In viscoelastic deformation the biofilm deforms (changes volume) due to applied shear stress and does not instantly regain its original structure, when the stress is removed. This has been demonstrated in section 3.2.2. It is important to notice that these values were calculated for ideal homogeneous elastic materials in a small shear stress range. Due to heterogeneity in the biofilm matrix, the evaluated compressibility β under applied shear stress will not be valid over the whole stress range.

The consequences of these compressibilities are versatile. Well studied systems are membrane reactors. Several studies showed biofouling on membranes and spacers (West *et al.*, 2015, Dreszer *et al.*, 2014a, Fortunato *et al.*, 2016) as well as the influence on the membrane flux (Dreszer *et al.*, 2014b, Derlon *et al.*, 2016). Valladares Linares *et al.* (2015) investigated the effects in detail and showed that along with a decrease in biofilm thickness a higher hydraulic biofilm resistance was measured after the biofilm was compacted. Therefore, a membrane system, which is operated at a high or variable permeate flux, may suffer from a compacting biofilm causing higher hydraulic resistance. So knowledge about the compressibility will have practical influence on systems such as membrane reactors.

Table 9: List of the Young's modulus E , shear modulus G , bulk modulus K , compressibility β , and Poisson's ratio ν for all cultivation conditions. A '-' indicates that it was not possible to measure the shear and Young's modulus at the same time for individual biofilm patches. Therefore, values for the other material properties are missing.

Reynolds number Re [-]	Substrate	Young's modulus E [Pa]	shear modulus G [Pa]	bulk modulus K [Pa]	compressibility β [Pa ⁻¹]	Poisson's ratio ν [-]
4	Glucose	72	58 – 62	13	0.07	(-0.42) – (-0.38)
11	Acetate	29 – 68	19 – 62	4 – 15	0.07 – 0.08	(-0.61) – (0.11)
55	Acetate Glucose Phenylalanine	37 – 72 4 – 51 9 – 18	15 – 30 6 – 25 11 – 13	24 – 39 0.5 – 17 3 – 4	0.03 – 0.04 0.06 – 0.65 0.30 – 0.36	(0.19) – (0.24) (-0.86) – (0.01) (-0.36) – (-0.31)
139	Acetate Glucose Phenylalanine	23 – 45 8 – 83 55 – 58	5 – 8 15 – 53 33 – 49	– 1 – 148 11 – 14	– 0.01 – 0.92 0.07 – 0.09	– (-0.74) – (0.41) (-0.40) – (-0.16)
165	Acetate	–	30 – 88	–	–	–
277	Acetate Glucose Phenylalanine	34 51 – 58 38	9 – 37 16 – 57 16 – 24	– 8 – 17 9 – 10	– 0.06 – 0.12 0.10 – 0.11	– (-0.55) – (-0.07) (-0.21) – (-0.05)
472	Acetate Glucose Phenylalanine	65 – 130 113 –	33 – 92 133 – 158 102 – 155	15 – 61 – –	0.02 – 0.07 – –	(-0.36) – (0.11) – –

3.4 Biofilm modeling using real biofilm geometries

Biofilm modeling in combination with laboratory experiments has been proven to be a qualitative tool for scientists to better understand biofilm processes and structure. Studies improved the understanding and estimation of structural features, biofilm formation, and interaction with the environment. The structure of the biofilm has a great impact on the fluid-structure interaction and substrate conversion. Picioreanu *et al.* (2000) could show that the surface roughness of a biofilm greatly influences the mass transport into the biofilm matrix. The need for real biofilm geometries from experiments became clear, in order to improve the quality of the model approach. Early biofilm simulation studies focused on nutrient transport and species distribution in rigid biofilm structures (Kreft *et al.*, 2001, Picioreanu *et al.*, 1998). Stereomicroscopy images were used as structural templates to study the impact of surface roughness and fluid dynamics on substrate mass fluxes in biofilms (Pavissich *et al.*, 2014). Martin *et al.* (2014) used 2D OCT cross-sections as a basis for the biofilm geometry to assess membrane fluxes, covered with patchy biofilms. Li *et al.* (2016) performed similar simulations. In their study convective and diffusive transport in biofilm carriers were investigated using OCT cross-sections as geometry templates. They showed that higher substrate fluxes at a heterogeneous biofilm surface renders the whole bulk-biofilm interface to be highly active under two conditions: pure diffusion and high flow velocity along the biofilms surface. Including porosity into biofilm modeling was one step closer to modeling real structure. Fortunato *et al.* (2016) used OCT cross-sections to visualize biofouling on submerged membranes. They used the acquired imaging data to calculate the decrease in flux due to biofouling. Their theoretical study differed only by 5% to the original flux. However, all these models assume the biofilm as a non-deformable, rigid material. Fluid-structure interaction in real biofilms occur with moving structures. Therefore, biofilm mechanics needed to be included in multi-dimensional models. The scope was to have an improved description of the biofilm deformation and detachment due to flow-induced stress. In previous models biofilms were assumed as elastically deformable but quasi-static structure (Picioreanu *et al.*, 2000, Radu *et al.*, 2010, Bottero *et al.*, 2013, Martin *et al.*, 2015). This created a limitation to study detachment processes of biomass, which were of great interest since it represents potential contamination of new areas. Therefore, new methods were developed to incorporate moving structures. Several studies investigated detachment processes to improve cleaning strategies (Duddu *et al.*, 2009, Bül *et al.*, 2009, Tierra *et al.*, 2015). The influence of the biofilm shape on substrate uptake was studied with a fluid-structure interaction model by Taherzadeh *et al.* (2010). They could show that oscillation of an artificial biofilm streamer in laminar flow revealed an increased substrate uptake at the downstream tip of the structure (Taherzadeh *et al.*, 2012). First 3D models of real biofilms were implemented by Bül *et al.* (2009) and Limbert *et al.* (2013). They included confocal laser scanning microscopy images and assigned material properties to investigate the influence of the Young's modulus on deformation and de-

tachment at the microscale. A drawback of all simulations is that material properties have to be taken from the literature or be assumed, due to lack of experimental measurements. Material properties, such as the Young's modulus or the Poisson's ratio, are crucial to simulate the real biofilm deformation correctly. The evaluation of material properties from deformation experiments using OCT (section 3.2 and 3.3) rely on accurate measurement of the deformation and the right description of the stress deforming the biofilm structure. To improve the model and overcome experimental errors, a new method to combine OCT imaging and fluid-structure interaction simulations was introduced. The possibility to use structural templates from OCT data-sets and simulating the fluid flow environment around the biofilm geometry allowed to evaluate the Young's modulus from simulations and compare the estimated values to experiments in literature. This allows to non-invasively evaluate material properties from the combination of imaging and simulations, and predict biofilm deformation without the need to destroy the structure.

3.4.1 OCT images as structural templates in 2D FSI simulations

For the 2D study, OCT cross-sections of $2\text{ mm} \times 1.95\text{ mm}$ ($1024 \times 700\text{ pixels}$) were acquired, which corresponds to a resolution of $1.95\text{ }\mu\text{m}$ in the x-axis and $2.14\text{ }\mu\text{m}$ in the z-axis (in water). The images were then cropped to the area of interest without losing biofilm related information. From these pre-processed OCT images, the model geometry, which was used for numerical simulations in COMSOL Multiphysics (COMSOL 5.1, Comsol Inc, Burlington, USA), was created by tracing out manually the biofilm outline and saving the resulting black and white image as a .dxf file. Fig. 32 shows the basis for the 2D fluid-structure interaction simulations. The OCT data used is taken from the elastic deformation experiment in described in section 3.2.1. It shows the elastic deformation of the biofilm structure under no flow ($\tau = 0\text{ Pa}$) and max. shear stress ($\tau = 0.3\text{ Pa}$, compare with Fig. 9). The outlines of the un-deformed and deformed biofilm geometries were imported into the simulation software and flow field, shear stress distribution, as well as the deformation field were simulated.

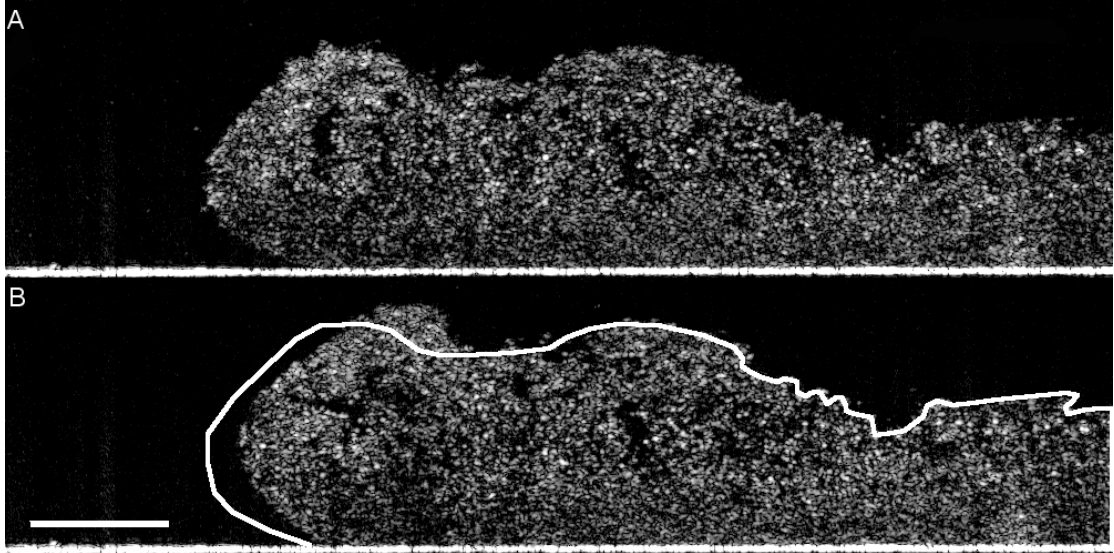


Figure 32: Basis for fluid-structure interaction simulations. OCT images of biofilm **I** were used as structural templates for the 2D simulations. **A** shows the un-deformed ($\tau = 0 \text{ Pa}$) and **B** the deformed biofilm geometry ($\tau = 0.3 \text{ Pa}$). The white outline in **B** represents the un-deformed geometry to compare. Scale bar equals $250 \mu\text{m}$.

3.4.2 Flow-field around real biofilm geometries

Fig. 33 shows the flow field of the stationary simulation at $Re = 89$ for biofilm **I**. In the simulation the inlet and outlet are treated as periodic boundary (equal flow velocity \mathbf{u}_F at Γ_{in} and Γ_{out}). This is a consequence of the assumption that more biofilm structures grew before and after the investigated biofilm. At low Reynolds numbers a laminar flow develops, which is influenced by the biofilm geometry towards the center of the channel. For simplification only the bottom biofilm geometry was extracted for the simulations. In reality biofilms form on the top as well as on the side walls (if a 3D

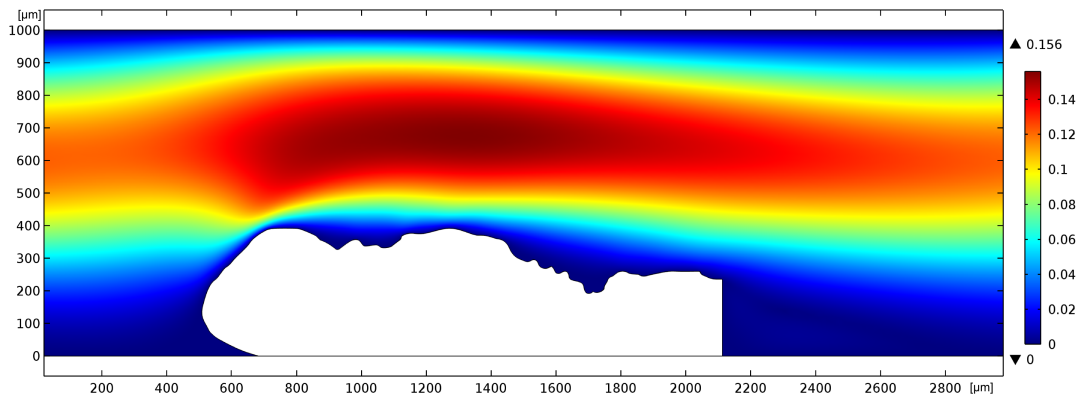


Figure 33: The figure shows the simulated stationary flow field of biofilm **I** at $Re = 89$. At low Reynolds numbers a laminar flow develops, with the highest flow velocities over the biofilm structure due to a reduced flow channel cross-section. Calibration bar in m/s .

model is considered). This reduces the cross-section of the channel further and therefore increases the flow velocity over the biofilm or introduce turbulences (in this study only laminar flow was investigated). Consequently the shear stress onto the bulk-biofilm boundary increases. This is the main reason, why simple assumptions of shear stresses such as eq. 5 do differ from real shear stresses. The highest flow velocity in Fig. 33 was above the biofilm structure and reached 0.156 m/s . Due to the small velocity no eddies developed in the channel. As the calculations presented here were based on stationary simulations, the time-dependent and stationary fluid-structure interaction simulations were compared. In time-dependent simulations flow field and deformation field are solved simultaneously, while in stationary simulations the flow field is solved first and the deformation field afterwards. In the time-dependent simulations a moving mesh was implemented, which adapted to the deformed geometry. Especially for large deformations time-dependent simulations might increase the accuracy of the simulation. Time-dependent simulations were therefore run for 2 s with a time-step of 0.005 s. It was expected from the elastic deformation experiments that full biofilm deformation would be reached within 2 s after the flow started. To allow the flow-field to establish and avoid errors with the moving mesh in the time-dependent simulation a ramp function was implemented so that the full flow velocity was reached after 0.15 s. The flow field fully developed after 0.175 s of simulation time. In the time-dependent simulation the geometry started moving as soon as the flow was enabled (0.05 s of simulation time). The geometry with the moving mesh reached the maximum deformation after 0.17 s. This was much faster than expected from the real biofilm deformation experiments. Since the geometry was treated as homogeneous material other effects, such as extrusion of water or re-arrangement of the EPS matrix components, are neglected. These effects damp the deformation, making the real process slower. The maximum flow velocity changed between the stationary to the time-dependent from 0.156 m/s to 0.158 m/s and similarly the magnitude of stress onto the biofilm structure. The fluid flow creates a viscous (shear) stress τ at the bulk-biofilm interface Γ_{FSI} as well as pressure stress (biofilm model explained in section 2.6, Fig. 7). Both stresses combined create the total stress σ (see eq. 20). The shear stress is an important parameter, since it is the basis for the assumptions in the biofilm deformation part (eq. 5). The total and shear stress were evaluated as the average stress on the biofilm boundary Γ_{FSI} (see eq. 29). The shear stress was the same in the stationary and time-lapsed simulation (both $\tau = 0.58 \text{ Pa}$), but differed slightly in the total stress. For the stationary simulation a total stress of $\sigma = 2.97 \text{ Pa}$ was calculated, while the total stress in the time-dependent simulation reached $\sigma = 3.10 \text{ Pa}$, a difference of 4%. This is a result of the pressure difference experienced by the biofilm, which is caused by the deformed geometry. As a consequence of these minor differences in the flow field and stress-distribution, further simulations were done based on stationary simulations.

3.4.3 Shear stress distribution onto and in the biofilm structure

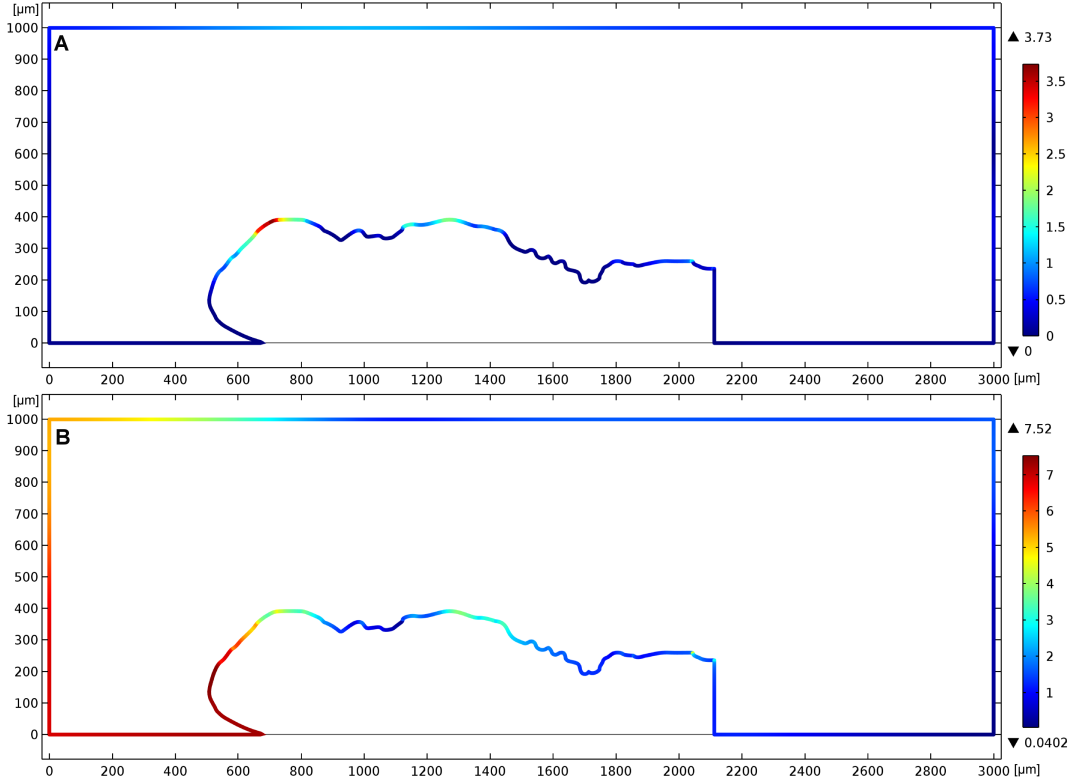


Figure 34: Simulated stress distribution along the biofilm surface for biofilm **I** at $Re = 89$. **A** shows the shear stress distribution, which is important for the experimental calculation of the shear and Young’s modulus. **B** shows the total stress distribution, including the pressure as well as the shear stress. Both calibration bars display the stress in Pa .

Fig. 34 **A** shows the shear stress distribution along the bulk-biofilm interface Γ_{FSI} at steady fluid flow of $Re = 89$. The highest shear stress was found at the upstream side of the biofilm structure. Here the fluid flow causes the highest friction up to a maximum of $\tau = 3.73 \text{ Pa}$. This is expected, since the biofilm is in contact with the highest fluid flow at that point. More interestingly there was an increased shear stress in the middle of the biofilm structure. This shows that long biofilm geometries are not only compressed from the upstream side, but experience a drag along the whole structure due to the shear forces. The total stress distribution is shown in Fig. 34 **B**. The stress in the front happens to coincide with the highest deformation in this region. The highest stress can be found at the contact point of the biofilm and substratum, which reaches $\sigma = 7.52 \text{ Pa}$. The total stress distribution is similar to the shear stress, except for the higher stress at the lower part of the upstream part of the biofilm. Integration of the stress over the whole bulk-biofilm boundary resulted in an average total stress of $\sigma = 2.97 \text{ Pa}$ and an average shear stress of $\tau = 0.58 \text{ Pa}$. The calculated shear stress from eq. 5 equals $\tau = 0.3 \text{ Pa}$. This is only 50% of the estimated shear stress and will

have an influence on the estimation of the material properties, which scale proportional to the shear stress. Even though the simulation is a simple assumption it shows the importance of the stress distribution on the biofilm structure. This can reveal the area of highest deformation as well as regions which tend to detach fast (e.g. filaments).

In section 3.2 the techniques to evaluate material properties from deformation experiments were introduced. The assumptions of the stress were based on estimations about the wall shear stress from Stoodley *et al.* (2001a). To improve the estimation of the shear stress onto the biofilm structure, the average shear stress for eight different biofilm geometries (deformed and un-deformed geometries used in the study) was evaluated for the flow velocities set during the stress-strain experiments, and compared to the calculated shear stress. These shear stresses have been used in section 3.3 to compare the influence of substrate and Reynolds number during cultivation to the mechanical properties. Fig. 35 shows the plot of the simulated shear stress versus the calculated shear stress from eq. 5. The fit for the viscous shear stress has a slope of ≈ 2

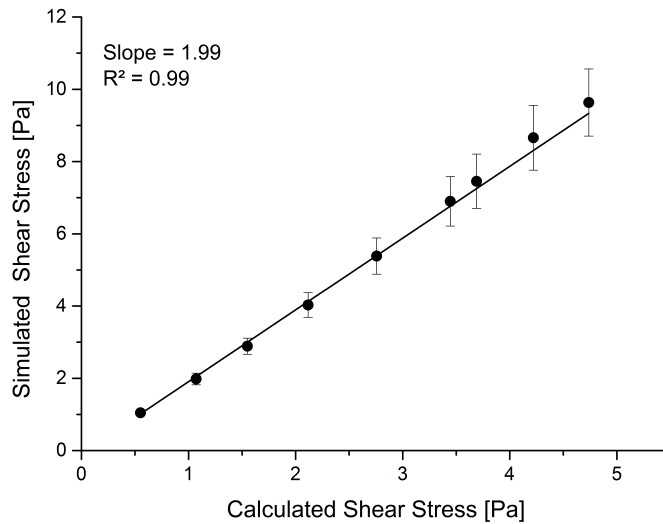


Figure 35: Relation between simulated shear stress distribution on a biofilm structure and the calculated shear stress from eq. 5. The simulated shear stress is twofold higher than the calculated shear stress.

($R^2 = 0.99, n = 8$). This directly influences the calculation of the Young's modulus, which will be twofold higher. The estimated moduli scale proportional to the higher shear stresses.

Fig. 36 shows the internal stress distribution within the biofilm domain. The von Mises stress reduces the local stress in all directions to one scalar value (see eq. 27). This makes it easier to compare the local stress to a failure criteria for which the material deforms or breaks. The simulation shows the highest stresses close to the inlet at the contact point of biofilm and substratum. This is expected from the simulation, since the highest friction and internal stress will be present at the point where the biofilm and the substratum meet. In the upstream part of the biofilm the von Mises

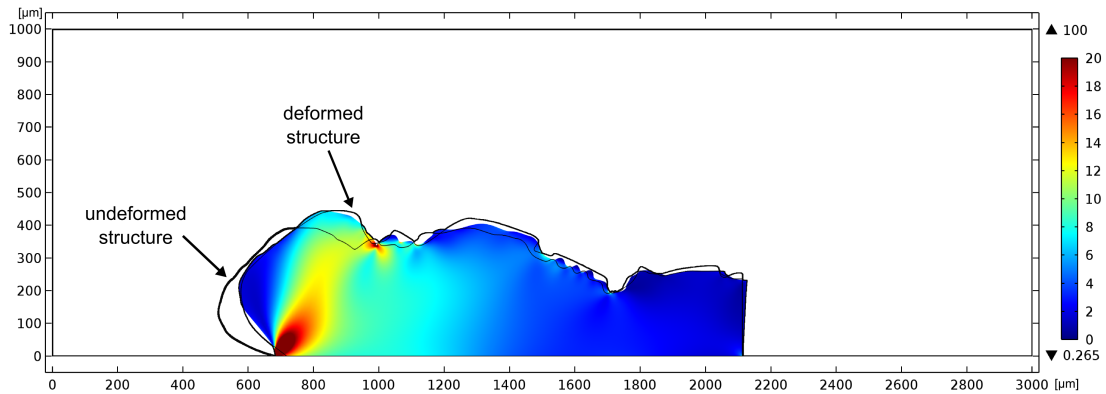


Figure 36: Von Mises stress distribution within the structure of biofilm **I** at $Re = 89$. The calibration bar display the von Mises stress in Pa .

stress is highest where the main deformation occurs. This implies that the biofilm is compressed there due to the invoking shear stress. These adjustments to the flow often result in a movement out of the OCT imaging plane, making it difficult to follow the structure movement in 2D. As a limitation of the 2D simulation, the biofilm structure overlaps at the top part as a consequence of the displacement field, which does not consider the biofilm boundary as impenetrable region. This creates an artificial high von Mises stress. Similar stress distributions were found by Taherzadeh *et al.* (2012), who simulated oscillatory biofilm streamer movements. The artificial biofilm geometry consisted of a ball acting as biofilm base and an attached tail which gets slimmer towards the end. This simplified geometry showed a similar shear stress distribution for high shear stresses at the base of the biofilm, which is exposed most to direct shear from the fluid flow. The shear stress further decreases along the tail of the streamer, indicating the phenomenological advantage of the structure in fast fluid flow. The same trend can be seen from biofilms cultivated under lower flow velocities, when no streamers develop (e.g. Fig. 34). Biofilms tend to form long and flat to decrease the overall shear stress of the fluid, while the front seems to be deformable to compensate for the stress. Böhl *et al.* (2009) used a real biofilm geometry from confocal laser scanning images for simulation of the fluid-structure interaction. This provided insight into the von Mises stress distribution too. Their experiments, similar to the results presented here, showed the highest inner stresses around the bended regions of the biofilm structure. The real biofilm geometries, such as shown in Fig. 36, give a more accurate picture of the shear

stress distribution in the upstream contact point of biofilm and substratum than artificial geometries. This contact point is the weak point of the biofilm structure from where detachment will occur.

3.4.4 Assessment of Young’s modulus from simulations

As shown in the biofilm deformation part (section 3.2), the Young’s modulus was experimentally evaluated from the linear part of a stress-strain plot. This requires a certain shape of the biofilm structure and introduces errors from manual calculation of the shear stress and strain. As mentioned in materials and methods, the basic assumption is the estimation of the stress responsible for the deformation. As Aravas and Laspidou (2008) discussed, the shear stress is not necessarily the optimal parameter to describe the stress stretching the biofilm. It might underestimate the actual stress and therefore the real Young’s modulus of the biofilm. Using a simulation model improves the shear stress assumption revealing a presumable more realistic value for the Young’s modulus. Implementing a real biofilm geometry into a simulation overcomes these restrictions and allows the determination of the Young’s modulus from geometries not suitable for image analysis. One example of these geometries is shown in Fig. 37. The biofilm geometry used for the simulations does not have a straight edge to access the shear modulus and the large structure makes it difficult to calculate the Young’s modulus from elongation.

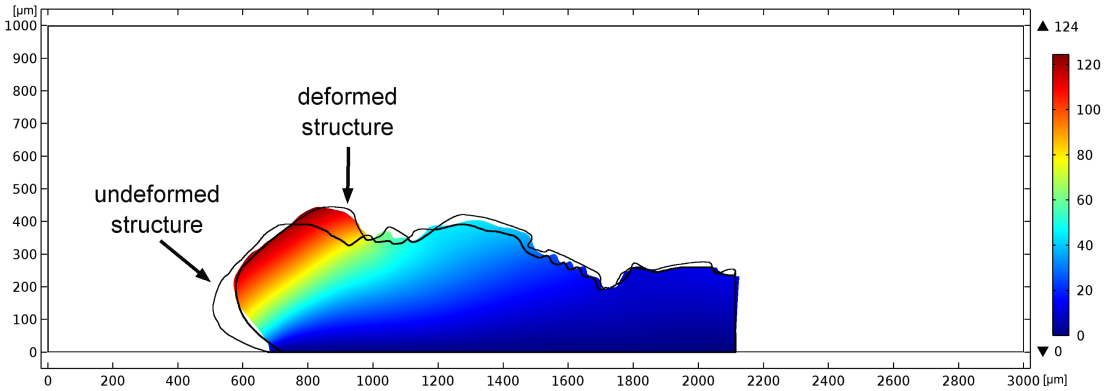


Figure 37: Final biofilm deformation at $Re = 89$. The black lines represent the experimental data before, and at full deformation. The best fit revealed a Young’s modulus of $E = 70 Pa$. Calibration bar shows the displacement field in μm .

For the simulations a Poisson’s ratio of $\nu = 0.4$ was chosen often used in literature ranging between $\nu = 0.3-0.5$ (Radu *et al.*, 2010, Zheng *et al.*, 2012, Limbert *et al.*, 2013). The evaluation of material properties was done by performing a parametric sweep of the Young’s modulus to find the best fit for the deformation to the real deformed geometry. This is different from conventional fluid-structure interaction simulations. Normally the model is set with variables and the output is the deformed geometry. Here it was possible to feed the deformed geometry (the output) and gain access to the variables.

Fig. 37 shows the displacement field of the best fit for the simulated biofilm structure at $Re = 89$. The two black lines represent the real geometries extracted from OCT cross-sections without flow ($\tau = 0 Pa$) and at full deformation ($\tau = 0.58 Pa$). Table 10 lists the differences between the simulated and real deformed geometry together for the corresponding Young's modulus. A parametric sweep from $E = 40 - 120 Pa$ resulted in a best fit for a Young's modulus of $E = 70 Pa$ with a difference of 3% from the real biofilm structure. The simulated displacement field is in good agreement with the shear

Table 10: Difference between the simulated and the real biofilm structure deformation. A Young's modulus of $70 Pa$ resulted in a best fit for the structure at $Re = 89$.

$E [Pa]$	Difference [%]
40	6.94
50	4.36
60	3.09
70	2.93
80	3.34
90	3.99
100	4.65
110	5.19
120	5.68

stress distribution, showing that the largest displacement is in the upper front region. This fits very well with the real deformed geometry. The main deformations always occurred at the front of the biofilm structure. This was the most difficult part to model correctly.

The evaluated value of $E = 70 Pa$ fits perfectly in the expected range for acetate biofilms from section 3.3. Reasons for differences between the simulated and the real deformation can be attributed to the missing information for the third dimension. During the deformation process parts of the structure bend out of the cross-section or start oscillating. This decreases the accuracy of the model. Although porosity is considered by implementing poroelasticity (including Darcy's law and a Biot assumption of fluid flow in the structure), heterogeneity of the biofilm plays another important role. During the biofilm deformation the biofilm is compressed, extruding water, and draining the biofilm. This can be measured by OCT, following the porosity during the compression over time. It has been shown that the biofilm porosity decreases up to 10% depending on the duration of the applied stress. This makes the biofilm stiffer over time. The model however considered the biofilm structure to behave like a uniform solid. Especially in biofilm structures, where bacteria tend to build clusters, heterogeneous regions develop, which make the biofilm locally stiffer or softer. It became evident that one value of the Young's modulus could not describe the deformation process well. Therefore, simula-

tions were run with the cross-sections of biofilm **IV** (see chapter 3.2.2 and Table 4) to evaluate the Young's modulus for deformations at different Reynolds numbers.

3.4.5 Scaling of the Young's modulus with fluid flow

To evaluate the stability of the system the model performance was tested for different Reynolds numbers (Re). Biofilm **IV** from section 3.2.2 was chosen to compare the simulated Young's modulus to the evaluated one from an experiment. It was tested if the evaluated Young's modulus is valid over a certain range of Reynolds numbers. Experimental techniques normally evaluate only a single value for biofilms and it is expected that this value is valid over the whole range of elastic deformation (Möhle *et al.*, 2007, Stoodley *et al.*, 1999c, Rupp *et al.*, 2005). Laspidou and Aravas (2007) predicted (based on theory) that the scale of the Young's modulus is indeed influenced by the change of porosity during deformation. A consolidation occurs (termed closing or collapsing of voids), which leads to an increase of the modulus. Their theory is quite advanced concerning the consideration of different fractions of the biofilm, e.g. active/inactive biomass, EPS, and void space. Experimental data was missing though. Deformation experiments using OCT can fill this gap and verify the model. Evaluation of the experimental Young's modulus for this study resulted in a Young's modulus of $E = 40 Pa$ ($80 Pa$ with the corrected shear stress from section 3.4.3). Above the linear region the strain increases unproportional with the shear stress until failure occurs. This relationship is covered by the Ramberg-Osgood model (Ramberg and Osgood, 1943). Lower shear stress however should result in a stable value for the Young's modulus.

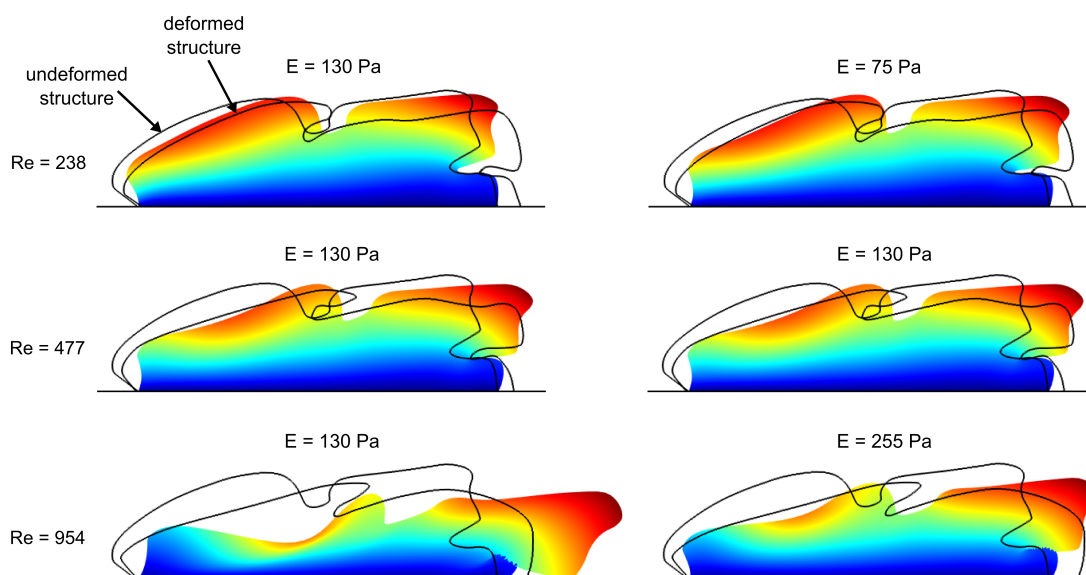


Figure 38: Simulation of biofilm **IV** with a constant Young's modulus of $E = 130 Pa$ on the left side and the best fit of Young's modulus on the right.

The simulated Young's modulus was evaluated at a Reynolds number of $Re_0 = 477$ and compared to half ($Re = 238$) and twice the Reynolds number ($Re = 954$). The best fit at Re_0 resulted in $E = 130 Pa$. The difference to the real deformation was 15%. Fig. 38 shows the difference between the simulated deformations at constant $E = 130 Pa$ (left side) and best fit (right side). Setting $E = 130 Pa$ for all fluid flows show that the linear elastic deformation does not fit all real deformations. At lower flow ($1/2Re_0$) a Young's modulus of $E = 130 Pa$ would underestimate the deformation. A Young's modulus of $E = 75 Pa$ was evaluated to fit best with the real deformation (16% difference). This is almost identical to the experiment ($E = 80 Pa$). The Young's modulus at Re_0 remained the same, while the deformation at $2Re_0$ would overestimate the deformation. Therefore, the Young's modulus had to be adjusted to $E = 255 Pa$, respectively (15% difference). That the Young's modulus increases with higher shear stress is intuitive. It has been shown that during the deformation at higher shear stresses, the porosity decreases (Blauert *et al.*, 2015). Water is extruded from the biofilm, making the structure more rigid. This behavior is a trait of heterogeneous materials. As mentioned before, the material properties depend on the porosity and are expressed ideally as a power function. This function depends on the porosity as well as a 'real' Young's modulus at zero porosity (see chapter 3.3.3). Through water exclusion the biofilm density increases, since the density of dry biomass is higher compared to water (Melo, 2005, Mueller *et al.*, 1968, Zhang and Bishop, 1994).

Table 11: Fitting the Young's modulus E for different Reynolds numbers. Instead of showing a constant value, the Young's modulus scales with the increase of the Reynolds number.

Reynolds number	Total stress	Shear stress	Young's modulus
$Re [-]$	$\sigma [Pa]$	$\tau [Pa]$	$E [Pa]$ (best fit)
238	9.07	1.72	75
477	24.40	3.47	130
954	70.23	7.51	255

To a certain extent re-arrangement of polysaccharides and polypeptides play an additional role in biofilm stiffening. Especially when the invoking shear stress is applied longer than the expected elastic relaxation time of 18 min (Shaw *et al.*, 2004), viscoelastic effects re-arrange the EPS. This limits the manual evaluation of the Young's modulus from sole imaging data for real applications. Biofilms will withstand much higher forces than anticipated. Furthermore, OCT imaging alone does not reveal mechanical heterogeneity of the biofilm. OCT might be used to reveal more dense regions inside the structure to include heterogeneity in future calculations. The findings of this study are well in accordance with Lapidou and Aravas (2007). Their theoretical model predicted this behavior of increasing Young's modulus, which has now been validated with real biofilm deformation data. The estimated change from the decrease in porosity covered a range of three times the Young's modulus at high porosities. The same scale was found in this simulation with a Young's modulus ranging between $E = 75 - 255 Pa$. Lapidou and Aravas (2007) estimations based on an iterative process over time in which the a change in strain caused a change of other material properties. Consequentially the porosity fraction changed and material properties, such as the Young's modulus, Poisson's ratio and shear modulus were evaluated for each time step. Due to the model system they showed that by keeping the volume constant (or not), the slope of the Young's modulus evolution can be changed. Another unexpected outcome of the simulation was that even though the model considered a Poisson's ratio of $\nu = 0.45$ for all fractions at the beginning (active biomass, inactive biomass, EPS) the averaged Poisson's ratio developed over time and ranged between $\nu = 0.36 - 0.44$. So the question has to be answered, which influence the Poisson's ratio has on the evaluation of the Young's modulus.

3.4.6 Influence of the Poisson's ratio ν on the evaluation of the Young's modulus

Experimental data gathered in the stress-strain experiments concluded that the investigated biofilms possess on average a negative Poisson's ratio of $\nu = -0.31$. The Poisson's ratio has direct influence on the biofilm deformation, since it relates the longitudinal and transverse strain. Materials with positive Poisson's ratio, close to 0.5, have a (nearly) constant volume and the force of shear stress is translated mainly into deformation. Materials with negative Poisson's ratios do not conserve volume. In the biofilm simulations this is expressed in an upwards movement of the geometry. Most of the shear force compresses the structure rather than deforms it. As a result the deformation field of the deformed biofilm geometry is changed. The influence of the Poisson's ratio on biofilm deformation is therefore necessary to be investigated. Fig. 39 gives a direct comparison of the positive ($\nu = 0.4$) and negative Poisson ratio ($\nu = -0.31$), both at $Re = 477$. While the deformation field of the biofilm with a positive Poisson's ratio showed movement of the whole biofilm structure the simulation with the negative Poisson's ratio displayed

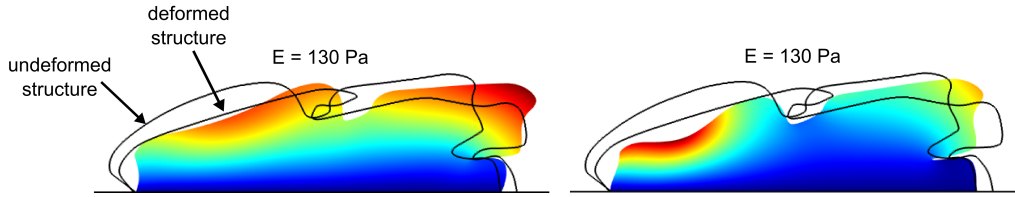


Figure 39: Influence of the negative Poisson's ratio. The image shows the difference in the deformation for a positive Poisson's ratio of $\nu = 0.4$ (left) and a negative ratio $\nu = -0.31$ (right) both at $Re = 477$ (red movement, blue no movement). For both structures the same Young's modulus of $E = 130 Pa$ was assumed.

a deformation process, which goes with a loss of volume. The simulation implicitly assumes a more rigid biofilm base, while most deformation occurs in the upstream part. The increase of biofilm density toward the bottom has been experimentally measured before (Masuda *et al.*, 1991, Zhang and Bishop, 1994), and is widely accepted in the biofilm community.

The deformation processes in which the upstream part of the biofilm deforms more than the downstream part can be observed experimentally with OCT. Fig. 40 shows an OCT cross-section of a biofilm (**VII**, cultivated with glucose) without and with flow. The deformation mainly occurs in the upstream part, while the downstream part deforms little. This is comparable to biofilm **I** (Fig. 32), which shows the main deformation in the upstream part of the biofilm.

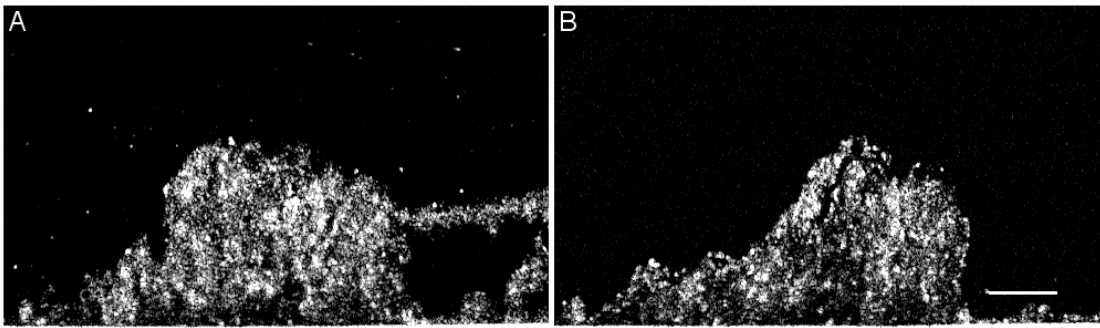


Figure 40: **A** shows the OCT cross-section of biofilm **VII** without flow and **B** with flow at $Re = 215$. Mainly the upstream part deforms as it is expected for a negative Poisson's ratio. Scale bar equals $250 \mu m$. Flow from left to right.

To test the influence of the Poisson's ratio on the evaluation of the Young's modulus, the simulations from section 3.4.5 were repeated choosing the negative Poisson's ratio $\nu = -0.31$. Fig. 41 shows the comparison of the best fit for positive Poisson's ratio to the newly evaluated values with a negative Poisson's ratio. The simulated biofilm deformation did not fit as well as before. Table 12 (page 88) gives an overview over the best fits. One possible reason is that the real biofilm did have either a positive or at least a different value of the Poisson's ratio. It has to be mentioned again that the 2D geometry is a limiting factor in the simulation. The real biofilm is able to deform

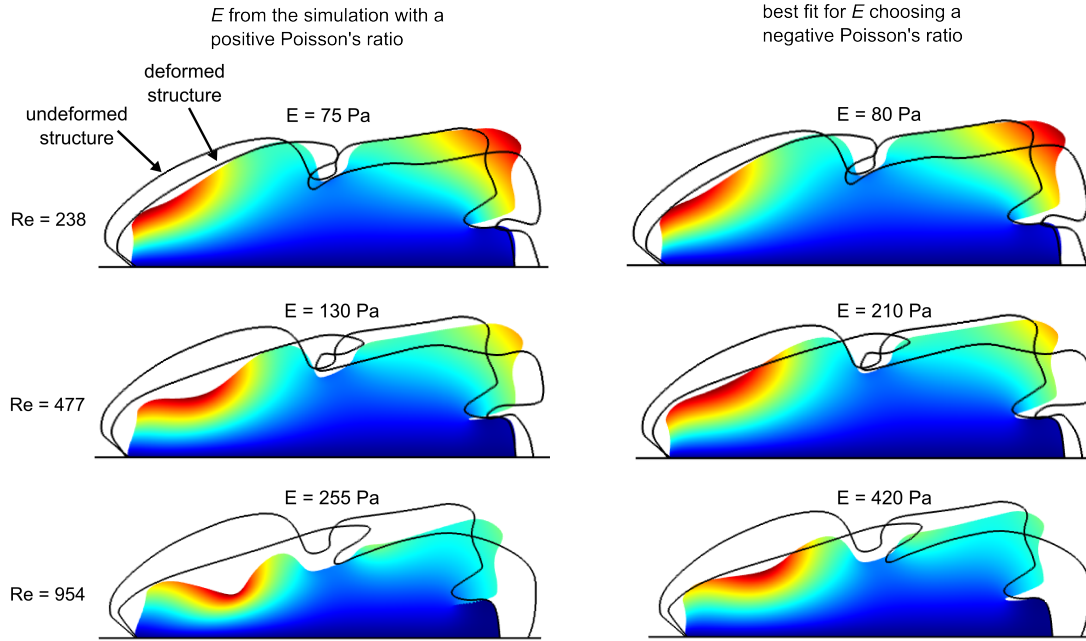


Figure 41: Influence of the negative Poisson's ratio on the evaluation of the Young's modulus. In the simulations a negative Poisson's ratio of $\nu = -0.31$ was used. Left shows the simulated deformation with the Young's moduli E evaluated earlier choosing a positive Poisson's ratio. Right shows the new best fit for E choosing a negative Poisson's ratio.

out of the image plane, which decreases the accuracy of the simulation. Generally, the Young's modulus increased using a negative Poisson's ratio. The best fits from the first simulation with a positive Poisson's ratio overestimated the deformation at increasing Reynolds numbers (left side of Fig. 41). This is in agreement with the theoretical study of Laspidou and Aravas (2007). They predicted that under real conditions the change in the Poisson's ratio results in a change of the Young's modulus. The new best fits changed the Young's modulus to $E = 80 \text{ Pa}$ at $Re = 238$, $E = 210 \text{ Pa}$ at $Re = 477$, and $E = 420 \text{ Pa}$ at $Re = 954$. For all simulations the base became more rigid and the main deformation occurred in the upstream part. As mentioned before, this represents the real biofilm deformation much better than before, but does not fit as well as a positive Poisson's ratio. The deformation in the downstream part was underestimated. This is possibly an error from the assumption of a homogeneous material. It has been shown and discussed before that the heterogeneous matrix will have different material properties locally. It is clear that the average value for the Poisson's ratio is not enough to fit the deformation well. Therefore, three biofilms, from the experiments in section 3.3.2, were chosen for which the Poisson's ratio was evaluated experimentally. The simulated deformation is shown in Fig. 42 and the values for the best fits are summarized in Table 12. The biofilms chosen were: **A** a glucose biofilm **VII** with a Poisson's ratio $\nu = 0$, **B** an acetate biofilm **VIII** with a Poisson's ratio close the mean of $\nu = -0.3$, and **C** a glucose biofilm **IX** with a low Poisson's ratio of $\nu = -0.6$. The simulations provided useful insights in the

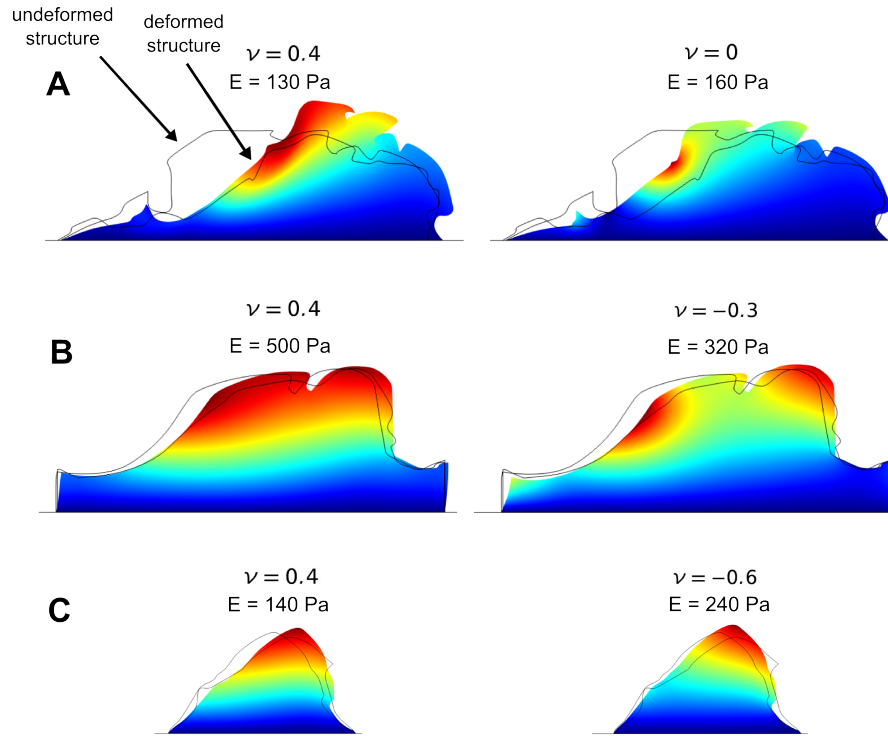


Figure 42: Comparison of the positive and negative Poisson's ratio for the simulated geometries from biofilms **VII** (A), **VIII** (B), and **IX** (C). Left side shows the best fit for the Young's modulus assuming $\nu = 0.4$. The right side shows the best fits for the Young's modulus choosing the experimentally determined Poisson's ratio.

evaluation of the Young's modulus and the sensitivity of the Poisson's ratio as a modeling parameter. The best fits for biofilm **VII** in Fig. 42 **A** showed a good approximation of the upstream part of the biofilm for a positive Poisson's ratio, but overestimated the upwards lift at the downstream part. Whereas the simulation with the experimentally determined Poisson's ratio showed a better approximation of the downstream part of the biofilm, but underestimated the upstream compression. Both simulations resulted in an equally well fit with 34%/33% difference to the real deformation. The best fits for the Young's moduli were $E = 130 Pa$ and $E = 160 Pa$, respectively. Biofilm **VIII** in Fig. 42 **B** showed a good estimation of the real deformation, independent of the Poisson's ratio chosen. Both fits result in a minimum difference of 5%/6%. The main difference between these fits was the evaluation of the Young's modulus. For the positive Poisson's ratio, a Young's modulus of $E = 500 Pa$ was evaluated, while the negative ratio resulted in $E = 320 Pa$. With regard to the Young's moduli evaluated before, it becomes obvious that the experimentally evaluated Poisson's ratio provides a value closer to the experimental data. As discussed before, the heterogeneity of the biofilm matrix will influence the deformation. Therefore, future simulations must implement local consolidation. Biofilm **IX** showed a similar trend than biofilm **VIII**. The Young's modulus for the positive Poisson's ratio was evaluated to equal $E = 140 Pa$, while the

negative ratio provided a best fit for $E = 240 Pa$. Here, the positive Poisson's ratio gives a better approximation of the deformed geometry to the real deformation. The differences of positive and negative Poisson's ratio are 7% and 13%, respectively. This indicates that the evaluation of experimentally determined material properties can be wrong. Section 3.3.7 showed that $\approx 25\%$ of the investigated biofilms showed a positive Poisson's ratio. An improvement of the simulations can be achieved by having the Young's modulus as well as the Poisson's ratio as a free parameter and sweep over both. However, this requires high computation capacity and automatization, especially when the simulations should be done in 3D.

Simulating the influence of the Poisson's ratio revealed a fascinating insight into the deformation process of biofilms. Choosing negative values resulted in a complete change of the deformation field, which is closer to real deformation processes observed with OCT. The simulation showed a higher deformation and compression at the upstream part and less deformation for the downstream part of the biofilm. This results in an implicit consolidation of the biofilm towards the bottom, in agreement with experimental results. The evaluated Young's moduli of biofilms with negative Poisson's ratio ranged between $E = 80 - 420 Pa$ and fit well in the expected range. To improve the quality further, future simulations need to include a full 3D geometry of the deformed biofilm in order to account for the third dimension, as well as local changes of the material stiffness. This might lead to a complete model to predict deformation behavior in future studies.

Table 12: Overview of the best fits for the Young's modulus, evaluated at different Reynolds numbers (Re). The minimum difference ($\%_{diff}$) between simulated and real deformation was chosen for the best fit (E_{best}) for both positive and negative Poisson's ratio (ν).

	Biofilm													
			IV				VII		VIII		IX			
Re	238		477				954		578		555		344	
ν	0.4	-0.31	0.4	-0.31	0.4	-0.31	0.4	0	0.4	-0.3	0.4	-0.6		
E_{best}	75	80	130	210	255	420	130	160	500	320	240	140		
$\%_{diff}$	16	20	15	20	15	25	34	33	5	6	7	13		

4 Summary and Outlook

Application of OCT to investigate biofilm deformation

The mechanical nature of biofilms is still one of the least investigated areas in biofilm research. Mainly because sophisticated methods were missing to measure the fragile nature of the biofilm matrix *in situ* and non-invasively. In this thesis mechanical properties of biofilms were investigated in detail using optical coherence tomography (OCT) and fluid-structure interaction simulations. OCT allowed to investigate fast dynamic processes occurring during biofilm deformation. Thereby, OCT extended the existing evaluation of mechanical properties by giving detailed information of the internal biofilm structure compared to silhouette images acquired by means of light microscopy. This allowed to measure changes during the deformation process within the biofilm matrix such as the macro-porosity.

Real-time and time-lapsed biofilm deformation visualized by means of OCT

By using OCT the understanding of the elastic deformation properties was deepened. For the first time an adaption period during elastic biofilm deformation was described. Real-time imaging of biofilm deformation processes revealed that biofilms need approximately 2 s to adapt to new shear stress conditions by either deforming or detaching. Time-lapsed shear stress experiments demonstrated the possibility to investigate biofilm deformation over a longer time.

Evaluation of mechanical properties

From the cross-sectional OCT images a full description of the elastic material properties of biofilms was derived. This included the estimation of the shear modulus G as well as Young's modulus E through image analysis. To study the influence of substrates and flow velocity on the mechanical and structural properties of biofilm, heterotrophic wastewater biofilms were cultivated in flow cells at five different Reynolds numbers at laminar flow ($Re = 11 - 472$). It was shown that mechanical properties of biofilms cultivated with sodium-acetate, D-glucose, and L-phenylalanine scaled with the Reynolds numbers during cultivation. Higher Reynolds numbers resulted in larger values for the mechanical properties. Heterogeneity in the biofilm structure produced a range of shear and Young's moduli instead of single narrow values. The shear moduli ranged between $G = 5 - 158 Pa$ and the Young's modulus between $E = 4 - 130 Pa$. These values fit well to the values found in literature. Structural heterogeneity refers to the observation that biofilms are a complex network composed of biomass, pores, and channels rather than a homogeneous material. The situation is further complicated by local density variations in the biofilm matrix. During cultivation biofilms tend to form clusters and it is common knowledge that biofilms form denser structures towards the base. A parameter, which was thought to have a significant influence on the mechanical properties, is the porosity. It was shown that a simple correlation of the shear or Young's modulus with

macro-porosity does not explain the scaling of the mechanical properties. Although it is believed that single components of the biofilm matrix are responsible for the stability (e.g. polysaccharides or polypeptides), the influence of the substrates was negligible.

Accessing the Poisson's ratio of biofilms

The systematic study of Reynolds numbers and different substrates provided the basis for a more advanced investigation of mechanical properties. In the theory of elasticity the shear and Young's modulus are related by the Poisson's ratio ν . This ratio describes the fraction of lateral to horizontal elongation during deformation. Due to the high water content, biofilms were expected to possess positive Poisson's ratios close to incompressible materials such as rubber. However, OCT images revealed a compressible nature of biofilms leading to the conclusion that most of the investigated biofilms behave as auxetic materials with an average negative Poisson's ratio of $\nu = -0.31$. This can change the mechanical view on biofilms and explains the high resistance against shear stresses.

Bulk modulus and compressibility of biofilms

Another material property, which is related to the shear modulus G , Young's modulus E , and Poisson's ratio ν , is the bulk modulus K . The bulk modulus defines the resistance towards stress to conserve volume. The inverse of the bulk modulus is the compressibility β . Most biofilms investigated showed negative Poisson's ratios and were therefore highly compressible. Moreover, biofilms with positive Poisson's ratios conserved volume at higher stresses more than biofilms with negative Poisson's ratios. For biofilms with Poisson's ratios $\nu > 0$ the bulk modulus reached values up to $K = 150 Pa$, while for biofilms with a Poisson's ratio $\nu \leq 0$ the bulk modulus ranged between $K = 0 - 17 Pa$. The comprehensive understanding of compressibility will have an influence on applications such as membrane reactors, since a consolidation of biofilms forming on a membrane will reduce flux and disturb the process of filtration.

OCT cross-sections as structural templates for FSI simulations

The acquired cross-sectional OCT images were further used as structural templates in fluid-structure interaction simulations. Implementation of real geometries was a necessary step towards a better understanding of biofilm mechanics. Real geometries allowed to correct assumptions about the shear stress. In turn, the values of the Young's modulus E , derived initially from image analysis of OCT data-sets, were further refined. Before, most simulations assumed the biofilm as a non-moving structure. Implementation of real deformed and un-deformed biofilm geometries from OCT images allowed to fit the simulated deformation to the real deformed geometry by varying the Young's modulus. The evaluated Young's moduli from simulations proved to be in similar range than the estimated ones from image analysis ($E = 70 - 500 Pa$). It was demonstrated in the simulations that the Young's modulus cannot be considered constant over a large range

of shear stresses. Biofilms have been demonstrated to be macro-porous, deformable structures which consolidate during the deformation process. Therefore, the Young's modulus must increase and cannot be assumed constant.

Influence of Poisson's ratio on FSI simulations

Furthermore, the influence of a negative Poisson's ratio on the biofilm deformation was investigated. Comparing simulated and real deformed biofilm structures showed that the value of the Poisson's ratio does not improve the accuracy of the simulation. However, simulations with a negative Poisson's ratio showed a better agreement of the volume loss visualized in the experiments by optical coherence tomography compared to simulations with a positive Poisson's ratio. Choosing a negative Poisson's ratio an implicit consolidation of the biofilm base was observed in the simulations. Furthermore, the simulations confirmed a larger deformation of the upstream part of the biofilm, which has also been observed in deformation experiments monitored by means of OCT.

A trait of the negative Poisson's ratio is that the biofilm structure does not lift up and elongate as much as the simulations with positive Poisson's ratios revealed. This is in agreement with the experimental observations made by OCT. The simulations with negative Poisson's ratios extended the knowledge about biofilm mechanics validating the need to consider biofilms as auxetic materials.

Outlook

The methods developed and presented in this work were used to investigate biofilm mechanics in detail. The results extended the knowledge of biofilm mechanics. This includes the classification of biofilms as auxetic materials and evaluation of their Poisson's ratio, bulk modulus, and compressibility. More studies of a variety of different biofilms will be needed in future to understand the complex interaction of biofilm matrix and fluid flow. In this thesis the importance of a structured network within the biofilm matrix has been emphasized. More experiments are needed in order to understand the interaction of polysaccharides, polypeptides, and other EPS components. Till now it is not completely clear which component is the major factor to provide a great stability. This is especially important to understand the transition process from elastic into viscoelastic deformation. OCT provides a system to monitor creep of biofilms in 3D over a long period. This will help to understand more about biofilm mechanics and possibly reveal new mechanical properties. However, image analysis introduced systematic errors, which were corrected by implementation of real deformed geometries into fluid-structure interaction simulation. Even though the simulations presented in this work helped to understand and validate the mechanical nature of biofilms, 2D simulations ran into limitations. Movements out of the cross-sectional image plane during image acquisition as well as the description of the stress-distribution on the 2D geometry were the major factors responsible for mismatches between simulated and imaged deformation. Extension of the model handling 3D data-sets would further improve the estimation

of mechanical properties. However, this is a difficult task and sophisticated methods need to be developed. Dealing with large data-sets will require to find the trait between structural details and smoothing. Additionally, a more detailed analysis would be possible by assigning different density zones to the biofilm structure. Until now biofilms were considered as homogeneous material in most FSI simulation studies. In reality biofilms consist of more and less dense zones, which might possess a variety of local mechanical properties. It has been shown that the biofilm stiffness increases towards the substratum, therefore including a density gradient might improve further deformation simulations. OCT is capable to identify density differences within the biofilm structure by indicating these areas with a stronger (brighter) signal. This has not yet been described in detail in biofilm research and might take a while before sophisticated methods are developed. However, this feature has potential to be included in future studies to improve the simulations even further.

The combination of optical coherence tomography and fluid-structure interaction simulations proved to be a useful to investigate biofilm mechanics and possesses a great potential for future research.

5 References

- Abdallah, M., Khelissa, O., Ibrahim, A., Benoliel, C., Heliot, L., Dhulster, P., and Chihib, N. E. Impact of growth temperature and surface type on the resistance of *Pseudomonas aeruginosa* and *Staphylococcus aureus* biofilms to disinfectants. *Int. J. Food Microbiol.*, 214:38–47, 2015.
- Aggarwal, S., Stewart, P. S., and Hozalski, R. M. Biofilm Cohesive Strength as a Basis for Biofilm Recalcitrance: Are Bacterial Biofilms Overdesigned? *Microbiol. insights*, 8(Suppl 2):29–32, 2015.
- Al-Fattani, M. A. and Douglas, L. J. Biofilm matrix of *Candida albicans* and *Candida tropicalis*: Chemical composition and role in drug resistance. *J. Med. Microbiol.*, 55(8):999–1008, 2006.
- Alderson, A. and Alderson, K. L. Auxetic materials. *Proc. Inst. Mech. Eng. Part G J. Aerosp. Eng.*, 221(4):565–575, 2007.
- Alpkvist, E. and Klapper, I. Description of mechanical response including detachment using a novel particle model of biofilm/flow interaction. *Water Sci. Technol.*, 55(8-9):265, 2007.
- Alpkvist, E. and Klapper, I. A multidimensional multispecies continuum model for heterogeneous biofilm development. *Bull. Math. Biol.*, 69(2):765–789, 2007.
- Alsteens, D., Dupres, V., Mc Evoy, K., Wildling, L., Gruber, H. J., and Dufrêne, Y. F. Structure, cell wall elasticity and polysaccharide properties of living yeast cells, as probed by AFM. *Nanotechnology*, 19(38):384005, 2008.
- Aravas, N. and Laspidou, C. S. On the calculation of the elastic modulus of a biofilm streamer. *Biotechnol. Bioeng.*, 101(1):196–200, 2008.
- Avellaneda, M. and Swart, P. J. Calculating the performance of 13 piezoelectric composites for hydrophone applications: An effective medium approach. *J. Acoust. Soc. Am.*, 103(3):1449–1467, 1998.
- Baniasadi, M., Xu, Z., Gandee, L., Du, Y., Lu, H., Zimmern, P., and Minary-Jolandan, M. Nanoindentation of *Pseudomonas aeruginosa* bacterial biofilm using atomic force microscopy. *Mater. Res. Express*, 1(4):045411, 2014.
- Banks, H. T., Hu, S., and Kenz, Z. R. A brief review of elasticity and viscoelasticity for solids. *Adv. Appl. Math. Mech.*, 3(1):1–51, 2011.
- Battin, T. J., Kaplan, L. a., Newbold, J. D., Cheng, X., and Hansen, C. Effects of Current Velocity on the Nascent Architecture of Stream Microbial Biofilms Effects of Current Velocity on the Nascent Architecture of Stream Microbial Biofilms. *Appl. Environ. Microbiol.*, 69(9):5443–5452, 2003.
- Baughman, R. H., Shacklette, J. M., Zakhidov, A. A., and Stafstöröm, S. Negative Poisson’s ratios as a common feature of cubic metals. *Nature*, 392:362–365, 1998.
- Beech, I. B., Smith, J. R., Steele, A. A., Penegar, I., and Campbell, S. A. The use of atomic force microscopy for studying interactions of bacterial biofilms with surfaces. *Colloids Surfaces B Biointerfaces*, 23(2-3):231–247, 2002.

- Beyenal, H. and Lewandowski, Z. Internal and External Mass Transfer in Biofilms Grown at Various Flow Velocities. *Biotechnol. Prog.*, 18(1):55–61, 2002.
- Beyenal, H., Lewandowski, Z., and Harkin, G. Quantifying biofilm structure: facts and fiction. *Biofouling*, 20(1):1–23, 2004.
- Bishop, P. L., Zhang, T. C., and Fu, Y. C. Effects of biofilm structure, microbial distributions and mass transport on biodegradation processes. *Water Sci. Technol.*, 31(1):143–152, 1995.
- Blauert, F., Horn, H., and Wagner, M. Time-resolved biofilm deformation measurements using optical coherence tomography. *Biotechnol. Bioeng.*, 112(9):1893–1905, 2015.
- Böl, M., Möhle, R. B., Haesner, M., Neu, T. R., Horn, H., and Krull, R. 3D finite element model of biofilm detachment using real biofilm structures from CLSM data. *Biotechnol. Bioeng.*, 103(1):177–86, 2009.
- Böl, M., Ehret, A. E., Bolea Albero, A., Hellriegel, J., and Krull, R. Recent advances in mechanical characterisation of biofilm and their significance for material modelling. *Crit. Rev. Biotechnol.*, 33(2):145–71, 2013.
- Bottero, S., Storck, T., Heimovaara, T. J., van Loosdrecht, M. C. M., Enzien, M. V., and Picioreanu, C. Biofilm development and the dynamics of preferential flow paths in porous media. *Biofouling*, 29(9):1069–86, 2013.
- Brito, A. G. and Melo, L. F. Mass transfer coefficients within anaerobic biofilms: Effects of external liquid velocity. *Water Res.*, 33(17):3673–3678, 1999.
- Broecker, E. H. and Dunbar, M. T. Optical coherence tomography: its clinical use for the diagnosis, pathogenesis, and management of macular conditions. *Optometry*, 76(2):79–101, 2005.
- Cabrera, S., Katz, A., and Margalit, E. Vitreopapillary traction: Cost-effective diagnosis by optical coherence tomography. *Can. J. Ophthalmol. / J. Can. d’Ophtalmologie*, 41(6):763–765, 2006.
- Cense, A. W., Peeters, E. A. G., Gottenbos, B., Baaijens, F. P. T., Nuijs, A. M., and van Dongen, M. E. H. Mechanical properties and failure of *Streptococcus mutans* biofilms, studied using a microindentation device. *J. Microbiol. Methods*, 67(3):463–472, 2006.
- Charlebois, A., Jacques, M., Boulianne, M., and Archambault, M. Tolerance of *Clostridium perfringens* biofilms to disinfectants commonly used in the food industry. *Food Microbiol.*, 62:32–38, 2017.
- Chen, Y., Van Der Mei, H. C., Busscher, H. J., and Norde, W. Viscous nature of the bond between adhering bacteria and substratum surfaces probed by atomic force microscopy. *Langmuir*, 30(11):3165–3169, 2014.
- Costerton, J. W., Lewandowski, Z., Caldwell, D. E., Korber, D. R., and Lappin-Scott, H. M. Microbial biofilms. *Annu. Rev. Microbiol.*, 49:711–45, 1995.
- Coussy, O. *Poromechanics*. John Wiley & Sons, Ltd, Chichester, UK, 2003.
- De Beer, D. and Stoodley, P. Relation between the structure of an aerobic biofilm and transport phenomena. *Water Sci. Technol.*, 32(8):11–18, 1995.

- de Beer, D., Stoodley, P., Roe, F., and Lewandowski, Z. Effects of biofilm structures on oxygen distribution and mass transport. *Biotechnol. Bioeng.*, 43(11):1131–8, 1994.
- Derlon, N., Grütter, A., Brandenberger, F., Sutter, A., Kuhlicke, U., Neu, T. R., and Morgenroth, E. The composition and compression of biofilms developed on ultrafiltration membranes determine hydraulic biofilm resistance. *Water Res.*, 102(September): 63–72, 2016.
- Douarche, C., Allain, J. M., and Raspaud, E. Bacillus subtilis Bacteria Generate an Internal Mechanical Force within a Biofilm. *Biophys. J.*, 109(10):2195–2202, 2015.
- Dreszer, C., Vrouwenvelder, J. S., Paulitsch-Fuchs, A. H., Zwijnenburg, A., Kruithof, J. C., and Flemming, H. C. Hydraulic resistance of biofilms. *J. Memb. Sci.*, 429: 436–447, 2013.
- Dreszer, C., Flemming, H.-C., Wexler, A., Zwijnenburg, A., Kruithof, J., and Vrouwenvelder, J. Development and testing of a transparent membrane biofouling monitor. *Desalin. Water Treat.*, 52(10-12):1807–1819, 2014.
- Dreszer, C., Wexler, A., Drusová, S., Overdijk, T., Zwijnenburg, A., Flemming, H.-C., Kruithof, J., and Vrouwenvelder, J. In-situ biofilm characterization in membrane systems using Optical Coherence Tomography: Formation, structure, detachment and impact of flux change. *Water Res.*, 67:243–254, 2014.
- Drexler, W. and Fujimoto, J. G., editors. *Optical Coherence Tomography*. Springer International Publishing, Cham, 2015.
- Duddu, R., Chopp, D. L., and Moran, B. A two-dimensional continuum model of biofilm growth incorporating fluid flow and shear stress based detachment. *Biotechnol. Bioeng.*, 103(1):92–104, 2009.
- Dunsmore, B. C., Jacobsen, A., Hall-Stoodley, L., Bass, C. J., Lappin-Scott, H. M., and Stoodley, P. The influence of fluid shear on the structure and material properties of sulphate-reducing bacterial biofilms. *J. Ind. Microbiol. Biotechnol.*, 29(6):347–353, 2002.
- Ertesvåg, H. and Valla, S. Biosynthesis and applications of alginates. *Polym. Degrad. Stab.*, 59(1-3):85–91, 1998.
- Evans, K. E. Auxetic polymers: a new range of materials. *Endeavour*, 15:170–174, 1991.
- Fercher, A. F., Drexler, W., Hitzenberger, C. K., and Lasser, T. Optical coherence tomography development, principles, applications. *Z. Med. Phys.*, 20(4):251–276, 2010.
- Findley, W. N., Lai, J. S., and Onaran, K., editors. *Creep and Relaxation of Nonlinear Viscoelastic Materials*. Dover Publishing, Minneola, NY, 1989.
- Flemming, H.-C. and Wingender, J. The biofilm matrix. *Nat. Rev. Microbiol.*, 8(9): 623–33, 2010.
- Fortunato, L., Qamar, A., Wang, Y., Jeong, S., and Leiknes, T. In-situ assessment of biofilm formation in submerged membrane system using optical coherence tomography and computational fluid dynamics. *J. Memb. Sci.*, 521:84–94, 2016.

- Friis, E. A., Lakes, R. S., and Park, J. B. Negative Poisson's ratio polymeric and metallic foams. *J. Mater. Sci.*, 23(12):4406–4414, 1988.
- Gelikonov, V. M. and Gelikonov, G. V. New approach to cross-polarized optical coherence tomography based on orthogonal arbitrarily polarized modes. *Laser Phys. Lett.*, 3(9):445–451, 2006.
- Gonzalez, D., Tjandraatmadja, G., Barry, K., Vanderzalm, J., Kaksonen, A. H., Dillon, P., Puzon, G. J., Sidhu, J., Wylie, J., Goodman, N., and Low, J. Biofouling potential and material reactivity in a simulated water distribution network supplied with stormwater recycled via managed aquifer recharge. *Water Res.*, 105:110–118, 2016.
- Greaves, G. N., Greer, A. L., Lakes, R. S., and Rouxel, T. Poisson's ratio and modern materials. *Nat. Mater.*, 10(11):823–837, 2011.
- Guélon, T., Mathias, J.-D., and Stoodley, P. Advances in Biofilm Mechanics. In Fleming, H.-C., Wingender, J., and Szewzyk, U., editors, *Biofilm Highlights*, volume 5 of *Springer Series on Biofilms*, chapter Advances i, pages 111–139. Springer-Verlag, Berlin, Heidelberg, 2011.
- Haisch, C. and Niessner, R. Visualisation of transient processes in biofilms by optical coherence tomography. *Water Res.*, 41(11):2467–2472, 2007.
- Harapanahalli, A. K., Younes, J. A., Allan, E., van der Mei, H. C., and Busscher, H. J. Chemical Signals and Mechanosensing in Bacterial Responses to Their Environment. *PLoS Pathog.*, 11(8):1–6, 2015.
- Hawser, S. P., Baillie, G. S., and Douglas, L. J. Production of extracellular matrix by *Candida albicans* biofilms. *J Med Microbiol.*, 47(June 1997):253–256., 1998.
- He, Y., Peterson, B. W., Jongsma, M. A., Ren, Y., Sharma, P. K., Busscher, H. J., and van der Mei, H. C. Stress relaxation analysis facilitates a quantitative approach towards antimicrobial penetration into biofilms. *PLoS One*, 8(5):e63750, 2013.
- Hohne, D. N., Younger, J. G., and Solomon, M. J. Flexible microfluidic device for mechanical property characterization of soft viscoelastic solids such as bacterial biofilms. *Langmuir*, 25(13):7743–7751, 2009.
- Hollenbeck, E. C., Douarche, C., Allain, J.-M., Roger, P., Regeard, C., Cegelski, L., Fuller, G. G., and Raspaud, E. Mechanical Behavior of a *Bacillus subtilis* Pellicle. *J. Phys. Chem. B*, 120(26):6080–6088, 2016.
- Holmberg, A. and Rasmussen, M. Mature biofilms of *Enterococcus faecalis* and *Enterococcus faecium* are highly resistant to antibiotics. *Diagn. Microbiol. Infect. Dis.*, 84(1):19–21, 2016.
- Horn, H. and Lackner, S. Modeling of Biofilm Systems: A Review. *Adv. Biochem. Eng. Biotechnol.*, 123(July 2015):53–76, 2014.
- Houari, a., Picard, J., Habarou, H., Galas, L., Vaudry, H., Heim, V., and Di Martino, P. Rheology of biofilms formed at the surface of NF membranes in a drinking water production unit. *Biofouling*, 24(4):235–40, 2008.
- Hu, Z., Luo, H., Du, Y., and Lu, H. Fluorescent stereo microscopy for 3D surface profilometry and deformation mapping. *Opt. Express*, 21(10):11808–18, 2013.

- Huang, D., Swanson, E., Lin, C., Schuman, J., Stinson, W., Chang, W., Hee, M., Flotte, T., Gregory, K., Puliafito, C., and Et, A. Optical coherence tomography. *Science (80-.)*, 254(5035):1178–1181, 1991.
- Jayawarna, V., Smith, A., Gough, J. E., and Ulijn, R. V. Three-dimensional cell culture of chondrocytes on modified di-phenylalanine scaffolds. *Biochem. Soc. Trans.*, 35(Pt 3):535–7, 2007.
- JPK. Determining the elastic modulus of biological samples using atomic force microscopy. Technical report, JPK Instruments, 2008.
- Kitchens, J. W., Flynn, H. W., Moshfeghi, A. A., and Puliafito, C. A. Idiopathic macular hole with extensive subretinal fluid: Clinical and optical coherence tomography features before and after surgery. *Am. J. Ophthalmol.*, 139(2):383–386, 2005.
- Klapper, I., Rupp, C. J., Cargo, R., Purvedorj, B., and Stoodley, P. Viscoelastic fluid description of bacterial biofilm material properties. *Biotechnol. Bioeng.*, 80(3):289–96, 2002.
- Knudsen, F. P. Dependence of Mechanical Strength of Brittle Polycrystalline Specimens on Porosity and Grain Size. *J. Am. Ceram. Soc.*, 42(8):376–387, 1959.
- Körstgens, V., Flemming, H. C., Wingender, J., and Borchard, W. Influence of calcium ions on the mechanical properties of a model biofilm of mucoid *Pseudomonas aeruginosa*. *Water Sci. Technol.*, 43(6):49–57, 2001.
- Körstgens, V., Flemming, H.-C., Wingender, J., and Borchard, W. Uniaxial compression measurement device for investigation of the mechanical stability of biofilms. *J. Microbiol. Methods*, 46(1):9–17, 2001.
- Kreft, J. U., Picioreanu, C., Wimpenny, J. W., and van Loosdrecht, M. C. Individual-based modelling of biofilms. *Microbiology*, 147(Pt 11):2897–2912, 2001.
- Laspidou, C. S. and Aravas, N. Variation in the mechanical properties of a porous multi-phase biofilm under compression due to void closure. *Water Sci. Technol.*, 55(8-9):447–453, 2007.
- Laspidou, C. S. and Rittmann, B. E. Evaluating trends in biofilm density using the UMCCA model. *Water Res.*, 38(14-15):3362–3372, 2004.
- Lau, P. C. Y., Dutcher, J. R., Beveridge, T. J., and Lam, J. S. Absolute quantitation of bacterial biofilm adhesion and viscoelasticity by microbead force spectroscopy. *Biophys. J.*, 96(7):2935–2948, 2009.
- Lembre, P., Lorentz, C., and Di, P. Exopolysaccharides of the Biofilm Matrix: A Complex Biophysical World. In *The Complex World of Polysaccharides*, pages 371–392. InTech, 2012.
- Lewandowski, Z. Notes on biofilm porosity. *Water Res.*, 34(9):2620–2624, 2000.
- Li, C., Felz, S., Wagner, M., Lackner, S., and Horn, H. Investigating biofilm structure developing on carriers from lab-scale moving bed biofilm reactors based on light microscopy and optical coherence tomography. *Bioresour. Technol.*, 200:128–136, 2016.

- Li, Y.-H. and Tian, X. Quorum sensing and bacterial social interactions in biofilms. *Sensors (Basel)*, 12(3):2519–38, 2012.
- Limbert, G., Bryan, R., Cotton, R., Young, P., Hall-Stoodley, L., Kathju, S., and Stoodley, P. On the mechanics of bacterial biofilms on non-dissolvable surgical sutures: A laser scanning confocal microscopy-based finite element study. *Acta Biomater.*, 9(5):6641–6652, 2013.
- Lubliner, J. and Papadopoulos, P. *Introduction to Solid Mechanics*. Springer International Publishing, Cham, 2017.
- Martin, K. J., Bolster, D., Derlon, N., Morgenroth, E., and Nerenberg, R. Effect of fouling layer spatial distribution on permeate flux: A theoretical and experimental study. *J. Memb. Sci.*, 471:130–137, 2014.
- Martin, K. J., Picioreanu, C., and Nerenberg, R. Assessing microbial competition in a hydrogen-based membrane biofilm reactor (MBfR) using multidimensional modeling. *Biotechnol. Bioeng.*, 112(9):1843–1853, 2015.
- Masuda, S., Watanabe, Y., and Ishiguro, M. Biofilm Properties and Simultaneous Nitrification and Denitrification in Aerobic Rotating Biological Contactors. *Wat. Sci. Tech.*, 23:1355–1363, 1991.
- Mathias, J. D. and Stoodley, P. Applying the digital image correlation method to estimate the mechanical properties of bacterial biofilms subjected to a wall shear stress. *Biofouling*, 25(8):695–703, 2009.
- Mayer, C., Moritz, R., and Kirschner, C. The role of intermolecular interactions: studies on model systems for bacterial biofilms. *Int. J. Biol. Macromol.*, 26:3–16, 1999.
- Melo, L. F. Biofilm physical structure, internal diffusivity and tortuosity. *Water Sci. Technol.*, 52(7):77–84, 2005.
- Möhle, R. B., Langemann, T., Haesner, M., Augustin, W., Scholl, S., Neu, T. R., Hempel, D. C., and Horn, H. Structure and shear strength of microbial biofilms as determined with confocal laser scanning microscopy and fluid dynamic gauging using a novel rotating disc biofilm reactor. *Biotechnol. Bioeng.*, 98(4):747–55, 2007.
- Moreira, J. M. R., Gomes, L. C., Simões, M., Melo, L. F., and Mergulhão, F. J. The impact of material properties, nutrient load and shear stress on biofouling in food industries. *Food Bioprod. Process.*, 95:228–236, 2015.
- Moreira, J. M. R., Fulgêncio, R., Alves, P., Machado, I., Bialuch, I., Melo, L. F., Simões, M., and Mergulhão, F. J. Evaluation of SICAN performance for biofouling mitigation in the food industry. *Food Control*, 62:201–207, 2016.
- Morgenroth, E. and Milferstedt, K. Biofilm engineering: linking biofilm development at different length and time scales. *Rev. Environ. Sci. Bio/Technology*, 8(3):203–208, 2009.
- Moskvicheva, E., Sidyakin, P., and Shitov, D. Method of Corrosion Prevention in Steel Pressure Pipelines in Sewerage Systems. *Procedia Eng.*, 150(442):2381–2386, 2016.
- Mueller, J. A., Boyle, W. C., and Lightfoot, E. N. Oxygen diffusion through zoogloeal flocs. *Biotechnol. Bioeng.*, 10(3):331–358, 1968.

- Murga, R., Stewart, P. S., and Daly, D. Quantitative analysis of biofilm thickness variability. *Biotechnol. Bioeng.*, 45(6):503–10, 1995.
- Noguera, D., Pizarro, G., Stahl, D., and Rittmann, B. Simulation of multispecies biofilm development in three dimensions. *Water Sci. Technol.*, 39(7):123–130, 1999.
- Ochoa, J.-C., Coufort, C., Escudié, R., Liné, A., and Paul, E. Influence of non-uniform distribution of shear stress on aerobic biofilms. *Chem. Eng. Sci.*, 62(14):3672–3684, 2007.
- Otsu, N. A Threshold Selection Method from Gray-Level Histograms. *IEEE Trans. Syst. Man. Cybern.*, 9(1):62–66, 1979.
- Panda, J. J., Mishra, A., Basu, A., and Chauhan, V. S. Stimuli responsive self-assembled hydrogel of a low Molecular weight free dipeptide with potential for tunable drug delivery. *Biomacromolecules*, 9(8):2244–2250, 2008.
- Paramonova, E., Krom, B. P., van der Mei, H. C., Busscher, H. J., and Sharma, P. K. Hyphal content determines the compression strength of *Candida albicans* biofilms. *Microbiology*, 155(6):1997–2003, 2009.
- Pavissich, J. P., Aybar, M., Martin, K. J., and Nerenberg, R. A methodology to assess the effects of biofilm roughness on substrate fluxes using image analysis, substrate profiling, and mathematical modelling. *Water Sci. Technol.*, 69(9):1932–1941, 2014.
- Pelling, A. E., Li, Y., Shi, W., and Gimzewski, J. K. Nanoscale visualization and characterization of *Myxococcus xanthus* cells with atomic force microscopy. *Proc. Natl. Acad. Sci. U. S. A.*, 102(18):6484–6489, 2005.
- Peterson, B. W., van der Mei, H. C., Sjollem, J., Busscher, H. J., and Sharma, P. K. A distinguishable role of eDNA in the viscoelastic relaxation of biofilms. *MBio*, 4(5):1–7, 2013.
- Peterson, B. W., He, Y., Ren, Y., Zerdoum, A., Libera, M. R., Sharma, P. K., van Winkelhoff, A. J., Neut, D., Stoodley, P., van der Mei, H. C., and Busscher, H. J. Viscoelasticity of biofilms and their recalcitrance to mechanical and chemical challenges. *FEMS Microbiol. Rev.*, 39(2):234–245, 2015.
- Peulen, T.-O. and Wilkinson, K. J. Diffusion of nanoparticles in a biofilm. *Environ. Sci. Technol.*, 45(8):3367–73, 2011.
- Phani, K. K. and Niyogi, S. K. Young’s modulus of porous brittle solids. *J. Mater. Sci.*, 22(1):257–263, 1987.
- Picioreanu, C., Loosdrecht, M., and Heijnen, J. Mathematical Modeling of Biofilm Structure with a Hybrid Differential-Discrete Cellular Automata Approach. *Biotechnol. Bioeng.*, 58(January):101–116, 1998.
- Picioreanu, C., van Loosdrecht, M. C., and Heijnen, J. J. A theoretical study on the effect of surface roughness on mass transport and transformation in biofilms. *Biotechnol Bioeng*, 68(4):355–369, 2000.
- Picioreanu, C., Kreft, J.-U., and Mark C. M. van Loosdrecht. Particle based multidimensional multispecies biofilm model. *Appl. Environ. Microbiol.*, 70(5):3024–3040, 2004.

- Prawoto, Y. Seeing auxetic materials from the mechanics point of view: A structural review on the negative Poisson's ratio. *Comput. Mater. Sci.*, 58:140–153, 2012.
- Proia, L., Von Schiller, D., Sánchez-Melsió, A., Sabater, S., Borrego, C. M., Rodríguez-Mozaz, S., and Balcázar, J. L. Occurrence and persistence of antibiotic resistance genes in river biofilms after wastewater inputs in small rivers. *Environ. Pollut.*, 210: 121–128, 2016.
- Radu, A. I., Vrouwenvelder, J. S., van Loosdrecht, M. C. M., and Picioreanu, C. Modeling the effect of biofilm formation on reverse osmosis performance: Flux, feed channel pressure drop and solute passage. *J. Memb. Sci.*, 365(1-2):1–15, 2010.
- Ramberg, W. and Osgood, W. R. Description of stress-strain curves by three parameters. *Natl. Advis. Comm. Aeronaut.*, pages 1–29, 1943.
- Roa, J. J., Oncins, G., Díaz, J., Sanz, F., and Segarra, M. Calculation of Young's Modulus Value by Means of AFM. *Recent Pat. Nanotechnol.*, 5:27–36, 2011.
- Røder, H. L., Raghupathi, P. K., Herschend, J., Brejnrod, A., Knøchel, S., Sørensen, S. J., and Burmølle, M. Interspecies interactions result in enhanced biofilm formation by co-cultures of bacteria isolated from a food processing environment. *Food Microbiol.*, 51:18–24, 2015.
- Roy, S. and Banerjee, A. Amino acid based smart hydrogel: formation, characterization and fluorescence properties of silver nanoclusters within the hydrogel matrix. *Soft Matter*, 7(11):5300, 2011.
- Roy, S., Baral, A., and Banerjee, A. An amino-acid-based self-healing hydrogel: modulation of the self-healing properties by incorporating carbon-based nanomaterials. *Chemistry*, 19(44):14950–14957, 2013.
- Rupp, C. J., Fux, C. A., and Stoodley, P. Viscoelasticity of *Staphylococcus aureus* biofilms in response to fluid shear allows resistance to detachment and facilitates rolling migration. *Appl. Environ. Microbiol.*, 71(4):2175–8, 2005.
- Ryshkewitch, E. Compression Strength of Porous Sintered Alumina and Zirconia. *J. Am. Ceram. Soc.*, 36(2):65–68, 1953.
- Safari, A., Habimana, O., Allen, A., and Casey, E. The significance of calcium ions on *Pseudomonas fluorescens* biofilms - a structural and mechanical study. *Biofouling*, 30(7):859–69, 2014.
- Saxena, K. K., Das, R., and Calius, E. P. Three Decades of Auxetics Research Materials with Negative Poisson's Ratio: A Review. *Adv. Eng. Mater.*, pages 1–24, 2016.
- Schindelin, J., Arganda-Carreras, I., Frise, E., Kaynig, V., Longair, M., Pietzsch, T., Preibisch, S., Rueden, C., Saalfeld, S., Schmid, B., Tinevez, J.-Y., White, D. J., Hartenstein, V., Eliceiri, K., Tomancak, P., and Cardona, A. Fiji: an open-source platform for biological-image analysis. *Nat. Methods*, 9(7):676–82, 2012.
- Shaw, T., Winston, M., Rupp, C. J., Klapper, I., and Stoodley, P. Commonality of Elastic Relaxation Times in Biofilms. *Phys. Rev. Lett.*, 93(9):098102, 2004.
- Simões, M., Simões, L. C., and Vieira, M. J. A review of current and emergent biofilm control strategies. *LWT - Food Sci. Technol.*, 43(4):573–583, 2010.

- Smith, A. M., Williams, R. J., Tang, C., Coppo, P., Collins, R. F., Turner, M. L., Saiani, A., and Ulijn, R. V. Fmoc-diphenylalanine self assembles to a hydrogel via a novel architecture based on pi-pi interlocked beta-sheets. *Adv. Mater.*, 20(1):37–41, 2008.
- Spriggs, R. M. Expression for Effect of Porosity on Elastic Modulus of Polycrystalline Refractory Materials, Particularly Aluminum Oxide. *J. Am. Ceram. Soc.*, 44(12): 628–629, 1961.
- Steiner, R., Kunzi-Rapp, K., and Scharffetter-Kochanek, K. Optical Coherence Tomography: Clinical Applications in Dermatology. *Med. Laser Appl.*, 18(3):249–259, 2003.
- Stewart, P. S. Diffusion in Biofilms. *J. Bacteriol.*, 185(5):1485–1491, 2003.
- Stoodley, P., Dodds, I., Boyle, J. D., and Lappin-Scott, H. M. Influence of hydrodynamics and nutrients on biofilm structure. *J. Appl. Microbiol.*, 85 Suppl 1:19S–28S, 1999.
- Stoodley, P., Lewandowski, Z., Boyle, J., and Lappin-Scott, H. The formation of migratory ripples in a mixed species bacterial biofilm growing in turbulent flow. *Environ. Microbiol.*, 1(5):447–55, 1999.
- Stoodley, P., Hall-Stoodley, L., and Lappin-Scott, H. M. Detachment, surface migration, and other dynamic behavior in bacterial biofilms revealed by digital time-lapse imaging. *Methods Enzymol.*, 337(1999):306–19, 2001.
- Stoodley, P., Jacobsen, A., Dunsmore, B. C., Purevdorj, B., Wilson, S., Lappin-Scott, H. M., and Costerton, J. W. The influence of fluid shear and AICI₃ on the material properties of *Pseudomonas aeruginosa* PAO1 and *Desulfovibrio* sp. EX265 biofilms. *Water Sci. Technol.*, 43(6):113–20, 2001.
- Stoodley, P., Cargo, R., Rupp, C., Wilson, S., and Klapper, I. Biofilm material properties as related to shear-induced deformation and detachment phenomena. *J. Ind. Microbiol. Biotechnol.*, 29(6):361–367, 2002.
- Stoodley, P., Lewandowski, Z., Boyle, J. D., and Lappin-Scott, H. M. Structural deformation of bacterial biofilms caused by short-term fluctuations in fluid shear: an in situ investigation of biofilm rheology. *Biotechnol. Bioeng.*, 65(1):83–92, 1999.
- Subramanian, G., Palanichamy, S., and Veeramani, P. An eco-friendly process for prevention of biofouling. *Prog. Org. Coatings*, 99:474–479, 2016.
- Sutherland, I. W. The biofilm matrix—an immobilized but dynamic microbial environment. *Trends Microbiol.*, 9(5):222–227, 2001.
- Sutherland, I. W. Biofilm exopolysaccharides: A strong and sticky framework. *Microbiology*, 147(1):3–9, 2001.
- Taherzadeh, D., Picioreanu, C., Küttler, U., Simone, A., Wall, W. A., and Horn, H. Computational study of the drag and oscillatory movement of biofilm streamers in fast flows. *Biotechnol. Bioeng.*, 105(3):600–610, 2010.
- Taherzadeh, D., Picioreanu, C., and Horn, H. Mass transfer enhancement in moving biofilm structures. *Biophys. J.*, 102(7):1483–92, 2012.

- Tierra, G., Pavissich, J. P., Nerenberg, R., Xu, Z., and Alber, M. S. Multicomponent model of deformation and detachment of a biofilm under fluid flow. *J. R. Soc. Interface*, 12(106):1–13, 2015.
- Touhami, A., Nysten, B., and Dufrêne, Y. F. Nanoscale Mapping of the Elasticity of Microbial Cells by Atomic Force Microscopy. *Langmuir*, 19(11):4539–4543, 2003.
- Towler, B. W., Rupp, C. J., Cunningham, A. B., and Stoodley, P. Viscoelastic properties of a mixed culture biofilm from rheometer creep analysis. *Biofouling*, 19(5):279–85, 2003.
- Tsuboi, M., Hayashi, A., Ikeda, N., Honda, H., Kato, Y., Ichinose, S., and Kato, H. Optical coherence tomography in the diagnosis of bronchial lesions. *Lung Cancer*, 49(3):387–394, 2005.
- Turan, O., Demirel, Y. K., Day, S., and Tezdogan, T. Experimental Determination of Added Hydrodynamic Resistance Caused by Marine Biofouling on Ships. *Transp. Res. Procedia*, 14(0):1649–1658, 2016.
- Valladares Linares, R., Wexler, A., Bucs, S., Dreszer, C., Zwijnenburg, A., Flemming, H.-C., Kruithof, J., and Vrouwenvelder, J. Compaction and relaxation of biofilms. *Desalin. Water Treat.*, 3994(July):1–13, 2015.
- Vincent, J. *Basic Elasticity and Viscoelasticity*. Princeton Univ. Press, Princeton, 3. ed. edition, 2012.
- Vinogradov, A. M., Winston, M., Rupp, C. J., and Stoodley, P. Rheology of biofilms formed from the dental plaque pathogen *Streptococcus mutans*. *Biofilms*, 1(1):49–56, 2004.
- Wagner, M., Manz, B., Volke, F., Neu, T. R., and Horn, H. Online assessment of biofilm development, sloughing and forced detachment in tube reactor by means of magnetic resonance microscopy. *Biotechnol. Bioeng.*, 107(1):172–181, 2010.
- Wagner, M., Taherzadeh, D., Haisch, C., and Horn, H. Investigation of the mesoscale structure and volumetric features of biofilms using optical coherence tomography. *Biotechnol. Bioeng.*, 107(5):844–853, 2010.
- Waters, M. S., Kundu, S., Lin, N. J., and Lin-Gibson, S. Microstructure and Mechanical Properties of In Situ *Streptococcus mutans* Biofilms. *ACS Appl. Mater. Interfaces*, 6(1):327–332, 2014.
- Weiss, R. G. and Terech, P., editors. *Molecular gels: materials with self-assembled fibrillar networks*. Springer-Verlag, Netherlands, 2006.
- West, S., Wagner, M., Engelke, C., and Horn, H. Optical coherence tomography for the in situ three-dimensional visualization and quantification of feed spacer channel fouling in reverse osmosis membrane modules. *J. Memb. Sci.*, 498:345–352, 2015.
- Wloka, M., Rehage, H., Flemming, H.-C., and Wingender, J. Rheological properties of viscoelastic biofilm extracellular polymeric substances and comparison to the behavior of calcium alginate gels. *Colloid Polym. Sci.*, 282(10):1067–1076, 2004.

- Wloka, M., Rehage, H., Flemming, H.-C., and Wingender, J. Structure and rheological behaviour of the extracellular polymeric substance network of mucoid *Pseudomonas aeruginosa* biofilms. *Biofilms*, 2:275–283, 2005.
- Xi, C., Marks, D., Schlachter, S., Luo, W., and Boppart, S. High-resolution three-dimensional imaging of biofilm development using optical coherence tomography. *J. Biomed. Opt.*, 11(3):34001, 2006.
- Yang, X., Beyenal, H., Harkin, G., and Lewandowski, Z. Quantifying biofilm structure using image analysis. *J. Microbiol. Methods*, 39(2):109–19, 2000.
- Zhang, T. C. and Bishop, P. L. Density, porosity, and pore structure of biofilms. *Water Res.*, 28(11):2267–2277, 1994.
- Zhang, X., Bishop, P. L., and Kupferle, M. J. Measurement of polysaccharides and proteins in biofilm extracellular polymers. *Water Sci. Technol.*, 37(4-5):345–348, 1998.
- Zheng, L. Y., Farnam, D. S., Homentcovschi, D., and Sammakia, B. G. A porous elastic model for bacterial biofilms: application to the simulation of deformation of bacterial biofilms under microfluidic jet impingement. *J. Biomech. Eng.*, 134(5):051003, 2012.

Schriftenreihe des Lehrstuhls für Wasserchemie und Wassertechnologie und
der DVGW-Forschungsstelle am Engler-Bunte-Institut
des Karlsruher Instituts für Technologie (KIT)

Band 35: Symposium on Refractory Organic Substances in the Environment ROSE, 1997, 248 S., 12,80 €.

Band 36: Symposium on Refractory Organic Substances in the Environment ROSE II, 2000, 265 S., 12,80 €.

Band 37: Thomas Brinkmann: Alkalischer und solarinduzierter Abbau von natürlicher organischer Materie, 2003, 212 S., 15,00 €.

Band 38: Andreas Gorenflo: Rückhalt und Fouling von natürlichen organischen Substanzen bei der Nano- und Ultrafiltration, 2003, 219 S., 18,00 €.

Band 39: Philip Hörsch: Einfluss der chemischen Oxidation auf das toxische Potenzial und das biologische Abbauverhalten von Industrieabwässern, 2004, 210 S., 20,00 €.

Band 40: Margit B. Müller: Bewertung von Anreicherungs- und Fraktionierungsverfahren für die strukturelle Charakterisierung der gelösten organischen Substanz in Gewässern, 2004, 185 S., 18,00 €.

Band 41: Fritz H. Frimmel, Gudrun Abbt-Braun: Praktikum Allgemeine Chemie und Chemie in wässrigen Lösungen - Qualitative und quantitative Bestimmungen, 2004, 158 S., 18,00 €.

Band 42: Tusnelda E. Doll: Photochemischer und photokatalytischer Abbau von Carbamazepin, Clofibrinsäure, Iomeprol und Iopromid, 2004, 158 S., 18,00 €.

Band 43: Ayşe B. Değer: Entfernung von organischen Schadstoffen aus Wasser mit Hilfe von Poly(ϵ -caprolacton), 2005, 205 S., 18,00 €.

Band 44: Fritz H. Frimmel, Gudrun Abbt-Braun: Wassertechnologisches und wasserchemisches Praktikum, 2005, 201 S., 20,00 €.

Band 45-I, 45-II: Fritz H. Frimmel, Gudrun Abbt-Braun (Eds.): Humic Substances - Linking Structure to Functions. Proceedings of the 13th Meeting of the International Humic Substances Society, July 30 to August 4, 2006, Universität Karlsruhe, 2006, 492 S. (45-I), 623 S. (45-II), 50,00 €.

Band 46: Fritz H. Frimmel, Gudrun Abbt-Braun: Praktikum Allgemeine Chemie und Chemie in wässrigen Lösungen - Qualitative und quantitative Bestimmungen II, 2. verbesserte und ergänzte Neuauflage 2007, 139 S., 20,00 €.

Band 47: Thomas Glauner: Aufbereitung von Schwimmbeckenwasser - Bildung und Nachweis von Desinfektionsnebenprodukten und ihre Minimierung mit Membran- und Oxidationsverfahren, 2007, 233 S., 20,00 €.

Band 48: George Metreveli: Kolloidale Wechselwirkungen und kolloidgetragener Transport von Metall(oid)en in porösen Medien, 2008, 215 S., 20,00 €.

Band 49: Florencia Saravia: Entfernung von organischen Spurenstoffen und Untersuchung von Foulingprozessen in getauchten Membranen und Hybridverfahren, 2009, 213 S., 20,00 €.

Band 50: Markus Delay: Dynamische versus statische Elutionsversuche - Ein Beitrag zur Beurteilung der Wiederverwertbarkeit von Abfallmaterialien, 2010, 206 S., 20,00 €.

Band 51: Luis A. Tercero Espinoza: Heterogeneous photocatalysis with titanium dioxide suspensions containing bromide and dissolved organic matter, 2010, 172 S., 20,00 €.

Band 52: Ulrich-M. Metzger: Extrazelluläre polymere Substanzen aus Biofilmen - Aufklärung von Strukturen und ihr Einfluss auf die Foulingbildung in Membranbioreaktoren, 2011, 211 S., 20,00 €.

- Band 53:** Fritz H. Frimmel, Gudrun Abbt-Braun: Praktikum Allgemeine Chemie und Chemie in wässrigen Lösungen - Qualitative und quantitative Bestimmungen, 3. überarbeitete Neuauflage 2011, 139 S., 20,00 €.
- Band 54:** Markus Ziegmann: Beurteilung von Cyanobakterienblüten und Untersuchung geeigneter Verfahrenskombinationen zur Elimination cyanobakterieller Zellen und Toxine, 2011, 191 S., 20,00 €.
- Band 55:** Fritz H. Frimmel, Gudrun Abbt-Braun: Praktikum Allgemeine Chemie und Chemie in wässrigen Lösungen - Qualitative und quantitative Bestimmungen, 4. ergänzte Neuauflage 2012, 137 S., 20,00 €.
- Band 56:** Angela Klüpfel: Nanofiltration bei der Aufbereitung von Trink- und Schwimmbeckenwasser - Foulingmechanismen und Rückhalt anthropogener Kontaminanten, 2012, 259 S., 20,00 €.
- Band 57:** Christina Schmalz: Bildung, Phasentransfer und Toxizität halogener Desinfektionsnebenprodukte im Aufbereitungszyklus von Schwimmbeckenwasser - Schwerpunkt stickstoffhaltige Verbindungen, 2012, 195 S., 20,00 €.
- Band 58:** Fritz H. Frimmel, Gudrun Abbt-Braun, Harald Horn: Praktikum Allgemeine Chemie und Chemie in wässrigen Lösungen - Qualitative und quantitative Bestimmungen, 5. ergänzte Neuauflage 2013, 120 S., 20,00 €.
- Band 59:** Heiko Schwegmann: Wechselwirkungen zwischen anorganischen Nanopartikeln und Mikroorganismen - Nutzungs- und Gefährdungspotentiale, 2013, 149 S., 20,00 €.
- Band 60:** Fritz H. Frimmel, Gudrun Abbt-Braun, Harald Horn: Praktikum Allgemeine Chemie und Chemie in wässrigen Lösungen - Qualitative und quantitative Bestimmungen, 6. überarbeitete Neuauflage 2014, 129 S., 20,00 €.
- Band 61:** Carsten Jobelius: Anaerobe Metabolite organischer Schadstoffe im Grundwasser - Analytik, Bildung und Nutzung als Indikatoren, 2014, 247 S., 20,00 €.
- Band 62:** Eva M. Gilbert: Partielle Nitrifikation / Anammox bei niedrigen Temperaturen, 2014, 115 S., 20,00 €.
- Band 63:** Aleksandr O. Kondrakov: Heterogeneous photocatalysis and sensitized photolysis for enhanced degradation of bisphenol A and its analogues, 2015, 155 S., 20,00 €.
- Band 64:** Meijie Ren: TiO₂: application in photocatalysis for the degradation of organic pollutants and aggregation behavior in aquatic systems, 2015, 121 S., 20,00 €.
- Band 65:** Fritz H. Frimmel, Gudrun Abbt-Braun, Harald Horn: Praktikum Allgemeine Chemie und Chemie in wässrigen Lösungen - Qualitative und quantitative Bestimmungen, 7. überarbeitete Neuauflage 2016, 126 S., 20,00 €.
- Band 66:** Chunyan Li: Using optical coherence tomography to quantify biofilm structure and mass transfer in combination with mathematical modeling, 2016, 121 S., 20,00 €.
- Band 67:** Maria Pia Herrling: Nanoparticles in biofilm systems - assessment of their interactions by magnetic susceptibility balance and magnetic resonance imaging, 2016, 132 S., 20,00 €.
- Band 68:** Elham Fatoorehchi: Sludge disintegration techniques - assessment of their impacts on solubilization of organic carbon and methane production, 2016, 116 S., 20,00 €.
- Band 69:** Norman Hack: Refraktäre organische Substanzen im Kapillarsaum: ihre Dynamik, Gradienten und Reaktionen, 2016, 152 S., 20,00 €.
- Band 70:** Di Peng: Disinfection by-products and the application potential of nanofiltration in swimming pool water treatment, 2016, 112 S., 20,00 €.
- Band 71:** Jueying Qian: Investigation of the fouling driving factors in drip irrigation systems, 2017, 112 S., 20,00 €.

Band 72: Florian Blauert: Investigating biofilm deformation using optical coherence tomography and fluid-structure interaction simulation, 2017, 105 S., 20,00 €.

Preise verstehen sich zzgl. der gesetzlichen Mehrwertsteuer und Versandkosten.

Bestellungen über:

Lehrstuhl für Wasserchemie und Wassertechnologie und DVGW-Forschungsstelle
am Engler-Bunte-Institut des Karlsruher Instituts für Technologie (KIT)

Engler-Bunte-Ring 9

D-76131 Karlsruhe

Tel.: +49-(0)721-608-42581

Fax: +49-(0)721-608-46497

E-mail: ebi-sekretariat-wasserchemie@kit.edu